

공학박사 학위논문

**Study of Heteroatom-doped  
Carbon Materials derived from  
Polyimide Precursors for  
Supercapacitor Applications**

슈퍼커패시터 응용을 위한 폴리이미드  
전구체 기반의 이종원소 도핑 탄소 재료 연구

2018년 8월

서울대학교 융합과학기술대학원

융합과학부 나노융합전공

김 대 겸

# Study of Heteroatom-doped Carbon Materials derived from Polyimide Precursors for Supercapacitor Applications

지도 교수 박 원 철

이 논문을 공학박사 학위논문으로 제출함  
2018년 5월

서울대학교 융합과학기술대학원  
융합과학부 나노융합전공  
김 대 겸

김대겸의 공학박사 학위논문을 인준함  
2018년 7월

위 원 장           김 연 상           (인)

부위원장           박 원 철           (인)

위 원           이 강 원           (인)

위 원           나 현 빈           (인)

위 원           유 태 경           (인)

## **Abstract**

# **Study of Heteroatom-doped Carbon Materials derived from Polyimide Precursors for Supercapacitor Applications**

Dae Kyom Kim

Program in Nano Science and Technology

Graduate School of Convergence Science & Technology

Seoul National University

Carbon materials are most widely used as supercapacitor electrode materials because of high power density, high electrical conductivity, and stable long cycle life. However, it needs to overcome their relatively low energy density properties. The various design strategies to enhance specific capacitance of carbon materials have been developed to figure out the problems.

This thesis is mainly focused on the synthesis, characterization and supercapacitor applications of various types of heteroatom doped carbon materials derived from PI precursors by *in situ* doping technique. In the following chapters, we will introduce different kinds of heteroatoms, which are doped into carbon matrix and investigate their doping effects in electrochemical performances.

Firstly, nitrogen-doped carbon derived from polyimide/MWCNT composites for flexible all-solid-state symmetric supercapacitors was developed. As a nitrogen-doped carbon precursor, aminophenyl multiwall carbon nanotube grafted PI precursor was synthesized by *in situ* polymerization method. The synthesized PI precursor solution was dropped to the CC surface which was served as the flexible substrate and current collector and coating followed by direct carbonization at high temperature. These suggested drop, paste and pyrolysis process for the fabrication of electrodes effectively solved the technical problems of the control of the loading mass of active material on the CC surface, and the difficulty of large scale production. The obtained electrode showed a high specific capacitance of  $333.4 \text{ F g}^{-1}$  at  $1 \text{ A g}^{-1}$  (based on active material mass) in a three electrode system. Fabricated an all-solid-state flexible supercapacitor device exhibited a high volumetric

capacitance of  $3.88 \text{ F cm}^{-3}$  at a current density of  $0.02 \text{ mA cm}^{-3}$ . This flexible supercapacitor device can deliver the maximum volumetric energy density of  $0.50 \text{ mWh cm}^{-3}$  and presents a good cycling stability with capacitance retention of 85.3% after 10,000 cycles. Furthermore, this device displays superior flexibility with stable electrochemical performance and good capacitance retention.

Secondly, multiple-heteroatom-doped carbons (from single- to triple-doped) by the pyrolysis of polyimide precursors using a simple and facile *in situ* approach were developed. This approach can be tuned heteroatom compositions by controlling the desired polyimide monomer functional groups as well as introducing external doping sources into the polyimide precursor solutions. Various types of multiple-heteroatom-doped carbons such as N, N,S-, N,F-, N,S,B-, and N,F,B-doped carbon were synthesized. In comparison with single N-doped carbons, the specific capacitance of N,F,B-triple-doped carbon was remarkably enhanced, to  $350.3 \text{ F g}^{-1}$  at  $1 \text{ A g}^{-1}$  in a three-electrode system. Moreover, a flexible all-solid-state supercapacitor device was fabricated based on the N,F,B-triple-doped carbon, which exhibited a high volumetric capacitance of  $4.45 \text{ F cm}^{-3}$  at a current

density of  $0.01 \text{ mA cm}^{-3}$ . The maximum volumetric energy density of the flexible supercapacitor device was achieved as  $0.58 \text{ mWh cm}^{-3}$ .

Finally, N,B-co-doped carbon by pyrolysis using polyimide precursors incorporating ammonia borane ( $\text{NH}_3\text{BH}_3$ ) was synthesized with a simple and effective process. Polyimide is an attractive N-doping carbon source for supercapacitor applications. In addition,  $\text{NH}_3\text{BH}_3$  is an efficient heteroatom-doping source for introducing boron as well as nitrogen atoms during thermal processes. N,B-co-doped carbon was prepared by high-temperature pyrolysis of a precursor solution pasted on carbon cloth. The effects of dual doping of the carbon surface were investigated by X-ray photoelectron spectroscopy, Raman spectroscopy, and sheet resistance measurements. In comparison with N-doped carbon, the specific capacitance of N,B-co-doped carbon in a three-electrode system was enhanced ( $277.8 \text{ F g}^{-1}$  at  $1 \text{ A g}^{-1}$ ) owing to the synergetic effects of dual heteroatom doping. An as-fabricated flexible all-solid-state supercapacitor device exhibited a volumetric capacitance of  $2.97 \text{ F cm}^{-3}$  at a current density of  $0.01 \text{ mA cm}^{-3}$  and a maximum energy density of  $0.38 \text{ mWh cm}^{-3}$ .

**Keywords: Supercapacitor, Carbon material, Polyimide,  
Heteroatom doping, Flexible electrode**

**Student Number: 2012-30692**

# Contents

## Chapter 1. Introduction

1.1. Supercapacitor.....	23
1.1.1. Energy storage systems.....	23
1.1.2. Electric double layer capacitors.....	28
1.2. Heteroatom doped carbon materials .....	32
1.2.1. Carbon materials for supercapacitor applications .....	32
1.2.2. Heteroatom doped carbons for supercapacitor applications.....	36
1.2.3. Nitrogen doping.....	36
1.2.4. Fluorine doping .....	40
1.2.5. Sulfur doping .....	40
1.2.6. Boron doping.....	42
1.2.7. Multiple heteroatom doping .....	44
1.3. Carbonized polyimides .....	46
1.3.1. Polyimides .....	46
1.3.2. Carbonized polyimides.....	49
1.3.3. Carbonized polyimides for supercapacitor applications.....	52

1.4. Carbon textiles .....	54
1.4.1. Carbon textiles for supercapacitor applications.....	54
1.5. Objectives .....	57

## **Chapter 2. Experiment**

2.1. Synthesis of heteroatom doped carbon precursors.....	59
2.1.1. Nitrogen doped carbon derived from polyimide/multiwall carbon nanotube composites.....	59
2.1.1.1. Synthesis of MWCNT-PI nanocomposite precursor.....	59
2.1.2. Multiple-heteroatom-doped carbon derived from polyimide precursors .....	60
2.1.2.1. Synthesis of NCP precursor .....	60
2.1.2.2. Synthesis of NSCP precursor .....	60
2.1.2.3. Synthesis of NFCP precursor .....	61
2.1.2.4. Synthesis of NSBCP precursor.....	61
2.1.2.5. Synthesis of NFBCP precursor.....	62
2.1.3. Nitrogen- and boron-co-doped carbon derived from polyimide precursors .....	64
2.1.3.1. Synthesis of PI precursor .....	64

2.1.3.2. Synthesis of NBCP precursor.....	64
2.2. Fabrication of heteroatom-doped carbon electrodes .....	65
2.3. Fabrication of all-solid-state symmetric supercapacitors .....	65
2.4. Materials characterizations .....	68
2.5. Electrochemical measurements.....	68

### **Chapter 3. Results and Discussion**

3.1. Nitrogen doped carbon derived from polyimide/multiwall carbon nanotube composites .....	71
3.1.1. Physical and chemical analysis .....	71
3.1.2. Electrochemical activity measurements .....	88
3.2. Multiple-heteroatom-doped carbon derived from polyimide precursors.....	102
3.2.1. Physical and chemical analysis .....	102
3.2.2. Electrochemical activity measurements .....	122
3.3. Nitrogen- and boron-co-doped carbon derived from polyimide precursors.....	136
3.3.1. Physical and chemical analysis .....	136
3.3.2. Electrochemical activity measurements .....	149

<b>Chapter 4. Conclusions</b> .....	159
<b>References</b> .....	164
<b>국문 초록 (Abstract in Korean)</b> .....	174

## List of Figures

- Figure 1.1.** Global generation capacity of sustainable energy. (source from bloomberg new energy finance 2017).....25
- Figure 1.2.** Comparison of power density and energy density with energy storage systems. ....26
- Figure 1.3.** Schematic illustration of electric double layer capacitor (EDLC). (Left image source from <https://www.ultracapacitor.co.kr>) .. .....27
- Figure 1.4.** Basic schematics for an (a) all carbon EDLC, (b) a pseudocapacitor. (from Ref. [1] Jost *et al.*, *J. Mater. Chem. A*, **2014**, 2, 10776-10787.).. .....30
- Figure 1.5.** Schematic illustration of (a) Helmholtz, (b) Gouy-Chapman, and (c) Stern model of the electrical double-layer formed at a positively charged electrode in an aqueous electrolyte. (from Ref. [5] Beguin *et al.*, *Adv. Mater.*, **2014**, 26, 2219-2251.).. .....31
- Figure 1.6.** Various type of supercapacitor materials. (from Ref. [4] Rolison *et al.*, *Chem. Soc. Rev.*, **2009**, 38, 226-252.).....34
- Figure 1.7.** Schematic illustration of different approaches to improve energy density of a supercapacitor.....35

<b>Figure 1.8.</b> Distribution of nitrogen atoms in carbon graphene structure. (from Ref. [13] Jurewicz <i>et al.</i> , <i>Electrochim. Acta</i> , <b>2003</b> , 48, 1491-1498.)..	39
<b>Figure 1.9.</b> Schematic illustration of a proposed electrochemical performance mechanism on S-containing mesoporous carbon. (from Ref. [29] Zhao <i>et al.</i> , <i>Nano Energy</i> , <b>2012</b> , 1, 624-630.)..	41
<b>Figure 1.10.</b> Ball model of B-G showing some of the most common boron induced defects. (from Ref. [32] Agnoli <i>et al.</i> , <i>J. Mater. Chem. A</i> , <b>2016</b> , 4, 5002-5025.)..	43
<b>Figure 1.11.</b> Synthetic scheme of polyimide. ...	48
<b>Figure 1.12.</b> Various types of polyimide derivatives. (from [43] Inagaki <i>et al.</i> , <i>Carbon</i> , <b>2013</b> , 61, 1-21.)..	50
<b>Figure 1.13.</b> Thermal stability of crane made by PI film. (from [43] Inagaki <i>et al.</i> , <i>Carbon</i> , <b>2013</b> , 61, 1-21.)..	51
<b>Figure 1.14.</b> Carbon cloth (W0S1002 produced from CeTech Co., Ltd.) product specification and SEM images. ...	56
<b>Figure 2.1.</b> Synthetic scheme of (a) NFCP, (b) NSCP, and (c) NCP precursors. ...	63
<b>Figure 2.2.</b> Fabrication scheme of all-solid-state symmetric	

supercapacitors. ....	67
<b>Figure 3.1.</b> Shematic illustration of the preparation of flexible CC/C-MWCNT-PI electrodes. ....	73
<b>Figure 3.2.</b> Plot of the carbonization temperature vs. the sheet resistance of CC/C-MWCNT-PI. ....	75
<b>Figure 3.3.</b> SEM images of CC, CC/MWCNT-PI-300, and CC/C-MWCNT-PI-800. (a), (d) CC, (b), (e) CC/MWCNT-PI-300 and c, f) CC/C-MWCNT-PI-800. The insets in (e), and (f) are high resolution SEM images of CC/MWCNT-PI-300 and CC/C-MWCNT-PI-800, respectively. ....	77
<b>Figure 3.4.</b> SEM images of (a), (d) CC/C-MWCNT-PI-600, (b), (e) CC/C-MWCNT-PI-1000 and (c), (f) CC/C-PI-800. The insets in (d), (e), and (f) are high resolution of SEM images of CC/C-MWCNT-PI-600, CC/C-MWCNT-PI-1000, and CC/C-MWCNT-PI-800, respectively. ....	78
<b>Figure 3.5.</b> TGA analysis of CC, CC/PI precursor, and CC/MWCNT-PI precursor. ....	80
<b>Figure 3.6.</b> Raman spectra of CC, CC/C-PI-800, and CC/C-MWCNT-PI-800. ....	82
<b>Figure 3.7.</b> Low resolution XPS spectra of CC/C-MWCNT-PI-1000,	

CC/C-MWCNT-PI-800,                    CC/C-MWCNT-PI-600,	
CC/MWCNT-PI-300, and CC/C-PI-800. ... ..	85

**Figure 3.8.** High resolution XPS spectra of N1s. (a) CC/MWCNT-PI-300, (b) CC/C-MWCNT-PI-600, (c) CC/C-MWCNT-PI-800, (d) CC/C-MWCNT-PI-1000, (e) CC/C-PI-800 and (f) nitrogen configuration ratio of all samples. ....86

**Figure 3.9.** Electrochemical performances in a three electrode system by using 1 M H<sub>2</sub>SO<sub>4</sub> electrolyte within a potential range of 0–1.0 V. (a) CV curves of all samples at a scan rate of 10 mV s<sup>-1</sup>. (b) Specific capacitance of all samples at different current densities. (c) CV curves of CC/C-MWCNT-PI-800 at scan rates of 5, 10, 20, 50, 100 mV s<sup>-1</sup>. (d) Charge-discharge curves of CC/C-MWCNT-PI-800 at various current densities. ... ..92

**Figure 3.10.** Electrochemical performances in a three electrode system by using 1 M H<sub>2</sub>SO<sub>4</sub> electrolyte within a potential range of 0–1.0 V. (a) Nyquist plots of all samples over a frequency range of 0.01 Hz – 1 MHz. (b) Cycle testing at a scan rate of 50 mV s<sup>-1</sup> of CC/C-MWCNT-PI-800. ....93

**Figure 3.11.** Contact angle measurement of (a) bare CC and (b) CC/C-

MWCNT-PI-800. ....94

**Figure 3.12.** Electrochemical performances of flexible all-solid-state CC/C-MWCNT-PI-800 symmetric supercapacitor integrated with PVA- H<sub>2</sub>SO<sub>4</sub> polymer gel electrolyte. (a) CV curves at scan rates of 5, 10, 20, 50, 100 mV s<sup>-1</sup>. (b) Charge-discharge curves at various current densities. (c) Volumetric capacitance at various current densities. (d) Cycle testing at a current density of 0.2 A cm<sup>-3</sup> over 10,000 cycles. ....99

**Figure 3.13.** Nyquist plot of flexible all-solid-state CC/C-MWCNT-PI-800 symmetric supercapacitor cell integrated with PVA-H<sub>2</sub>SO<sub>4</sub> polymer gel electrolyte. ....100

**Figure 3.14.** Flexibility tests of all-solid-state supercapacitors under flattening, folding, twisting, and rolling. (a) Digital images and (b) CV curves at a scan rate 10 mV s<sup>-1</sup>. ....101

**Figure 3.15.** Schematic illustration of preparation of the multiple heteroatom doped carbon electrodes. ....103

**Figure 3.16.** (a) Low- and (b) high-magnification SEM images of NFBCP electrode. ....105

**Figure 3.17.** TGA analysis of multiple heteroatom doped carbons... ..107

<b>Figure 3.18.</b> Raman spectra of multiple heteroatom doped carbons....	110
<b>Figure 3.19.</b> (a) The Low-resolution XPS spectra of multiple heteroatom doped carbons and high-resolution XPS spectra of (b) N 1s, (c) F 1s, (d) B 1s for NFBCP. ....	114
<b>Figure 3.20.</b> High-resolution XPS spectra of N 1s, and F 1s for NFCP. ....	115
<b>Figure 3.21.</b> High-resolution XPS spectra of N 1s, S 2p, and B 1s for NSBCP. ....	115
<b>Figure 3.22.</b> High-resolution XPS spectra of N 1s, and S 2p for NSCP. ....	116
<b>Figure 3.23.</b> High-resolution XPS spectra of N 1s for NCP. ..	116
<b>Figure 3.24.</b> Sheet resistance measurement results of multiple-heteroatom-doped carbons. ....	119
<b>Figure 3.25.</b> Contact angle measurement result of multiple-heteroatom-doped carbons. ....	121
<b>Figure 3.26.</b> Electrochemical performances of multiple-heteroatom-doped carbons in a three-electrode system. (a) CV curves at scan rate of $10 \text{ mV s}^{-1}$ . (b) Specific capacitance at different current densities from $1 \text{ A g}^{-1}$ to $20 \text{ A g}^{-1}$ . (c) CV curves of NFBCP at different scan rates from $10 \text{ mV s}^{-1}$ to	

100 mV s<sup>-1</sup>. (d) GCD curves of NFBCP at different current densities from 1 A g<sup>-1</sup> to 20 A g<sup>-1</sup>. (e) Comparison of Nyquist plots of NCP and NFBCP with frequencies from 0.01 Hz to 1 MHz. (f) Cycle stability test of NFBCP at current density of 5 A g<sup>-1</sup>. .....127

**Figure 3.27.** Electrochemical performances of multiple-heteroatom-doped carbons in a three-electrode system. (a) Comparison of Nyquist plots of NCP and NFBCP with frequencies from 0.01 Hz to 1 MHz. (b) Cycle stability test of NFBCP at current density of 5 A g<sup>-1</sup>. .....128

**Figure 3.28.** Electrochemical performances of the flexible all-solid-state supercapacitor device with NFBCP. (a) CV curves at scan rates from 10 to 100 mV s<sup>-1</sup>. (b) GCD curves at current density from 0.01 A cm<sup>-3</sup> to 0.2 A cm<sup>-3</sup>. (c) Volumetric capacitance at different current densities calculated from the GCD curves. (d) Long-term cycle stability test at current density of 0.05 A cm<sup>-3</sup>. .....133

**Figure 3.29.** Electrochemical performances of the flexible all-solid-state supercapacitor device with NFBCP. (a) Flexibility test under bending and flattening at a scan rate of 50 mV

	s <sup>-1</sup> . (b) Digital photo images of a LED lighted test with three devices connected in series. ....	134
<b>Figure 3.30.</b>	Nyquist plot of flexible all-solid-state NFBCP symmetric supercapacitor cell integrated with PVA-H <sub>2</sub> SO <sub>4</sub> polymer gel electrolyte. ...	135
<b>Figure 3.31.</b>	Schematic illustration of preparation of the nitrogen-and boron-co-doped carbon electrodes. ....	137
<b>Figure 3.32.</b>	(a) Low- and (b) high-magnification SEM images of NBCP electrode... ..	138
<b>Figure 3.33.</b>	TGA analysis of CC and NBCPs. ....	140
<b>Figure 3.34.</b>	(a) Low-resolution XPS spectra of NBCPs and high-resolution (b) C 1s, (c) N 1s, and (d) B 1s XPS spectra.. ..	142
<b>Figure 3.35.</b>	(a) Raman spectra of CC and NBCP samples. (b) Comparison of peak intensity ratios $I_{2D}/I_G$ and $I_D/I_G$ in the Raman spectra of NBCPs. ....	146
<b>Figure 3.36.</b>	Sheet resistances of CC and NBCPs. ....	148
<b>Figure 3.37.</b>	Electrochemical performance of NBCPs in a three-electrode system. (a) CV curves of NBCPs at a scan rate of 10 mV s <sup>-1</sup> . (b) Specific capacitance of NBCPs at	

various current densities from 1 to 20 A g<sup>-1</sup>. (c) Comparison of the specific capacitances of NBCPs at current densities of 1 and 20 A g<sup>-1</sup>. (d) CV curves of NBCP-3 at various scan rates from 10 to 100 mV s<sup>-1</sup>.....152

**Figure 3.38.** Electrochemical performance of NBCPs in a three-electrode system. (a) GCD curves of NBCP-3 at various current densities from 1 to 20 A g<sup>-1</sup>. (b) Nyquist plots of NBCP-0 and NBCP-3 in the frequency range of 0.01 Hz to 1 MHz. ....153

**Figure 3.39.** Electrochemical performance of the flexible all-solid-state supercapacitor device with NBCP-3. (a) CV curves at scan rates from 10 to 100 mV s<sup>-1</sup>. (b) GCD curves at current densities from 0.01 to 0.2 A cm<sup>-3</sup>. (c) Volumetric capacitances at various current densities calculated from the GCD curves. (d) Long-term cycle stability test at a current density of 0.05 A cm<sup>-3</sup>. ....157

**Figure 3.40.** Electrochemical performance of the flexible all-solid-state supercapacitor device with NBCP-3. (a) Flexibility test under rolled and flattened conditions at a scan rate of 50 mV s<sup>-1</sup>. (b) Digital photos of a LED test with three

devices connected in series. ....158

**Figure 3.41.** Nyquist plot of flexible all-solid-state NBCP-3 symmetric supercapacitor cell integrated with PVA-H<sub>2</sub>SO<sub>4</sub> polymer gel electrolyte. ....159

**Figure 4.1.** Ragone plots of the flexible all-solid-state supercapacitor devices of NFBCP, NBCP-3, and CC/C-MWCNT-PI-800. ....163

## List of Tables

<b>Table 3.1.</b>	Elemental analysis and relative contents of functional groups in N 1s peaks obtained by XPS. ....	87
<b>Table 3.2.</b>	Comparison of the nitrogen doped carbon-based materials in the three-electrode systems. ....	95
<b>Table 3.3.</b>	Raman spectra data of multiple-heteroatom-doped carbons. ....	111
<b>Table 3.4.</b>	Heteroatom contents of all samples by XPS analysis. ....	117
<b>Table 3.5.</b>	Comparison of the multiple-heteroatom-doped carbon-based materials in the three-electrode system. ...	129
<b>Table 3.6.</b>	Elemental contents of NBCPss obtained by XPS analysis. ..	143

# Chapter 1. Introduction

## 1.1 Supercapacitor

### 1.1.1 Energy storage systems

The excessive consumption and decreasing availability of fossil fuels in the past decades have become one of the most significant worldwide issues in terms of environmental problems such as global warming. Thus, developments of sustainable and renewable energy, which are less environmental impact and produce energy permanently, have been more and more attentions in recent years. The sustainable and renewable energy include biofuels, solar, wind, energy efficiency, pollution prevention, and smart grids. As gradually increasing global electricity production rates from sustainable & renewable energy, an efficient energy conversion and storage technologies with high performance such as long-term stability, high energy and power densities are also required (**Figure 1.1**).

Considering a reliable, stable, and sustainable large-scale use of renewable energy storage systems, especially batteries and

supercapacitors play an important key role for advanced and highly efficient energy storage systems (**Figure 1.2**). In generally, rechargeable batteries are used for portable electronics and electric vehicles due to their high energy density, however, they have performance limitations relatively long charging-discharging time and consequently lower power densities. Supercapacitors, also known as electrochemical capacitors or ultracapacitors, exhibit high power density, rapid charging/discharging time, superior rate capability, and long cycle life (**Figure 1.3**). Especially, their high power density property is used in the application fields such as back-up system, consumer portable device, hybride electric vehicles and other devices.

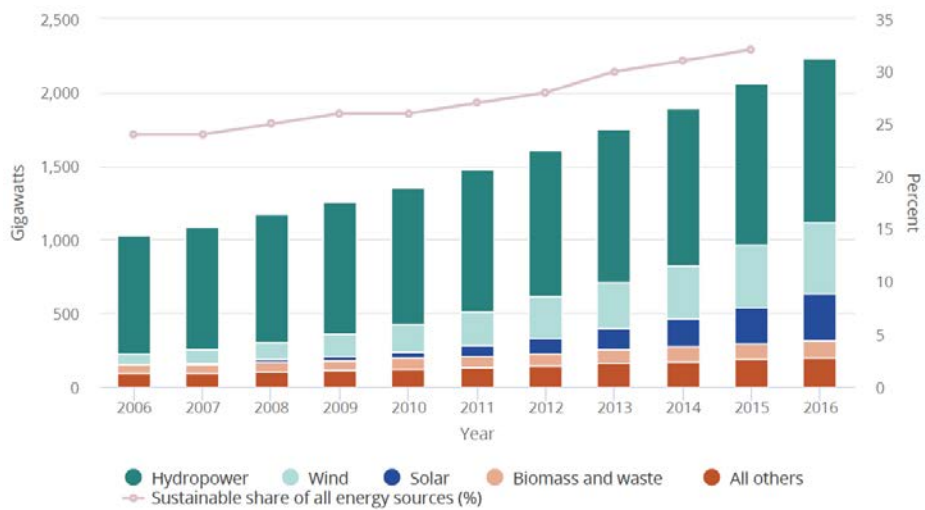


**Figure 1.1.** Global generation capacity of sustainable energy. (source from bloomberg new energy finance 2017)

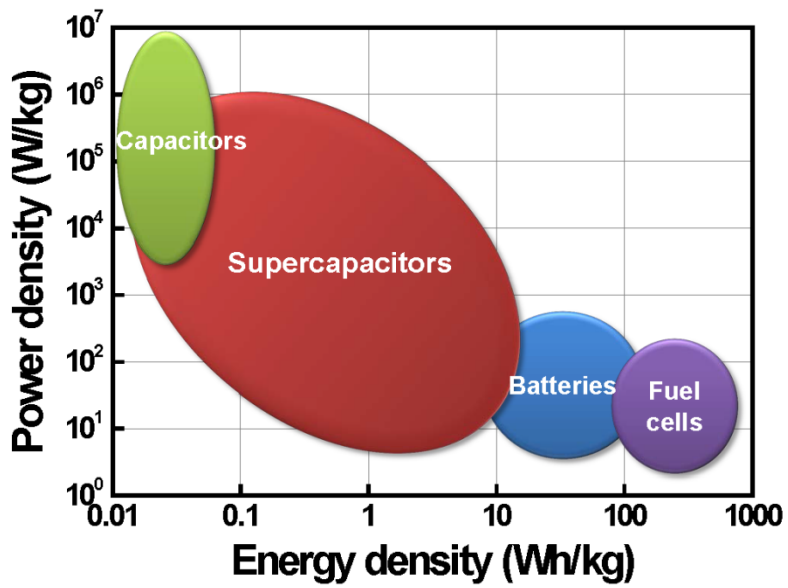


**Figure 1.2.** Comparison of power density and energy density with energy storage systems.

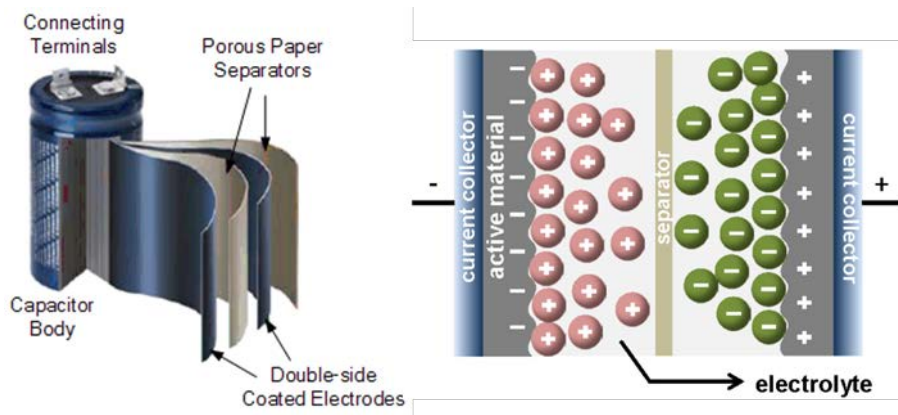


**Figure 1.3.** Schematic illustration of electric double layer capacitor (EDLC). (Left image source from <https://www.ultracapacitor.co.kr>)

### 1.1.2 Electric double layer capacitors

Supercapacitor or electrochemical capacitors can be classified electric double layer capacitors (EDLCs) and pseudocapacitors by charge storage mechanism as well as the active materials used (**Figure 1.4**) [1]. Supercapacitor devices typically consist of an electrode material, current collector, separator and electrolyte. EDLCs store charges by electrostatic interactions at the electrical double layer of electrode/electrolyte interface through nonfaradaic process using carbon base active materials. While, charge storage mechanism of pseudocapacitors is fast and reversible surface or near-surface reactions through faradaic process. Transition metal oxides or conducting polymers are used as active materials for pseudocapacitors [2-4].

In conventional capacitors without a consideration of electrolyte and active materials, the capacitors are consist of two metal plates separated by dielectrics such as air, glass, paper etc. When applied current voltage, the charged ions are accumulated both sides of metal plates. The capacitor can store more charge under the condition of the larger the area of metal plates or the smaller gap between metal plates. When consider electrolyte and active materials, the main energy storage

mechanism of EDLCs can be explained by the reversible electrostatic accumulation of ions on the surface of porous carbon. Helmholtz model describes that the charge separation occurs on polarization at the electrode-electrolyte interface [3].

$$C = \frac{\epsilon_r \epsilon_0 A}{d}$$

where  $C$  is the double layer capacitance,  $\epsilon_r$  is the electrolyte dielectric constant,  $\epsilon_0$  is the dielectric constant of the vacuum,  $A$  is the electrode surface area and  $d$  is the effective thickness of the double layer. Therefore, the very large specific surface area of porous carbon and less than 1 nm of the effective thickness of the double layer can obtained larger capacitance than conventional flat plate capacitors. Considering several factors such as the diffusion of ions in the solution and the interaction between the dipole moment of the solvent and the electrode, Gouy and Chapman proposed the modified diffuse model in which the potential decreases exponentially from the electrode surface to the fluid bulk [5]. This model, however, is not sufficient for highly charged double-layers, Stern suggested a new model combining the Helmholtz and Gouy-Chapman. Stern model considers the hydrodynamic motion of the ionic species in the diffuse layer and the accumulation of ions close to the electrode surface (**Figure 1.5**).

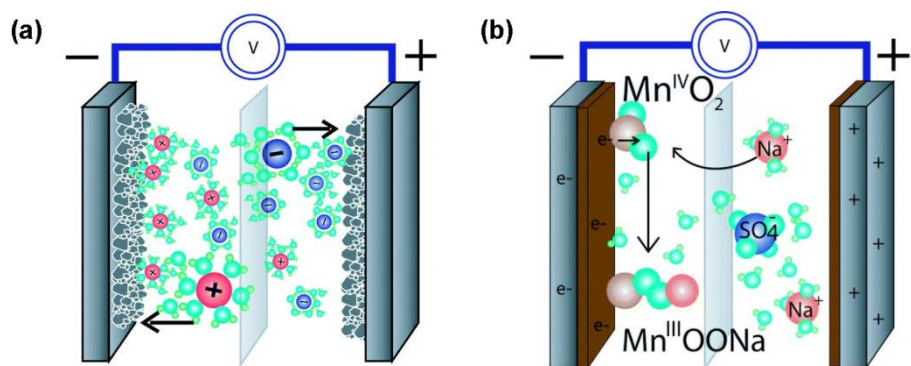


**Figure 1.4.** Basic schematics for an (a) all carbon EDLC, (b) a pseudocapacitor. (from Ref. [1] Jost *et al.*, *J. Mater. Chem. A*, **2014**, *2*, 10776-10787.)

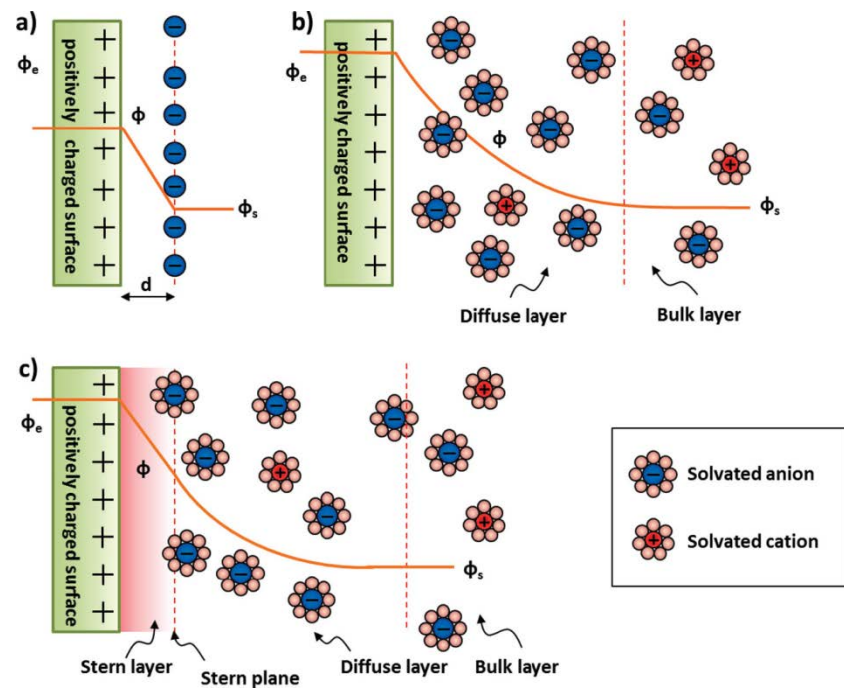


**Figure 1.5.** Schematic illustration of (a) Helmholtz, (b) Gouy-Chapman, and (c) Stern model of the electrical double-layer formed at a positively charged electrode in an aqueous electrolyte. (from Ref. [5] Beguin *et al.*, *Adv Mater*, **2014**, 26, 2219-2251.)

## 1.2 Heteroatom doped carbon materials

### 1.2.1 Carbon materials for supercapacitor applications

Electrode materials are considered as a crucial role in supercapacitors. Currently, carbon, conducting polymers, and metal oxides are proposed as supercapacitor electrode materials (**Figure 1.6**) [4]. Among these, activated, templated and carbide-derived carbons, carbon fabrics, fibers, nanotubes, onion-like and graphenes have been applied for EDLCs electrodes. Because these carbon materials exhibit high specific surface area, high electrical conductivity, rate capability, and long cycle stability.

There are two parameters for evaluating the electrochemical performance of supercapacitors. The maximum energy density ( $E$ ) and power density ( $P$ ) can be obtained by following equations [6]:

$$E (Wh kg^{-1}) = \frac{CV^2}{2}$$

$$P (W kg^{-1}) = \frac{V^2}{4R}$$

where  $C$  is capacitance,  $V$  is operating voltage, and  $R$  is equivalent series resistance.

However, EDLCs suffer from a limited energy density due to a consequence of electrostatic surface charging mechanism [2]. Therefore, EDLC researches are currently focused on improving the energy density by increasing specific capacitance of electrodes the operating voltage of cells. To improve specific capacitance, the strategies are focused on increasing the specific surface area, optimizing the pore size and pore size distribution by developing hierarchically porous structure without sacrificing the good electrical conductivity. Moreover, the high specific capacitance can be achieved by introducing redox species to contribute additional faradic pseudocapacitance such as heteroatom doping into carbon materials (**Figure 1.7**) [5, 7, 8].

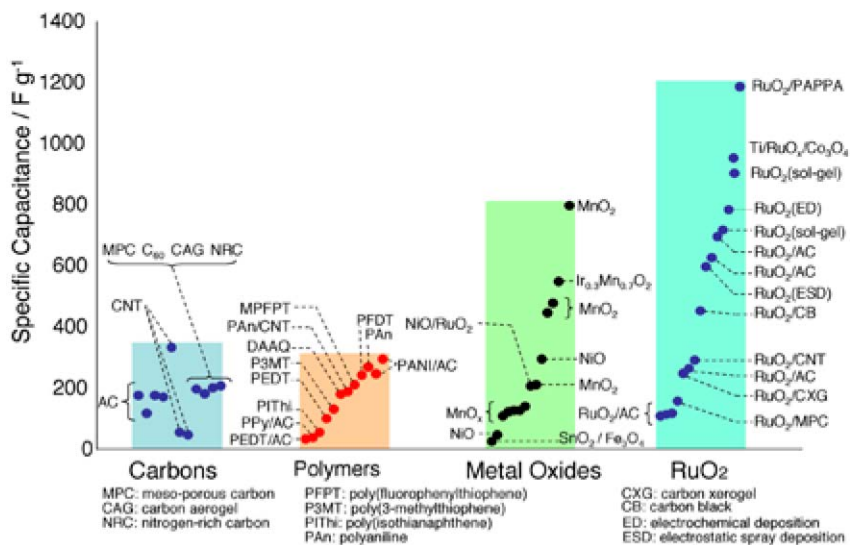


**Figure 1.6.** Various type of supercapacitor materials. (from Ref. [4] Rolison *et al.*, *Chem. Soc. Rev.*, **2009**, 38, 226-252.)

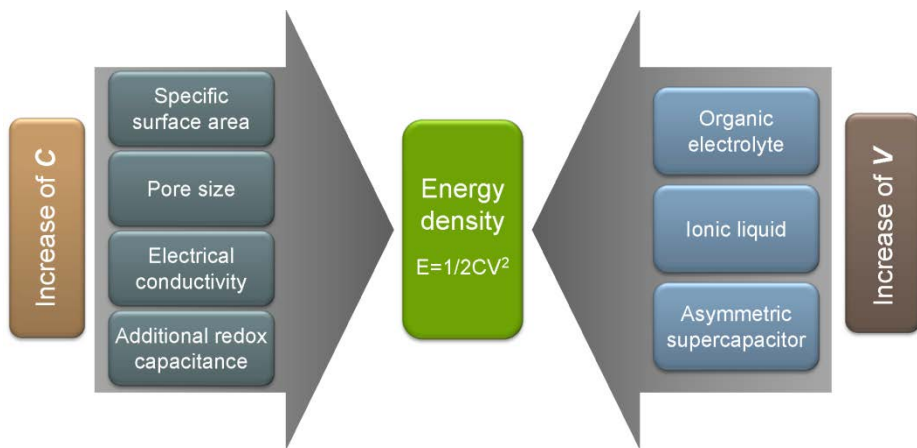


**Figure 1.7.** Schematic illustration of different approaches to improve energy density of a supercapacitor

### **1.2.2 Heteroatom doped carbons for supercapacitor applications**

One of the strategy to improve the energy density and cycle life of EDLCs involves the modification of surface functionality of the carbon materials, using elements such as nitrogen, oxygen, boron, or phosphorous. Heteroatom-doped carbon can enhance the capacitance and induce surface faradaic reactions by improving the charge mobility of negative charges on the carbon surface, while maintaining the high rate capability and long cycle life [9, 10].

### **1.2.3 Nitrogen doping**

Nitrogen doping is a mostly intensively explored for carbon materials because of their abundant resources in around. Introducing nitrogen atoms into carbon materials can enhance the spin density, asymmetric valance charge, and electron transfer ability of carbon-based materials because of their higher electronegativity properties. Moreover, the nitrogen doping can improve the wettability between electrode materials and electrolytes, which contributes increasing capacitance [11-13]. There are four different nitrogen configurations containing in

the carbon structure such as N-6 (pyridinic N), N-5 (pyrrolic N), N-Q (graphitic N), and N-O (oxidized N), respectively. As shown in the schematic in **Figure 1.8**, N-6 is substituted a carbon atom in a hexagone structure, which leads to great pseudocapacitance effect and improve the conductivity, resulting in enhanced capacitive performance. N-5 represents the nitrogen atoms in a five-membered ring and thus contributing two electrons to the  $\pi$ -system. N-Q is formed by substituting a carbon atom in a complete 2D honeycomb lattice, which can also enhance the electrical conductivity of materials [14].

Nitrogen-doped carbon materials can be prepared as active materials in one of two ways: post-treatment or *in situ*. The post-treatment pathway involves attaching nitrogen-containing functional groups such as urea [15], ammonia [16] and nitrogen plasma [17], but this pathway leads to relatively low nitrogen contents on the surface and an inhomogeneous nitrogen distribution. In the *in situ* pathway, nitrogen-containing precursors such as polypyrrole [18, 19], polyaniline [20-22], melanine [23], polyacrylonitrile [24] and nitrogen-containing ionic liquids undergo pyrolysis at high temperatures [25], directly converting them to nitrogen-doped carbon materials. Compared to post treatment, this method can realize homogeneous incorporation of nitrogen, and is

a more simple and facile way to utilize various precursors.

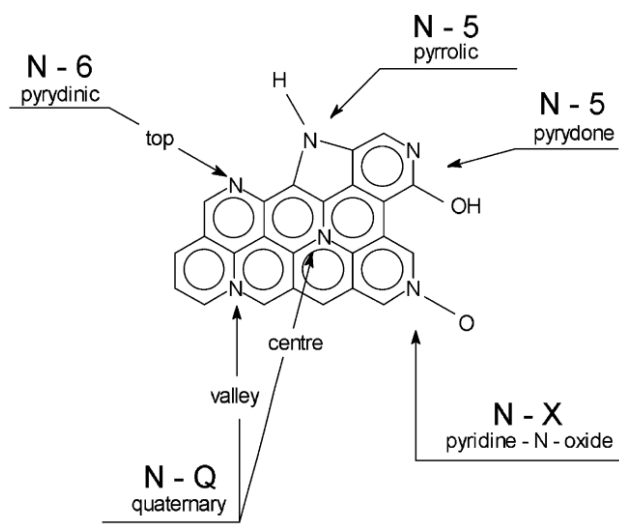


**Figure 1.8.** Distribution of nitrogen atoms in carbon graphene structure.  
 (from Ref. [13] Jurewicz *et al.*, *Electrochim. Acta*, **2003**, 48, 1491-1498.)

### **1.2.4 Fluorine doping**

Fluorine doping is another approach to enhance electrochemical performances of carbon materials. The highest electronegativity of fluorine atoms is capable of forming the fluorine-carbon bond with high polarity and stability. As a result, fluorine doped carbon can be enhanced rate capability, cycling stability and wettability [26, 27].

### **1.2.5 Sulfur doping**

Sulfur has lone-pair electrons and act as an electron donor, resulting to pseudocapacitance effects in carbon (**Figure 1.9**). Sulfur-doping can modify the electronic structure of carbon because of the sulfur atoms affecting  $\pi$  electrons in the carbon lattice. It can improve the electrical conductivity, surface reactivity and wettability [28-30].

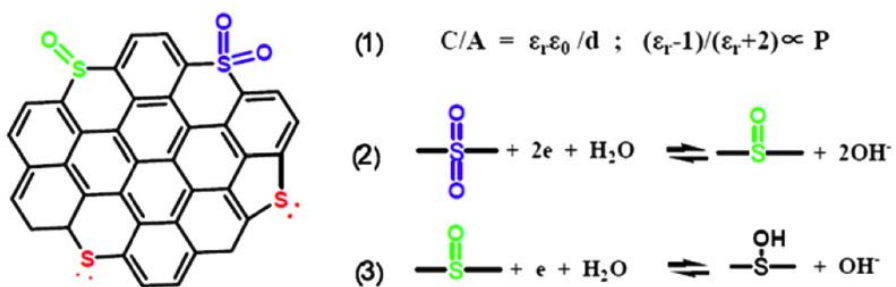


**Figure 1.9.** Schematic illustration of a proposed electrochemical performance mechanism on S-containing mesoporous carbon. (from Ref. [29] Zhao *et al*, *Nano Energy*, **2012**, 1, 624-630.)

### 1.2.6 Boron doping

Boron atom has three valence electrons and can substitute carbon with formations of boronic, borinic esters, and boronic acids (**Figure 1.10**). Substituted boron atoms in the carbon structure arise a shift in Fermi level to conduction band corresponding modification of the electronic structure of carbon. Furthermore, low-level boron doping exhibits catalytic effect on oxygen chemisorption on the carbon surface, resulting the introduction of redox reaction. As a result, boron doping can be modified the electrochemical capacitance of carbon materials [31, 32].

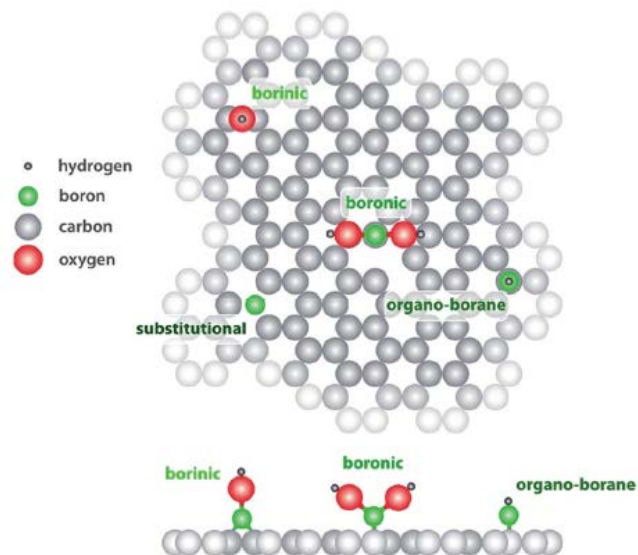


**Figure 1.10.** Ball model of B-G showing some of the most common boron induced defects. (from Ref. [32] Agnoli *et al.*, *J. Mater. Chem. A*, **2016**, 4, 5002-5025.)

### **1.2.7 Multiple heteroatom doping**

Nitrogen as a single heteroatom doping source has received much attention in recent years owing to its effect on the capacitance, ease of preparation, and relatively high abundance in nature. However, the strategy of co-doping of two or more heteroatoms into carbon atoms with nitrogen as a primary dopant can enhance electrochemical performance owing to their synergetic effects [10]. Having a synthetic method that can change the combination of various heteroatoms is a very important first step in studying the new synergies that we have not seen before and can be a new technique to design the properties of optimized materials for different applications.

Recently, research has focused on the development of multiple-heteroatom doping with diverse strategies. One of the strategies is using high-vacuum equipment such as chemical vapor deposition (CVD) or vacuum plasma treatment with gas as a doping source for introducing heteroatoms into carbon materials [33, 34]. Although this method allows easy control of the doping intensity, it has some drawbacks in terms of expensive equipment, hazardous gas, and difficulty in scaling up for commercial applications. Another approach

is prepared using toxic reagents (e.g.,  $\text{H}_2\text{SO}_4$ , HF,  $\text{HNO}_3$ ), which are dangerous and pose limitations for practical applications [35, 36]. Additionally, infiltration or stirring with a dopant solution is inhomogeneous and unable to control the doping concentration in the carbon structure [37]. Despite considerable interest and progress to date, it remains challenges to develop a novel, simple, un Hazardous, and time-saving preparation method for high-performance multiple-heteroatom-doped carbons.

## 1.3 Carbonized polyimides

### 1.3.1 Polyimides

Aromatic polymers, having conjugated aromatic rings in the polymer backbone, have excellent thermal stability and high carbon yield after pyrolysis compared to small organic precursors, making them useful nitrogen-containing precursors in this field. Recently, nitrogen-doped porous carbon nanofibers were prepared by carbonization of carbonaceous nanofibers coated with polypyrrole [38] and polyaniline [39] using a direct polymerization method.

One of the aromatic polymers, aromatic polyimides (API) are widely used in display, microelectronic, and aerospace technologies because of their high mechanical stability, thermal stability, chemical resistance, and low dielectric constants [40]. The general synthetic route of polyimide (PI) is a reaction of tetracarboxylic dianhydride with equimolar diamine in N-methyl-2-pyrrolidone (NMP) or N,N'-dimethylacetamide (DMAc), through dehydration reaction (**Figure 1.11**). Polyamic acid (PAA) is formed as an intermediate product by solution type with processable states. Finally, PAA is converted to PI by

chemical or thermal process [41, 42]. PIs have excellent properties of heat and chemical resistance, dimensional stability, and mechanical properties. Moreover, API is an effective carbon precursor due to its high carbon yield and ease of carbonization [41].

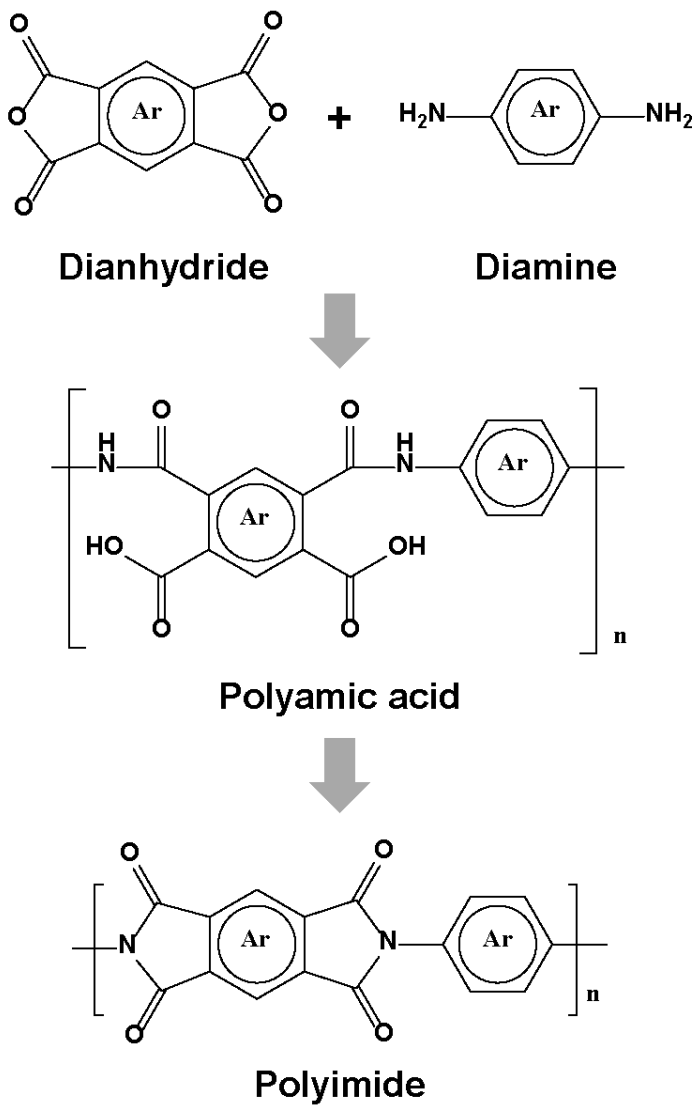


**Figure 1.11.** Synthetic scheme of polyimide.

### 1.3.2 Carbonized polyimides

PIs have also used as precursors for carbon materials followed by thermal process above 600 °C under inert atmosphere. One of the advantages of PIs as carbon precursors is a wide selectivities of diamines as well as dianhydrides, which is able to tune the morphology or functional groups of PI. The structure of carbon is highly dependent of molecular structure of PIs (**Figure 1.12**). Another advantage is a high carbon yield as well as no deformations after carbonization process (**Figure 1.13**). Kapton film consisted with pyromellitic dianhydride (PMDA) and 4,4'-oxydianiline (ODA) is obtained a carbon yield about 60% at 1000 °C with no cracks and a shrinkage [41, 43].

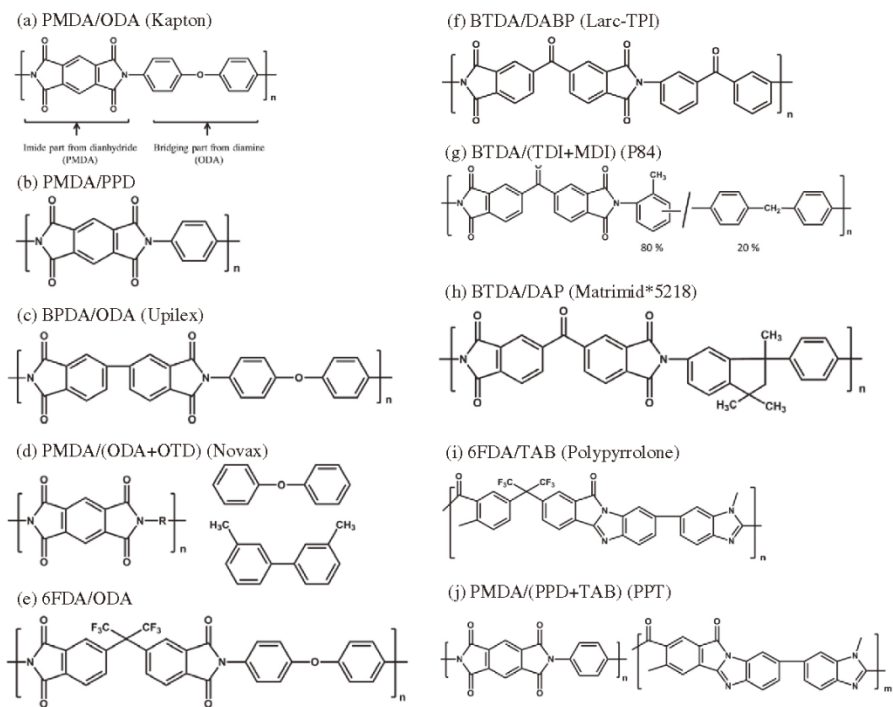


**Figure 1.12.** Various types of polyimide derivatives. (from Ref. [43])

Inagaki *et al.*, *Carbon*, **2013**, 61, 1-21.)

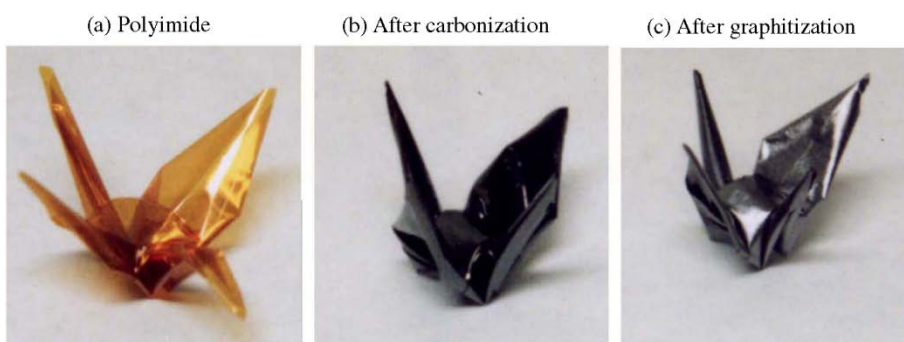


**Figure 1.13.** Thermal stability of crane made by PI film. (from Rfe. [43]  
Inagaki *et al.*, *Carbon*, **2013**, 61, 1-21.)

### 1.3.3 Carbonized polyimides for supercapacitor applications

As supercapacitor electrode materials, carbonized PIs are widely investigated with various types of electrodes. Electrospun nanofiber mats produced by electrospinning method have advantageous to obtain free-standing and binder-free type carbon electrode [44-47]. Le *et al.* demonstrated a micro-porous PI based carbon nanofiber mat prepared by polymer blend electrospinning technique and following thermal treatment without activation [44]. Polyvinyl pyrrolidone (PVP) was used as a forming template crosslinking with PI precursor via imidization process. The specific capacitance was achieved  $215 \text{ F g}^{-1}$  at a current density of  $0.2 \text{ A g}^{-1}$  based on a symmetrical two electrode system. For micro supercapacitor applications, PIs is used as a laser induced graphene source to fabricate active electrode [48, 49]. Peng *et al.* reported that boron-doped porous graphene was prepared by a facile laser induction process from boric acid containing polyimide sheets [48]. At the same time, active electrodes can be patterned for flexible micro supercapacitors. The obtained devices achieved an areal capacitance of  $16.5 \text{ mF cm}^{-2}$  and well-maintained a superb cyclability and flexibility. Xu *et al.* synthesized self-assembled 3D hierarchical

nanostructures by varying polymerization of PIs followed by activation process [50]. This 3D hierarchical shape is advantageous for a large specific surface area leading to improved specific capacitance of carbon electrodes. As a result, the specific capacitance was obtained  $364 \text{ F g}^{-1}$  at a current density of  $0.6 \text{ A g}^{-1}$ . The formation of composite with other carbon material such as is an alternative strategy for supercapacitor applications. Chen *et al.* prepared graphene composite electrodes deposited with PIs by molecular layer deposition (MLD) method followed by carbonization process [51]. The utilization of MLD method allows uniform coating of PI layers on the surface of pristine graphene without any surface treatments. The composite electrodes showed a specific capacitance of  $290.2 \text{ F g}^{-1}$  at a current density of  $1 \text{ A g}^{-1}$ .

## 1.4 Carbon textiles

### 1.4.1 Carbon textiles for supercapacitor applications

Many efforts have been made to realize flexible supercapacitors with robust mechanical properties and excellent electrochemical performance, to ensure operation in extreme conditions. Possible flexible substrates for supercapacitors include polyethylene-terephthalate films [52], carbon material integrated office paper [53], carbon nanofibers [54], graphene paper [55], carbon nanotube fibers [56], and graphene fibers [57]. Among these, textile-based substrates show great promise for use as flexible supercapacitor substrates. Carbon cloth (CC) is particularly attractive in this regard, as CC is a textile of carbon fiber bundles approximately 5  $\mu\text{m}$  in diameter, granting it light weight, flexibility, mechanical strength, thermal stability, electrical conductivity, and chemical resistance (**Figure 1.14**) [58].

However, it is still a significant challenge to achieve high energy density and long cycle life in flexible supercapacitors. A typical fabrication of all-solid-state flexible supercapacitor cells needs an

additional binder or other additive to integrate the active materials on current collector surfaces, resulting in large contact resistance and dead surface areas on the electrode materials [59]. In response to this, researchers have begun developing direct fabrication processes of active materials onto CC surfaces using *in situ* growth strategies. Various methods, including electrodeposition of conductive polymers [60] or metal oxides [61], hydrothermal growth of metal oxides [62, 63], *in situ* chemical polymerization of conducting polymers [64], and surface activation of CC [58, 65], have been demonstrated to achieve binder-free fabrication of active materials in such systems. However, control over the loading mass of active material on the CC surface is a challenge for commercialization, especially in regards to high specific capacitance and large scale production.



Substrate (w/o MPL)			Carbon Cloth
Property	Units	Method	W0S1002
Thickness	um	TECLOCK SM-114	360
Basic Weight	g/m <sup>2</sup>	ASTM D-846	125
Air Permeability	sec	Gurley Method*	<6
Through-Plane Resistance	mΩcm <sup>2</sup>	Base on ASTM C-611**	<5
Tensile Strength	MD	N/cm	19
	XD	N/cm	5

Produced by CeTech Co., Ltd.

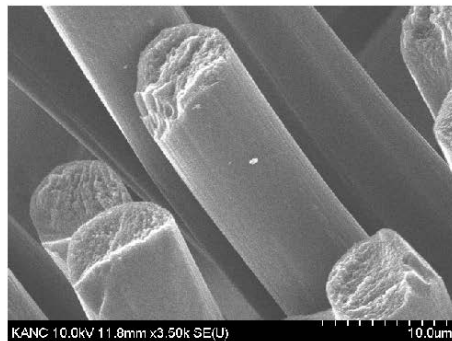
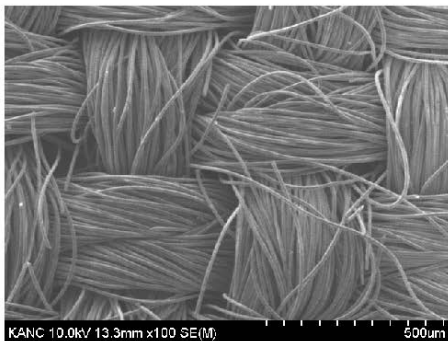


**Figure 1.14.** Carbon cloth (W0S1002 produced form CeTech Co., Ltd.) product specification and SEM images.

## 1.5 Objectives

This thesis is mainly focused on the developments of various types of heteroatom doped carbon materials derived from PI precursors by *in situ* doping techniques to improve the low capacitance and energy density of carbon electrodes and the investigations of their doping effects in electrochemical performances.

In the first part, nitrogen-doped carbons derived from polyimide/MWCNT composites for flexible all-solid-state symmetric supercapacitors are discussed. For this purpose, as a nitrogen-doped carbon precursor, aminophenyl multiwall carbon nanotube grafted PI precursor is synthesized by *in situ* polymerization method. The synthesized MWCNT/PI composites precursor solution is dropped to the carbon cloth surface which is served as the flexible substrate and current collector and coating followed by direct carbonization at high temperature. These suggested process for the fabrication of electrodes effectively solves the technical problems of the control of the loading mass of active material on the CC surface, and the difficulty of large scale production.

In the second part, the preparation of multiple-heteroatom-doped

carbons (from single- to triple-doped) derived from polyimide precursors with pyrolysis strategy is discussed. The heteroatoms incorporated into a carbon matrix can be tuned by varying the functional groups in diamine or dianhydride monomers and doped by *in situ* methods following pyrolysis. N, N,S-, N,F-, N,S,B-, and N,F,B-doped carbons derived from polyimide precursors are prepared and systematically investigated in terms of heteroatom doping effects.

In the third part, a facile approach to synthesis of N-, B-co-doped carbon using PI precursors and  $\text{NH}_3\text{BH}_3$  as nitrogen and boron doping sources, respectively is investigated. During the carbonization process,  $\text{NH}_3\text{BH}_3$  will be decomposed and released boron atoms as well as nitrogen atoms. Owing to N-, B-co-doping effects, N-, B-co-doped carbon enhanced a specific capacitance and capacitance retention compared with N-doped carbon in a three-electrode system is discussed.

## **Chapter 2. Experiment**

### **2.1 Synthesis of heteroatom doped carbon precursors**

#### **2.1.1 Nitrogen doped carbon derived from polyimide/multiwall carbon nanotube composites**

##### **2.1.1.1 Synthesis of MWCNT-PI nanocomposite precursor**

Aminophenyl functionalized MWCNT (AP-MWCNT) was prepared according to reference [66]. The as-prepared AP-MWCNT (36 mg) were dispersed in N,N-dimethylformamide (DMF, 15 mL) and the solution subjected to ultrasonication for 1 h. Then, 4,4'-oxydianiline (0.59 g, 2.75 mmol) was added to the solution and stirred for 30 min. Subsequently, pyromellitic dianhydride (0.60 g, 2.75 mmol) was added to the mixture with stirring for 24 h at room temperature, yielding the MWCNT-PI precursor with the desired viscosity.

## **2.1.2 Multiple-heteroatom-doped carbon derived from polyimide precursors**

### **2.1.2.1 Synthesis of NCP precursor**

Nitrogen doped carbonized PI (NCP) precursor solution was prepared as follows: diamine monomer 4,4'-oxydianiline (1.0 g, 4.9 mmol) was dissolved in DMF (8.4 g, solid content in 20 wt%) and stirred until completely dissolved under an argon atmosphere. After that, pyromellitic dianhydride (1.1 g, 4.9 mmol) was added. The mixed solution was polymerized at room temperature for 1 day.

### **2.1.2.2 Synthesis of NSCP precursor**

Nitrogen, sulfur-co-doped carbonized PI (NSCP) precursor solution was prepared as follows: 4,4'-thiodianiline (1.0 g, 4.6 mmol) and 4, 4'-[p-thiobis(phenylenesulfanyl)]diphthalic anhydride (2.5 g, 4.6 mmol) was mixed with DMF (5.3 g, solid content in 40 wt%). The mixed solution was polymerized at room temperature for 1 day.

### **2.1.2.3 Synthesis of NFCP precursor**

Nitrogen, fluorine-co-doped carbonized PI (NFCP) precursor solution was prepared as follows: diamine monomer 4,4'-oxydianiline (1.0 g, 4.9 mmol) was added to a flask with DMF (10.8 g, solid content in 23 wt%) and stirred until completely dissolved under an argon atmosphere. After that, 4,4'-(hexafluoroisopropylidene) diphthalic anhydride (2.2 g, 4.9 mmol) was added. The mixed solution was polymerized at room temperature for 1 day to obtain the NFCP precursor solution.

### **2.1.2.4 Synthesis of NSBCP precursor**

Nitrogen, sulfur, boron-triple-doped carbonized PI (NSBCP) precursor solution was prepared as follows: boric acid (0.028 g) was added into 1 g of NSCP precursor solution and stirred until clearly dissolved.

### **2.1.2.5 Synthesis of NFBCP precursor**

Nitrogen, fluorine, boron-triple-doped carbonized PI (NFBCP) precursor solution was prepared as follows: boric acid (0.014 g) was added into 1 g of NFBCP precursor solution and stirred until clearly dissolved.

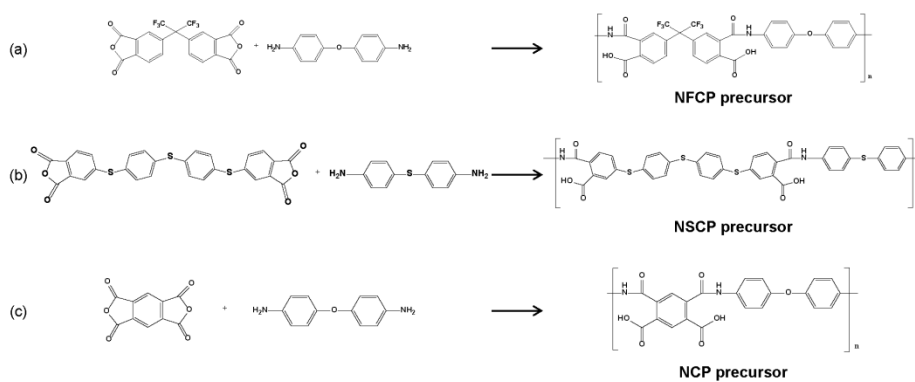


**Figure 2.1.** Synthetic scheme of (a) NFCP, (b) NSCP, and (c) NCP precursors.

## **2.1.3 Nitrogen- and boron-co-doped carbon derived from polyimide precursors**

### **2.1.3.1 Synthesis of PI precursors**

In a typical synthesis procedure, 4.9 mmol of 4,4'-oxydianiline was completely dissolved in 6.3 g of DMF by stirring under an Ar atmosphere. Subsequently, 4.9 mmol of pyromellitic dianhydride was added. The mixed solution was polymerized at room temperature for 1 day to acquire the PI precursor in solution. The solid content of the synthesized PI solution was 25 wt%.

### **2.1.3.2 Synthesis of NBCP precursors**

Various amounts of  $\text{NH}_3\text{BH}_3$  (0.075 g for 3 wt%, 0.125 g for 5 wt%, and 0.175 g for 7 wt%) were added to 1 g of the 25 wt% PI precursor solution and stirred until dissolved completely.

## **2.2 Fabrication of heteroatom doped carbon electrodes**

In order to form a conformal coating of precursor solution, carbon cloth (CC) (CeTech Co. Ltd. W0S1002) was treated with DI water/ethanol (7/3 v/v) at 80 °C in a water bath overnight. The treated CC was dried in a vacuum oven at 60 °C for 2 h. A desired amount of precursor solution was dropped uniformly on a 1 cm × 1 cm area of the CC surface. Thermal treatment was performed by increasing the temperature at a rate of 3 °C min<sup>-1</sup> and maintained at targeting temperature for additional 1 h under N<sub>2</sub>.

## **2.3 Fabrication of all-solid-state symmetric supercapacitors**

To prepare PVA-H<sub>2</sub>SO<sub>4</sub> gel electrolyte, 1 g of PVA was mixed with 10 mL of 1 M H<sub>2</sub>SO<sub>4</sub> solution, and the mixture was vigorously stirred at 100 °C until a clear homogeneous solution was obtained. Two pieces of heteroatom doped carbon electrodes were immersed in PVA-H<sub>2</sub>SO<sub>4</sub> gel electrolyte for 1 h to allow the electrolyte to uniformly wet the electrodes. These electrodes were then left in a fume hood for 5 h to evaporate the excess water. Finally, the two pieces of electrodes were

sandwiched together with the electrolyte wetted filter paper as a separator. The total volume of the symmetric supercapacitor was around  $0.3 \text{ cm}^3$  (working area:  $3.0 \text{ cm}^2$ , total height including two electrodes and separator:  $\sim 0.1 \text{ cm}$ ).

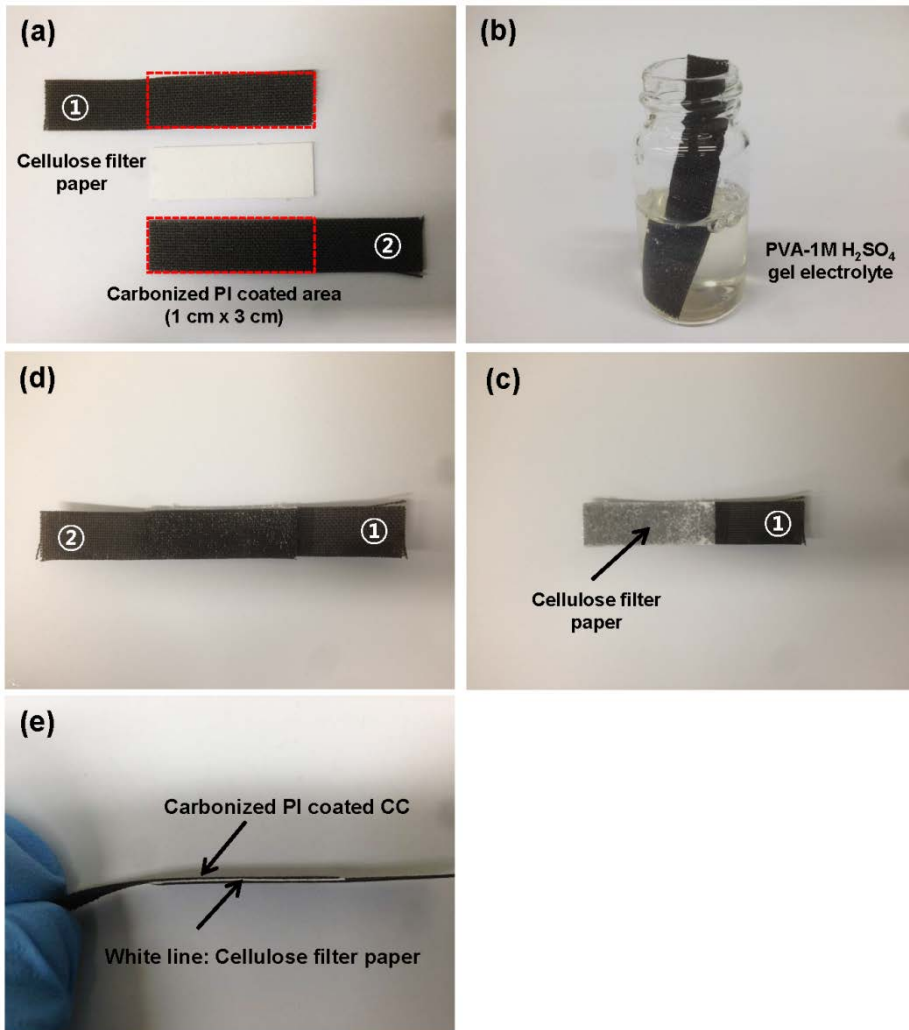


**Figure 2.2.** Fabrication scheme of all-solid-state symmetric supercapacitors.

## **2.4 Material characterization**

The morphologies and microstructures of these systems were investigated by FE-SEM (Hitachi S-4800). XPS spectra were measured using an AXIS-His spectrometer with a monochromatic Al K $\alpha$  source. Raman analysis was conducted using a Horiba T64000 model Raman spectrometer. A Mettler Toledo TGA/DSC 1 model thermogravimetric analyzer was used for TGA.

## **2.5 Electrochemical measurements**

Electrochemical measurements were performed by using a CHI660E (CH Instruments Inc., USA) electrochemical workstation. In a three electrode system, the as-prepared binder-free heteroatom doped carbon coated CC was directly used as a working electrode without any current collector. The mass loading of active material on the CC surface was about 2.5~3 mg cm<sup>-2</sup>. A Pt mesh electrode and an Ag/AgCl electrode were used as the counter and reference electrodes, respectively. All tests were performed in 1 M H<sub>2</sub>SO<sub>4</sub> aqueous electrolyte at room temperature with potential range from 0.0 to 1.0 V. Electrochemical impedance

spectroscopy (EIS) was measured using an AC amplitude of 5 mV over a frequency range of 0.01 Hz – 1 MHz at an open circuit potential.

The specific capacitance was calculated from galvanostatic charge-discharge (GCD) curves according to the following equation [7]:

$$C_s = \frac{I \times \Delta t}{\Delta V \times m} \quad (1)$$

where  $C_s$  ( $F g^{-1}$ ) is the gravimetric specific capacitance,  $I$  is the discharge current (A),  $\Delta t$  is the discharge time (s),  $\Delta V$  (v) is the potential window of discharge curve excluding voltage drop at the starting of discharge ( $IR$  drop), and  $m$  is the mass of active material (g).

Volumetric capacitance of the device was calculated according to the following equation [61]:

$$C_v = \frac{I \times \Delta t}{\Delta V \times v} \quad (2)$$

where  $C_v$  ( $F cm^{-3}$ ) is the volumetric capacitance of the device and  $v$  is the total volume of the device ( $cm^3$ ).

The volumetric energy density  $E$  ( $Wh cm^{-3}$ ) and power density  $P$

(W cm<sup>-3</sup>) of device were calculated with following equations [61]:

$$E = \frac{C_v(\Delta V)^2}{2} \times \frac{1}{3600} \quad (3)$$

$$P = \frac{E \times 3600}{\Delta t} \quad (4)$$

## Chapter 3. Results and Discussion

### 3.1 Nitrogen doped carbon derived from polyimide/multiwall carbon nanotube composites

#### 3.1.1 Physical and chemical analysis

Schematic illustrations of the flexible CC/carbonized MWCNT-PI composites electrodes are shown in **Figure. 3.1**. A controlled amount of AP-MWCNT-polyamic acid (PAA) solution was dropped and coated onto the CC surface. After evaporating the solvent, additional thermal processing was performed at 300 °C, 600 °C, 800 °C, and 1000 °C to convert the carbon present; the resulting samples are designated as CC/MWCNT-PI-300, CC/C-MWCNT-PI-600, CC/C-MWCNT-PI-800, and CC/C-MWCNT-PI-1000, respectively. As a reference sample, pure PAA solution without AP-MWCNT coated CC was heated at 800 °C and designated as CC/C-PI-800. During high temperature pyrolysis, AP-MWCNT-grafted API precursors are converted into nitrogen-doped carbon materials. The carbonized AP-MWCNT-PIs are tightly connected to the flexible and electrically conductive CC, which can be

directly used as an electrode without any binders or additives; these traits make for superior supercapacitor electrode design without sacrificing energy storage capacity or reducing electrical conductivity. Previously, we reported that AP-MWCNT was grafted via *in situ* polymerization to enhance the dispersity of MWCNT in the polymer matrix [66]. AP-MWCNT can not only enhance the nitrogen doping contents of AP-MWCNT-API nanocomposites after carbonization (compared to pure API), but also improve the dispersion stability of MWCNT in polymer matrices. As a result, the electrical conductivity and mechanical properties of AP-MWCNT grafted PI were improved compared to those of pure PI due to the incorporation of MWCNT in the PI matrix. Therefore, we expected that carbonized MWCNT-grafted PI will feature enhanced supercapacitive behavior in this study.

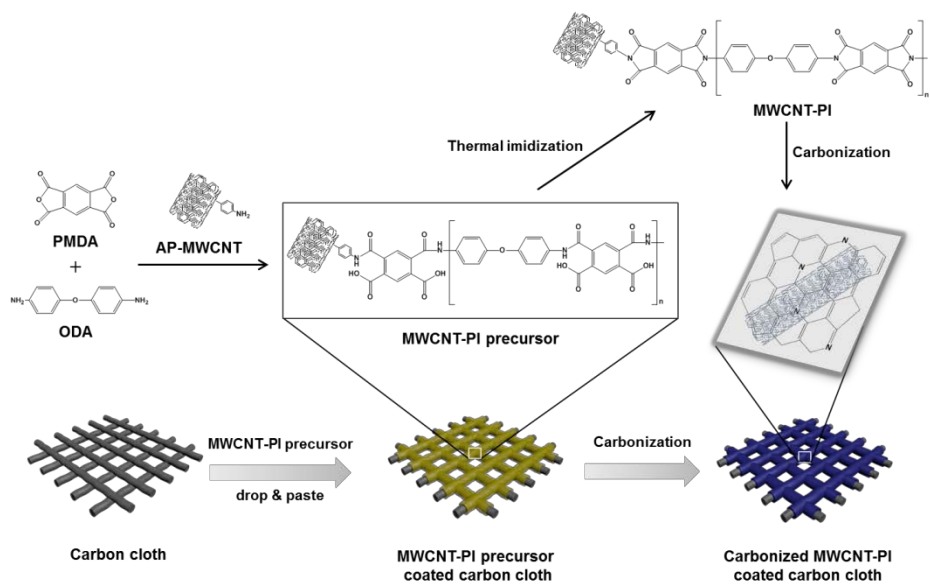


**Figure 3.1.** Schematic illustration of the preparation of flexible CC/C-MWCNT-PI electrodes.

We examined the conductivity of all samples using a four-point probe measurement method. As the carbonization temperature increased from 300 °C to 1000 °C, the sheet resistance of the carbonized MWCNT-grafted PI decreased from 2.2 to 0.42 Ohm sq<sup>-1</sup>. With fixed carbonization temperature of 800 °C, the incorporation of MWCNT in the carbonized PI decreased the sheet resistance from 0.63 to 0.51 Ohm sq<sup>-1</sup> (**Figure 3.2**). Woven CC also has good flexibility and conductive properties, as well as high thermal stability and chemical resistance. The micro-sized woven pattern provided a large accessible area for the electrolyte, reducing ion transport resistance between the electrode and electrolyte at high scan rates [67]. Due to the high thermal stability of CC, direct carbonization with PI is possible above 800 °C.

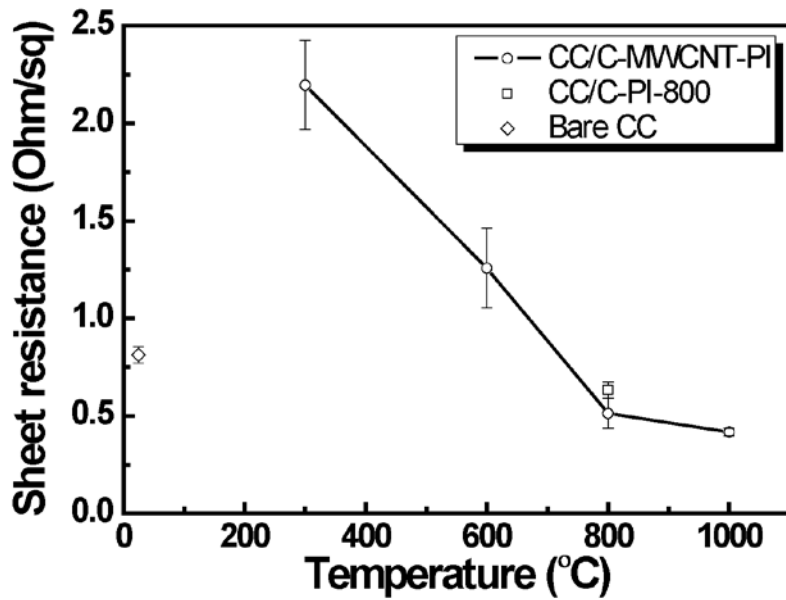


**Figure 3.2.** Plot of the carbonization temperature vs. the sheet resistance of CC/C-MWCNT-PI.

The morphology and microstructure were investigated using scanning electron microscopy (SEM), as shown in **Figure 3.3 and 3.4**. The images of bare CC (**Figure 3.3a and d**) reveal that the surface features interlaced carbon fibers with diameters of approximately 10  $\mu\text{m}$  and smooth surfaces. In **Figure 3.3b and e**, the MWCNT-PI precursor fully covers the CC surface at approximately 1  $\mu\text{m}$  thickness after heat treatment at 300  $^{\circ}\text{C}$ . Furthermore, we can observe that MWCNT bundles are exposed on the vertical surface of carbonized PI based on high-resolution SEM imaging (**Figure 3.3e**). This demonstrates that the MWCNT is well distributed in the polymer matrix after *in situ* polymerization. The as-prepared CC/MWCNT-PI-300 was carbonized at 600, 800, and 1000  $^{\circ}\text{C}$ . As shown in Fig. **Figure 3.3c, f and 3.4**, the initial morphology of the MWCNT-PI with CC is retained at all temperatures. As a reference, a pure polyimide precursor coated on CC was carbonized at 800  $^{\circ}\text{C}$ , and also maintained its morphology after heat treatment. These results indicate the potential applications of binder-free supercapacitor electrodes.

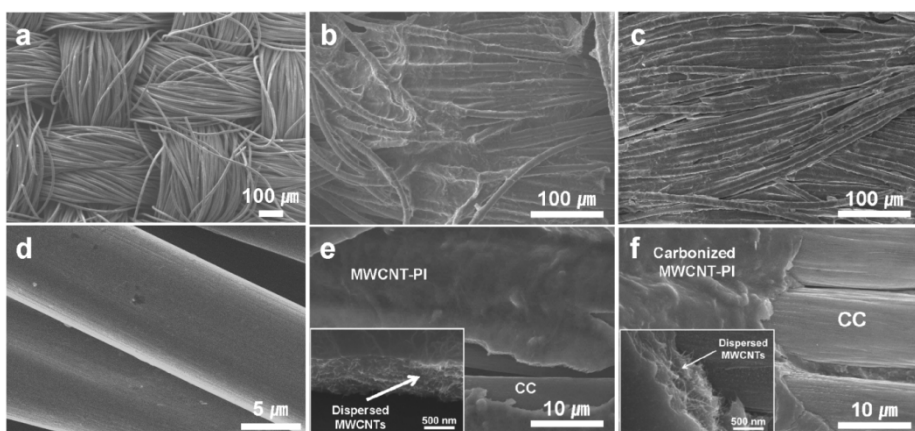


**Figure 3.3.** SEM images of CC, CC/MWCNT-PI-300, and CC/C-MWCNT-PI-800. (a), (d) CC, (b), (e) CC/MWCNT-PI-300 and (c), (f) CC/C-MWCNT-PI-800. The insets in (e), and (f) are high resolution SEM images of CC/MWCNT-PI-300 and CC/C-MWCNT-PI-800, respectively.

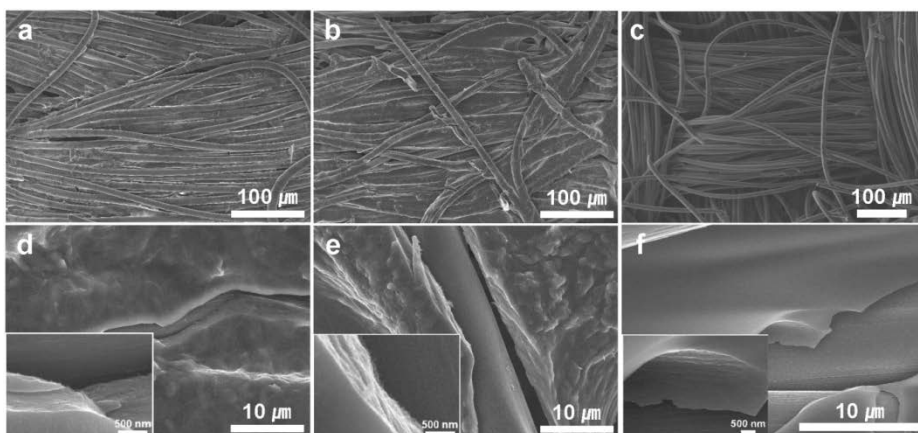


**Figure 3.4.** SEM images of (a), (d) CC/C-MWCNT-PI-600, (b), (e) CC/C-MWCNT-PI-1000 and (c), (f) CC/C-PI-800. The insets in (d), (e), and (f) are high resolution of SEM images of CC/C-MWCNT-PI-600, CC/C-MWCNT-PI-1000, and CC/C-MWCNT-PI-800, respectively.

Thermal stability is an important property for polymer driven carbon materials to achieve high carbon yields. To investigate these thermal properties, thermogravimetric analysis (TGA) was performed under N<sub>2</sub> as shown in **Figure 3.5**. Bare CC shows a very low weight loss of 4 % at 1000 °C, indicating high thermal stability and suitability for use as a current collector for high thermal processing. The CC/MWCNT-PI precursor shows two main TGA peaks at 100–260 °C, and 530–630 °C, which correspond to imidization and carbonization steps, respectively [41]. The TGA graph of CC/MWCNT-PI precursor exhibits slight degradation of carbon after the carbonization step (above 630 °C). From these results, we can infer that CC/MWCNT-PI-300 is a PI state and also that CC/C-MWCNT-PI-600 is not yet fully carbonized. The thermal stability of CC/C-MWCNT-PI (21% weight loss at 1000 °C) is higher than that of CC/C-PI (43% weight loss at 1000 °C) due to the incorporation of MWCNT in the polyimide precursor matrix.

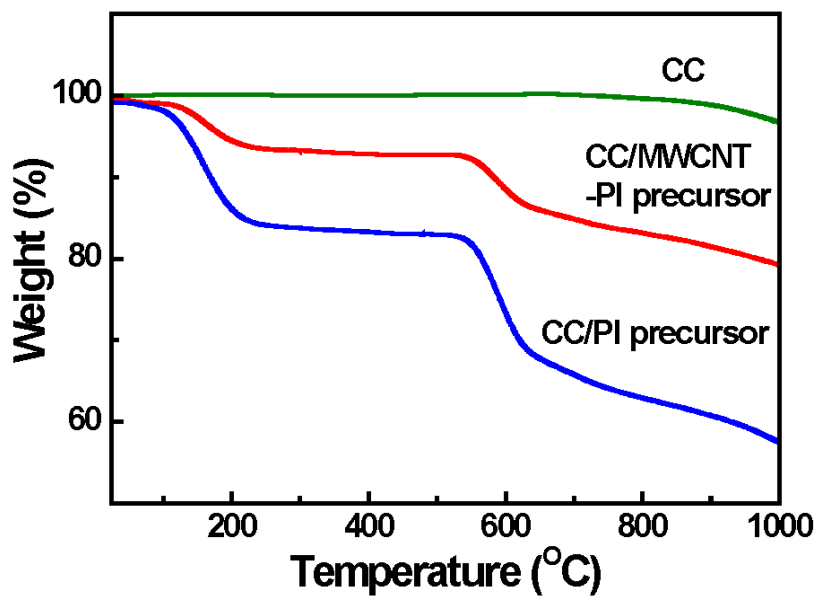


**Figure 3.5.** TGA analysis of CC, CC/PI precursor, and CC/MWCNT-PI precursor.

The carbon phase formation and structural features arising during carbonization were evaluated by Raman spectroscopy. As shown in **Figure 3.6**, the Raman spectra of CC, CC/C-PI-800, and CC/C-MWCNT-PI-800 show two prominent peaks at  $\sim 1361\text{ cm}^{-1}$  and  $\sim 1602\text{ cm}^{-1}$ , attributed to the D band and G band respectively. The D band is the vibration of the disordered carbon structure with various defects, and the G band is  $\text{sp}^2$ -bonded carbon atoms in a two dimensional hexagonal lattice [68, 69]. The  $I_D/I_G$  ratios of CC, CC/C-PI-800, and CC/C-MWCNT-PI-800 are 0.828, 0.820, and 0.687, respectively. The changes to the  $I_D/I_G$  ratio reveal that the coated PI precursors were successfully carbonized on the CC surface. The  $I_D/I_G$  ratio of CC/C-MWCNT-PI-800 is lower than that of CC/C-PI-800, indicating a larger graphitization ratio in CC/C-MWCNT-PI-800 due to the graphitic MWCNT structures in the carbon films [70].

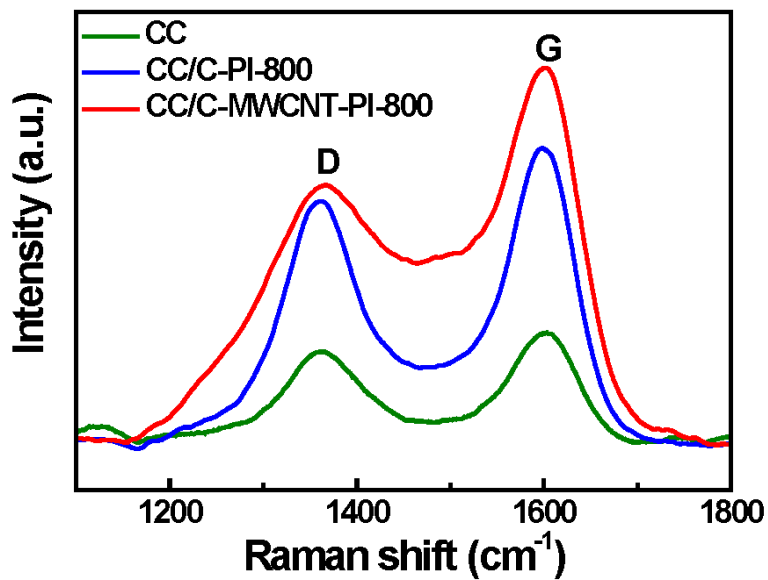


**Figure 3.6.** Raman spectra of CC, CC/C-PI-800, and CC/C-MWCNT-PI-800.

The nitrogen doping effects of CC/MWCNT-PI during thermal processing were evaluated by X-ray photoelectron spectroscopy (XPS), as presented in **Figure 3.7 and 3.8**. The low resolution XPS spectra of all samples (**Figure 3.7**) show peaks for nitrogen (400 eV) and oxygen (532 eV), which both indicate enhanced pseudocapacitance properties, improved wettability and increased conductivity. As shown in **Table 3.1**, the nitrogen contents decreased as the heat treatment temperature increased; the nitrogen contents were 6.73, 6.24, 2.78, and 1.29 atomic % for CC/MWCNT-PI-300, CC/C-MWCNT-PI-600, CC/C-MWCNT-PI-800, and CC/C-MWCNT-PI-1000, respectively. The nitrogen content of CC/C-PI-800 is lower than that of CC/C-MWCNT-PI-800, as caused by the amine-functionalized MWCNTs. The high-resolution peaks of N1s for all samples (**Figure 3.8**) were deconvoluted into four individual peaks centered at 398.5, 400.3, 400.9, and 402 eV, corresponding to the pyridinic (N-6), pyrrolic or pyridonic (N-5), quaternary (N-Q), and oxidized (N-X) forms respectively [38, 71]. Notably, N-6 and N-5 are considered as electrochemically active sites to provide main pseudocapacitance. N-Q is located into the carbon matrix and bonded to three carbon atoms, which can effectively benefit electron transfer and improve the conductivity of carbonaceous materials [69].

CC/MWCNT-PI-300 shows only the N-5 peak, due to the nitrogen atoms in the PI structure before carbonization. Increasing the heat treatment temperature causes the N-5 peak to disappear, and the N-6 and N-Q peaks become dominant in the cases of CC/C-MWCNT-PI-600, CC/C-MWCNT-PI-800, and CC/C-MWCNT-PI-1000, due to the transformation of amine groups in PI after thermal treatment. The N-6 state, which makes for effective active sites, can increase the accessible surface area of C-MWCNT-PI and the specific capacitance [39]. The N-Q state can improve the conductivity of carbon materials due to its higher stability at high temperatures compared to N-6 [69]. When introducing the MWCNTs into the polymer matrix, the nitrogen content increases from 1.55% to 2.78% at 800 °C due to amine group functionalization of MWNT for *in situ* polymerization with diamines. These as-prepared C-MWCNT-PI with nitrogen doping and conductive framework structure demonstrate excellent electrochemical performance.

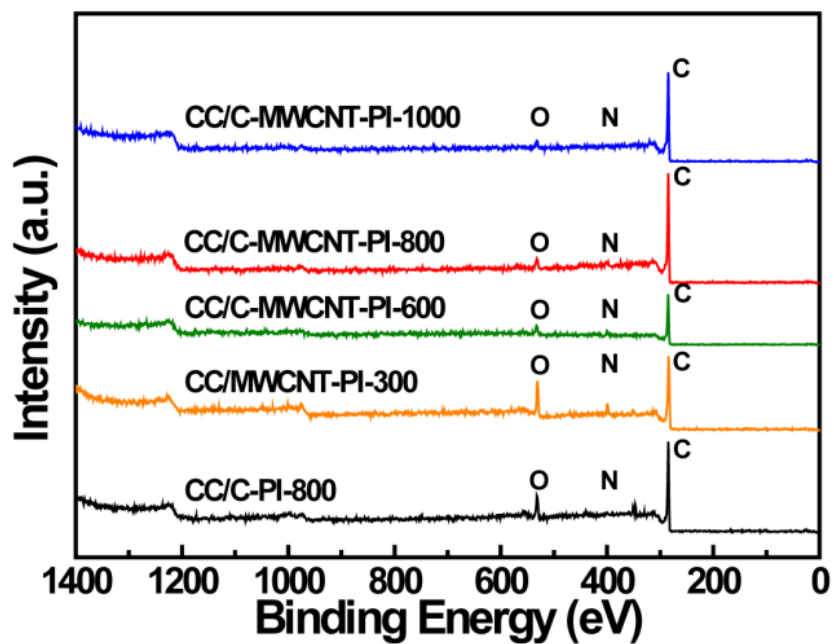


**Figure 3.7.** Low resolution XPS spectra of CC/C-MWCNT-PI-1000, CC/C-MWCNT-PI-800, CC/C-MWCNT-PI-600, CC/MWCNT-PI-300, and CC/C-PI-800.

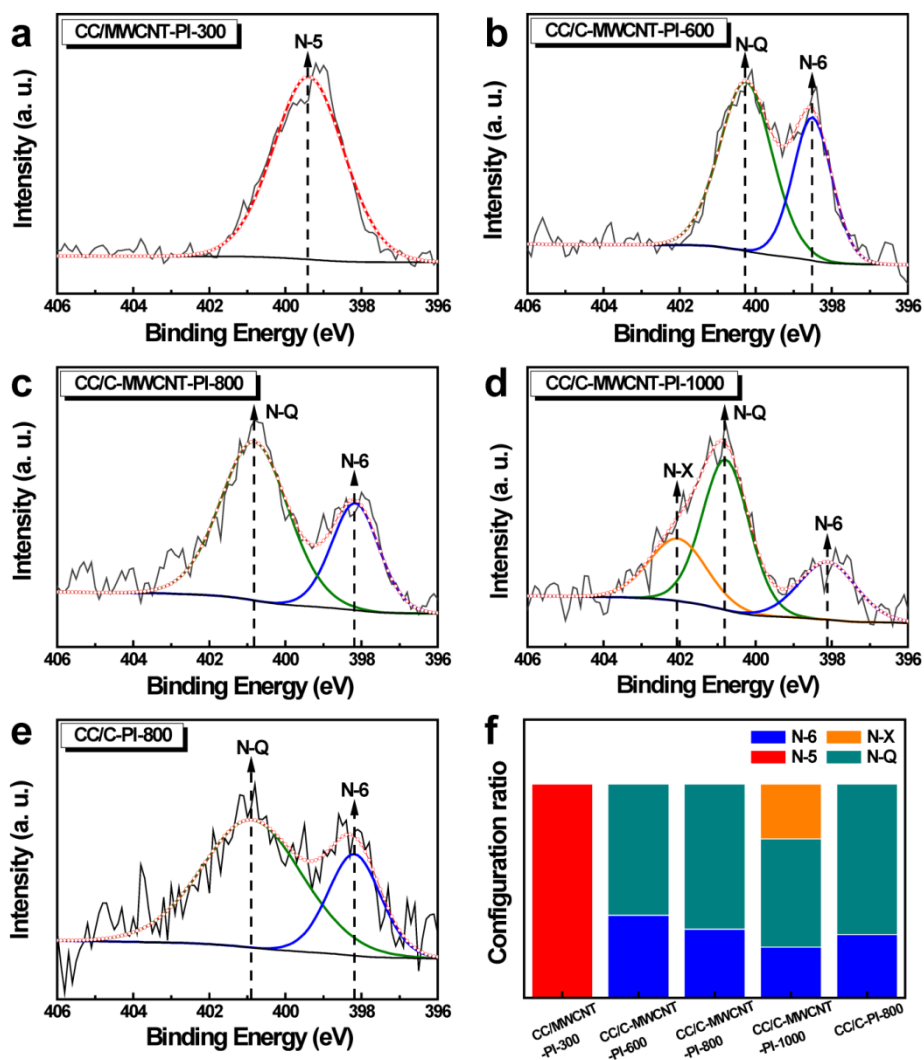


**Figure 3.8.** High resolution XPS spectra of N1s. (a) CC/MWCNT-PI-300, (b) CC/C-MWCNT-PI-600, (c) CC/C-MWCNT-PI-800, (d) CC/C-MWCNT-PI-1000, (e) CC/C-PI-800 and (f) nitrogen configuration ratio of all samples.

**Table 3.1.** Elemental analysis and relative contents of functional groups in N1s peaks obtained by XPS.

Sample	Atom %			N 1s <sup>a)</sup>			
	C	N	O	N-5	N-6	N-Q	N-X
CC/MWCNT-PI-300	78.1	6.73	15.17	6.73	-	-	-
CC/C-MWCNT-PI-600	84.16	6.24	9.6	-	2.41	3.83	-
CC/C-MWCNT-PI-800	92.28	2.78	4.94	-	0.89	1.89	-
CC/C-MWCNT-PI-1000	93.96	1.29	4.76	-	0.31	0.65	0.33
CC/C-PI-800	86.25	1.55	12.2	-	0.46	1.09	-

<sup>a)</sup> relative contents of functional groups in N 1s.

### 3.1.2 Electrochemical activity measurements

The capacitive performance of CC/C-MWCNT-PI for supercapacitors was investigated using a typical three electrode cell in 1 M H<sub>2</sub>SO<sub>4</sub> electrolyte, with Ag/AgCl and Pt mesh as the reference and counter electrodes, respectively. **Figure 3.9a** shows cyclic voltammetry (CV) curves for samples prepared at different thermal treatment temperatures, performed at a scan rate of 10 mV s<sup>-1</sup> within a potential range of 0.0–1.0 V s<sup>-1</sup>. CC and CC/MWCNT-PI-300 show very small rectangular shape curve corresponding to low electrochemical capacitance due to low surface area of CC or no carbonization state. The redox peaks at 0.4–0.6 V observed in CC/C-MWCNT-PI-600 indicate pseudocapacitance, likely due to the high nitrogen contents. The nearly rectangular shape of the CV curves for samples carbonized above 600 °C show electric double-layer capacitive behavior. The disappearance of some redox peaks at high temperatures is due to the decrease of nitrogen contents in the carbonized MWCNT-PI electrode, as confirmed by XPS [72]. **Figure 3.9b** compares the specific capacitances at different current densities as derived from charge-discharge curves based on active material mass. CC/C-MWCNT-PI-800

shows a specific capacitance value of  $333.4 \text{ F g}^{-1}$  at a current density of  $1 \text{ A g}^{-1}$ , better than CC/C-MWCNT-PI-600, CC/C-MWCNT-PI-1000, and CC/C-PI-800. The nitrogen doping on the surface of carbonized CC/C-MWCNT-800 enhances the wettability in the electrolyte and the electrical conductivity, both of which are beneficial for ion and electron transport (**Figure 3.11**). To the best of our knowledge, this is the highest capacitance among known nitrogen-doped carbon fibers (**Table 3.2**). **Figure 3.9c** shows the CV of CC/C-MWCNT-PI-800 at different scan rates of  $5\text{--}100 \text{ mV s}^{-1}$  in  $1 \text{ M H}_2\text{SO}_4$  electrolyte. The CV curves have quasi-rectangular shapes due to EDLC contributions. The charge-discharge curves at different current densities are shown in **Figure 3.9d**. The curves exhibit nearly triangular shapes and small internal resistance (*IR*) drop, indicating their effective EDLC and ion diffusion properties. Cycling stability is another requirement for optimal supercapacitor application, and as such we investigated the cycling stability of CC/C-MWCNT-PI-800 at a scan rate of  $50 \text{ mV s}^{-1}$  in a three electrode system. As shown in **Figure 3.9d**, the electrode exhibits excellent cycle stability with 103% capacitance retention after 10000 cycles, which implies that it is electrochemically stable for long-term operation conditions. To further understand the capacitive behavior of

these samples, electrochemical impedance spectroscopy (EIS) analysis was conducted in the frequency range from 0.01 Hz to 1 MHz (**Figure 3.10a**). The x-intercept in the high frequency region implies internal resistance ( $R_s$ ). The semicircle in the high frequency region reflects the electrochemical reaction impedance of the electrode, and the small diameter of this semicircle indicates low charge-transfer resistance ( $R_{ct}$ ). The slope verticality in the low frequency region denotes efficient diffusion of the electrolyte to the electrode surface [73]. The Nyquist plot of CC and CC/MWCNT-PI-300 show no  $R_{ct}$  values, and is perpendicular to the real axis in the low frequency region. This indicates that CC and CC/MWCNT-PI-300 do not have any faradic reactions. In the case of CC/C-MWCNT-PI-600,  $R_{ct}$  is very large and the slope in the low frequency region highly inclines due to the poor accessibility of the electrolyte ions to the electrodes, indicating the bad rate capability. It might be a poor conductivity of carbon film due to the low carbonization temperature. After increasing the temperature,  $R_{ct}$  of CC/C-MWCNT-PI-800 and CC/C-MWCNT-PI-1000 were smaller than that of CC/C-MWCNT-PI-600. The curves of CC/C-MWCNT-PI-800 and CC/C-MWCNT-PI-1000 in the low frequency region are also nearly perpendicular to the real axis. The low  $R_{ct}$  and  $R_s$  values are

beneficial for excellent electrochemical behaviors due to good conductivity and fast charge transfer, which could accelerate fast redox reactions. The  $R_{ct}$  value of CC/C-MWCNT-PI-800 is relatively small compared to that of CC/C-PI-800, demonstrating a low charge transfer resistance attributed to the electrical conductivity of MWCNT in the PI matrix. As shown in **Figure 3.10b**, the electrodes exhibit remarkably high stability, with 103.7% of its initial capacitance present after 10000 cycles. This extraordinary cycling performance proves that the carbonized MWCNT-PI on the CC surface is electrochemically stable for long-term operation. A comparison of the N contents, electrolyte, specific capacitance and rate capability of this work with other references [38, 39, 44, 46, 74-76] is presented in **Table 3.2**.

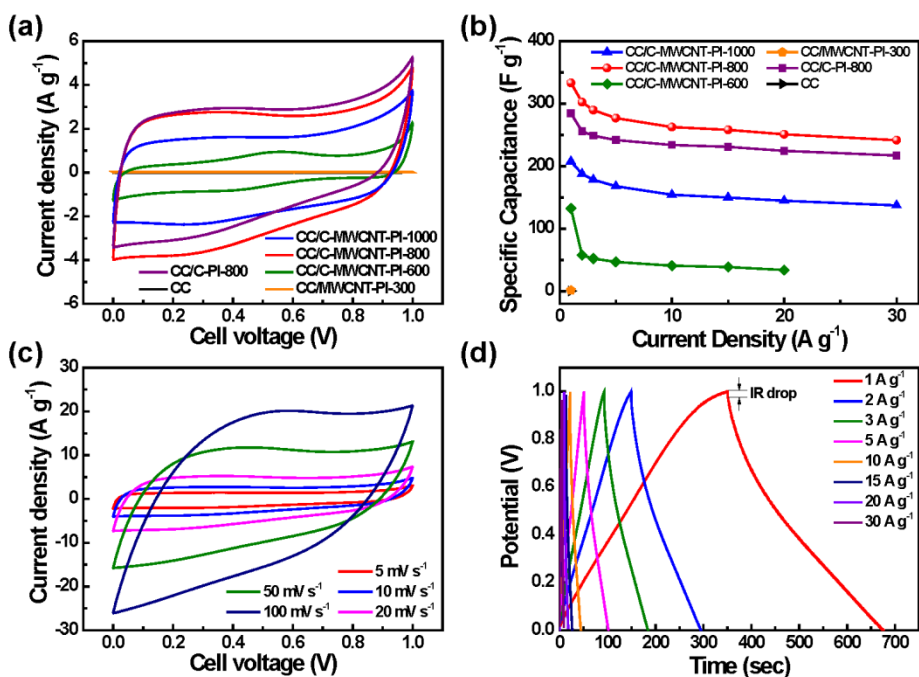


**Figure 3.9.** Electrochemical performances in a three electrode system by using 1 M H<sub>2</sub>SO<sub>4</sub> electrolyte within a potential range of 0–1.0 V. (a) CV curves of all samples at a scan rate of 10 mV s<sup>-1</sup>. (b) Specific capacitance of all samples at different current densities. (c) CV curves of CC/C-MWCNT-PI-800 at scan rates of 5, 10, 20, 50, 100 mV s<sup>-1</sup>. (d) Charge-discharge curves of CC/C-MWCNT-PI-800 at various current densities.

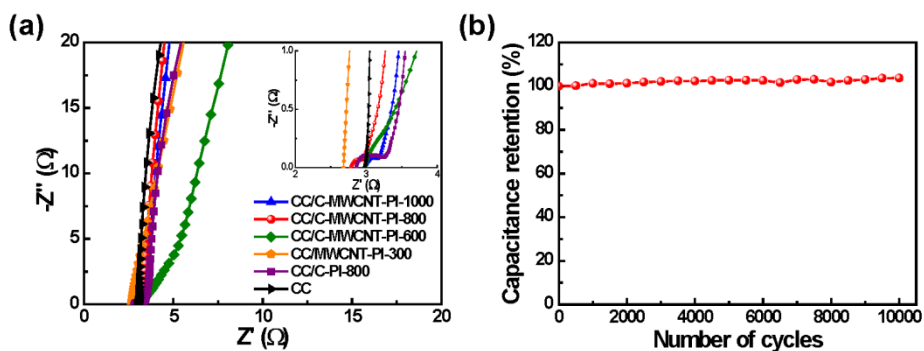


**Figure 3.10.** Electrochemical performances in a three electrode system by using 1 M  $\text{H}_2\text{SO}_4$  electrolyte within a potential range of 0–1.0 V. (a) Nyquist plots of all samples over a frequency range of 0.01 Hz – 1 MHz. (b) Cycle testing at a scan rate of  $50 \text{ mV s}^{-1}$  of CC/C-MWCNT-PI-800.

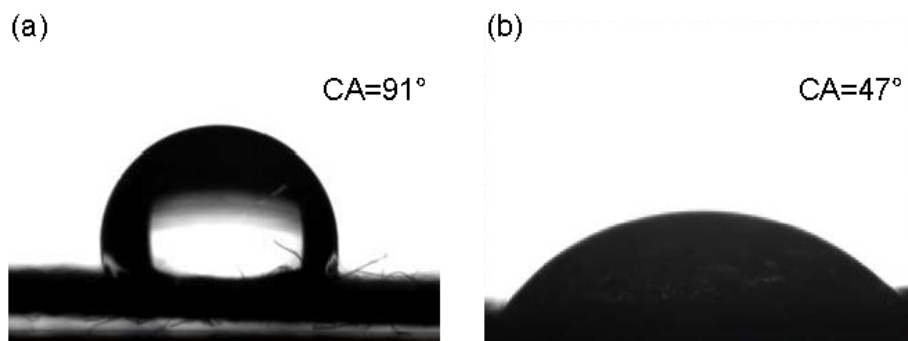


**Figure 3.11.** Contact angle measurement of (a) bare CC and (b) CC/C-MWCNT-PI-800.

**Table 3.2** Comparison of the nitrogen doped carbon-based materials in the three-electrode systems.

Materials	N contents	Electrolyte	Specific capacitance ( $F g^{-1}$ )	Rate capability ( $F g^{-1}$ )	ref
NCNF (CNF@PPy)	7.22 at%	6M KOH	202 at $1 A g^{-1}$	164.5 at $30 A g^{-1}$	38
NCNF (PAN@PANI)	8.96 at%	1M $H_2SO_4$	335 at $0.5 A g^{-1}$	175 at $32 A g^{-1}$	39
NCC	9.6 at%	1M $H_2SO_4$	207 at $1 A g^{-1}$	177 at $14 A g^{-1}$	44
NCNT	6.71 wt%	0.5M $Na_2SO_4$	105.4 at $2 mV s^{-1}$	70.5 at $200 mV s^{-1}$	46
NCNT	2.5 wt%	1M $H_2SO_4$	56 at $2 mV s^{-1}$	-	74
C-PI membrane	5.8 wt%	1M NaOH	179 at $0.75 A g^{-1}$	143.3 at $7 A g^{-1}$	75
PCNF	3.7 at%	6M KOH	215 at $0.2 A g^{-1}$	113 at $100 A g^{-1}$	76
CC/C-MWCNT-PI-800	2.78 at%	1M $H_2SO_4$	333.4 at $1 A g^{-1}$	241.7 at $30 A g^{-1}$	this work
CC/C-PI-800	1.55 at%	1M $H_2SO_4$	284.6 at $1 A g^{-1}$	217.3 at $30 A g^{-1}$	this work

To investigate the actual device behavior of CC/C-MWCNT-PI-800, symmetric all-solid-state devices were fabricated using filter paper as a separator between two CC/C-MWCNT-PI-800 electrodes and PVA-H<sub>2</sub>SO<sub>4</sub> polymer gel as a solid electrolyte. Here, activated material-coated CCs were directly used as highly flexible current collectors due to their favorable electric conductivity and mechanical durability. The electrochemical performances of the as-made devices were measured based on the total volume of the devices. **Figure 3.12a** shows the CV curves at scan rates of 5–50 mV s<sup>-1</sup>. In general, the CV curves at scan rates of 5–20 mV s<sup>-1</sup> have quasi-rectangular forms, but resistance-dominant behavior emerges at a high scan rate of 100 mV s<sup>-1</sup>. The galvanostatic charge/discharge curves of the CC/C-MWCNT-PI-800 symmetric supercapacitor cell at different current densities (0.02–0.3 A·cm<sup>-3</sup>) are shown in **Figure 3.12b**. Although the profile of the charge/discharge curves has nearly linear triangular shape, compared with charging time, shorter discharging time is observed under different discharge current densities. Additionally, *IR* drops are increased as a function of current density. To further investigate the properties of the full cell, EIS was conducted on the CC/C-MWCNT-PI-800 cell (**Figure 3.13**). Notably, the R<sub>s</sub> value of the full cell in the high frequency region

is  $\sim 5.0$  ohm, which is higher than that of a three-electrode system. The result indicates that in the full cell, the resistance between the electrode and electrolyte is increased as a result of a solid-state supercapacitor cell assembly. The maximum volumetric capacitance of the device is  $3.88 \text{ F cm}^{-3}$  at a current density of  $0.02 \text{ A cm}^{-3}$ . Moreover, the device retained 76.8% of its initial capacitance when the current density increased from  $0.02 \text{ A cm}^{-3}$  to  $0.3 \text{ A cm}^{-3}$ , demonstrating moderate rate capability. Furthermore, the symmetric supercapacitor cell exhibits excellent cycling performance, with 85.3% retention at a scan rate of  $0.2 \text{ A cm}^{-3}$  after 10000 cycles (**Figure 3.12d**). To test the electrochemical stability of the as-fabricated devices for use in flexible and wearable applications, we measured the CV at a scan rate of  $10 \text{ mV s}^{-1}$  while subjecting a device to different mechanical deformations under continuously changing conditions such as flattening, folding, twisting, and rolling (**Figure 3.14a**). As shown in **Figure 3.14b**, the CV curves of the device were not affected by the various deformation conditions, demonstrating excellent mechanical durability and electrochemical stability. The flexible all-solid-state supercapacitor device based on CC/C-MWCNT-PI-800 shows the volumetric energy density of  $0.50 \text{ mWh cm}^{-3}$  at a current density of  $0.02 \text{ mA cm}^{-3}$  and can

hold at an energy density of  $0.09 \text{ mWh cm}^{-3}$  with a high volumetric power density of  $72 \text{ mW cm}^{-3}$  at a current density of  $0.3 \text{ mA cm}^{-3}$ .

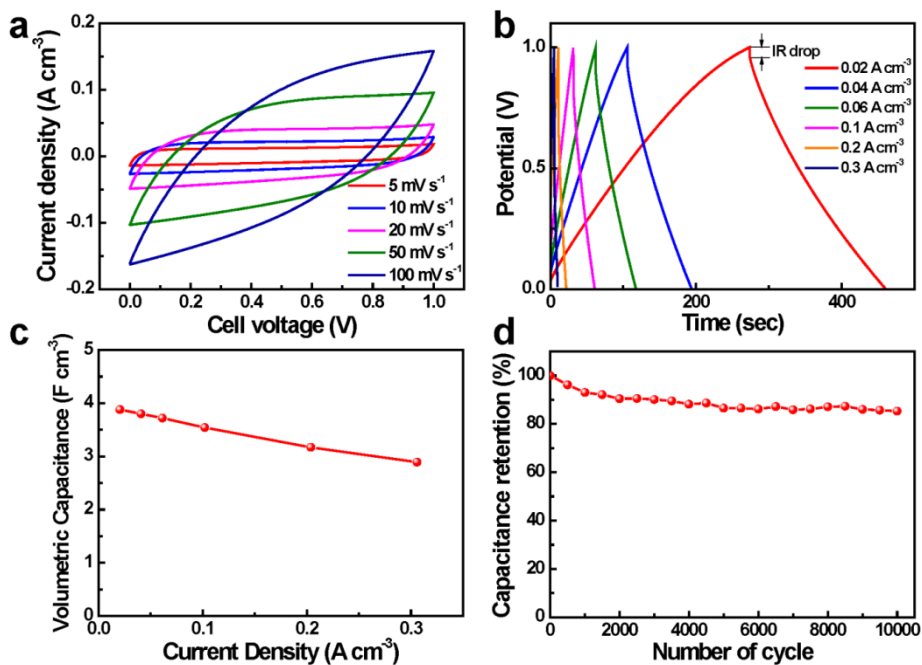


**Figure 3.12.** Electrochemical performances of flexible all-solid-state CC/C-MWCNT-PI-800 symmetric supercapacitor integrated with PVA-H<sub>2</sub>SO<sub>4</sub> polymer gel electrolyte. (a) CV curves at scan rates of 5, 10, 20, 50, 100 mV s<sup>-1</sup>. (b) Charge-discharge curves at various current densities. (c) Volumetric capacitance at various current densities. (d) Cycle testing at a current density of 0.2 A cm<sup>-3</sup> over 10,000 cycles.

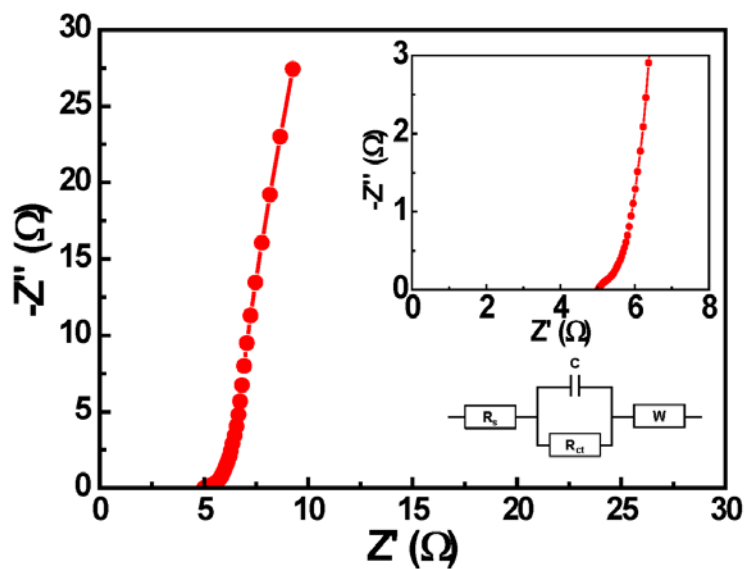


**Figure 3.13.** Nyquist plot of flexible all-solid-state CC/C-MWCNT-PI-800 symmetric supercapacitor cell integrated with PVA-H<sub>2</sub>SO<sub>4</sub> polymer gel electrolyte.

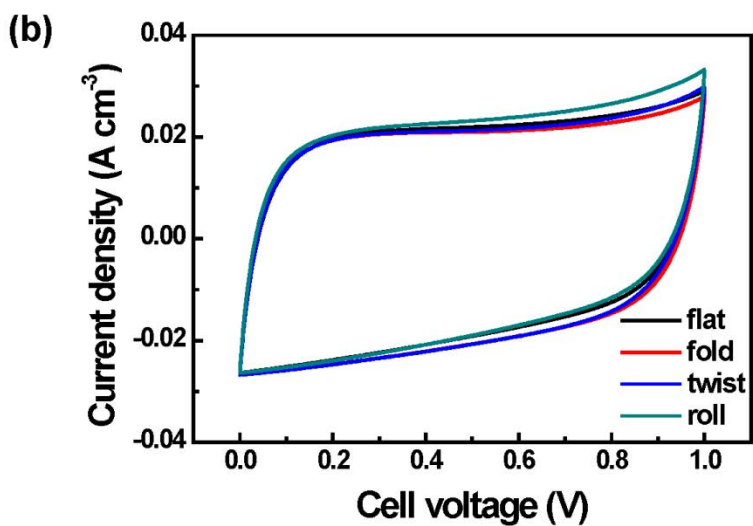
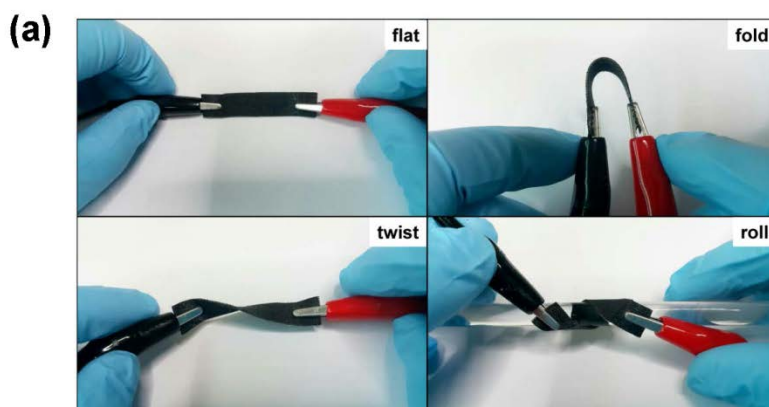


**Figure 3.14.** Flexibility tests of all-solid-state supercapacitors under flattening, folding, twisting, and rolling. (a) Digital images and (b) CV curves at a scan rate  $10 \text{ mV s}^{-1}$ .

## **3.2. Multiple-heteroatom-doped carbon derived from polyimide precursors**

### **3.2.1 Physical and chemical analysis**

**Figure 3.15** shows a schematic illustration of the fabrication of multiple-heteroatom-doped carbon electrodes. N, N,S and N,F-co-doped carbon precursors were synthesized by heteroatom-functionalized diamine and dianhydride monomers. Additional boron-doped carbon precursors were introduced by a controlled amount of boric acid into N,S and N,F-co-doped carbon precursors. Each prepared multiple-heteroatom-doped carbon precursor solution was dropped and coated onto a CC surface. After evaporating the solvent, multiple-heteroatom-doped carbon coated CC electrodes were obtained by following a thermal process at 800 °C for 1 h. The resulting samples with N, N,S, N,F, N,S,B, and N,F,B heteroatom-doped carbonized polyimide were designated as NCP, NSCP, NFCP, NSBCP, and NFBCP, respectively.

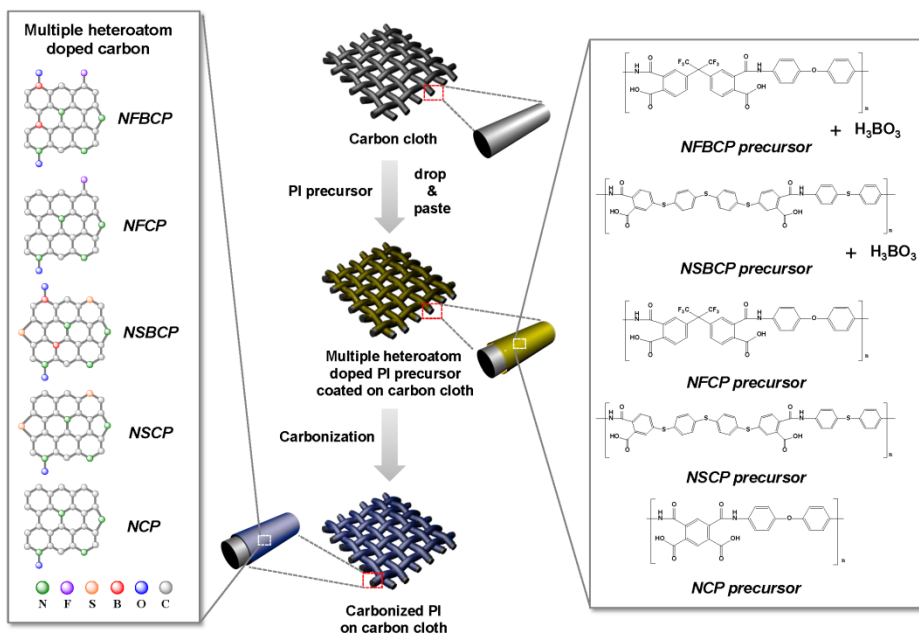


**Figure 3.15.** Schematic illustration of preparation of the multiple-heteroatom-doped carbon electrodes.

SEM images are shown in **Figure 3.16a and b**. The multiple-heteroatom-doped carbon was fully covered and uniformly coated the CC surface to an approximate thickness of 1  $\mu\text{m}$ . This result implies that the multiple-heteroatom-doped carbon coated CC can be used as supercapacitor electrodes without any binder or additives, which decrease the electrochemical performance behaviors.

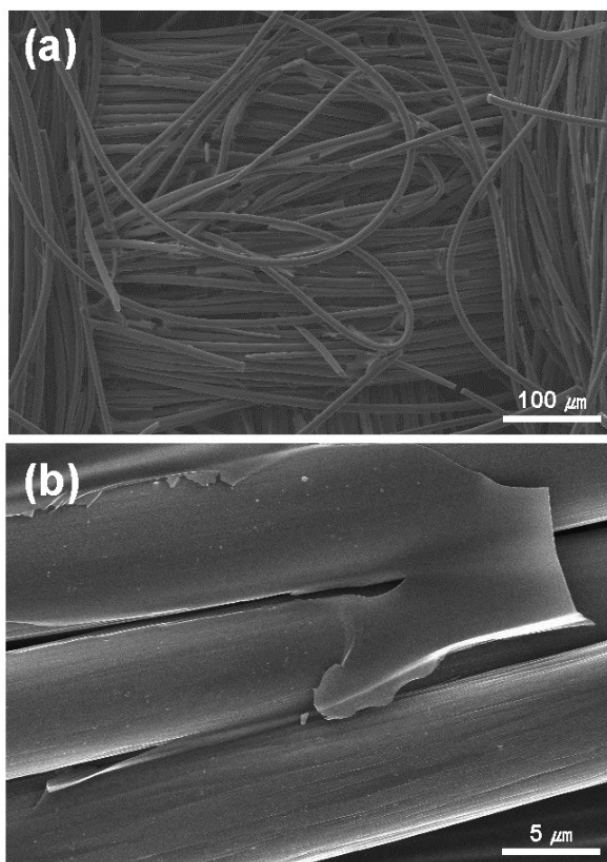


**Figure 3.16.** (a) Low- and (b) high-magnification SEM images of NFBCP electrode.

The thermal stability of the multiple-heteroatom-doped carbons was evaluated by TGA, as shown in **Figure 3.17**. NCP, NSCP, and NFCP precursors were coated on the CC and dried. Each of the prepared samples was heated to 800 °C under N<sub>2</sub>. As a reference sample, bare CC, showed a high thermal stability with 97% yield at 800 °C, which is suitable for use as a current collector at high temperature. The TGA peaks exhibited two main regions at 100–230 °C and 450–600 °C, which correspond to the imidization and carbonization steps, respectively [43, 77]. Therefore, an experimental temperature at 800 °C is sufficient for the carbonization of all precursors. The yields of NCP, NSCP, and NFCP at 800 °C were 65, 67, and 62%, respectively. Considering the weight loss of CC, the carbon yields of NCP, NSCP, and NFCP were higher than 50%, suggesting that polyimide derivatives are promising candidates for supercapacitor carbon electrodes.

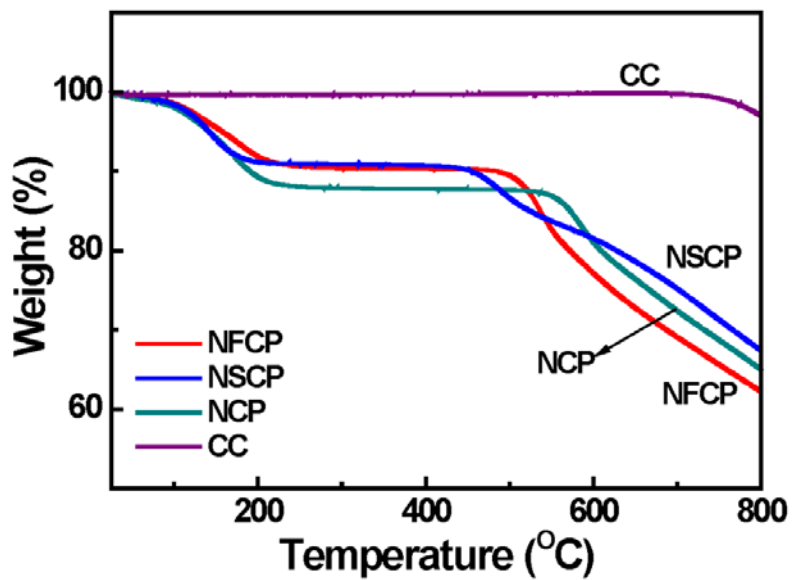


Figure 3.17. TGA analysis of multiple heteroatom doped carbons.

Raman spectroscopy is a useful method to study the doped carbon structure. The Raman spectra of multiple-heteroatom-doped carbons shown in **Figure 3.18** and **Table 3.3** exhibit three prominent peaks at  $\sim 1350\text{ cm}^{-1}$ ,  $\sim 1580\text{ cm}^{-1}$ , and  $\sim 2690\text{ cm}^{-1}$ , which are assigned to the D, G, and 2D bands, respectively. The D band corresponds to the disordered carbon structure with various defects, and the G band corresponds to the  $\text{sp}^2$ -bonded carbon atoms in a two-dimensional hexagonal lattice [78]. The average size of the  $\text{sp}^2$  domains ( $L_a$ ) were calculated by the Tuinstra–Koenig relation [79]:

$$L_a = (2.4 \times 10^{-10})\lambda^4(I_D/I_G)^{-1}$$

where  $\lambda$  is the excitation wavelength, which is 532 nm. The  $I_D/I_G$  ratios of CC, NCP, NSCP, NSBCP, NFCP, and NFBCP were 0.742, 0.952, 0.969, 1.032, 0.961, and 0.945, respectively (**Table 3.3**). This result indicates that the increasing  $I_D/I_G$  ratios of dual- and triple-doped carbons are revealed, producing more structured defects compared with single-heteroatom-doped NCP. The corresponding  $L_a$  values of CC, NCP, NSCP, NSBCP, NFCP, and NFBCP were 25.9, 20.2, 19.8, 18.6, 20.0, and 20.3, respectively, which suggest similar graphitization levels of heteroatom-doped carbons. Moreover, the intensity of the 2D band can be used to identify the number of layers or qualities in graphene-

related materials. The lowest and most broad 2D band indicates  $sp^3$ -amorphous or disordered or doped carbon structure [80, 81]. The  $I_{2D}/I_G$  ratios of 0.340 and 0.113 correspond to the NSBCP and NFBCP, respectively, which were lower than those of 0.372 and 0.282 for NSCP and NFCP, respectively. This result indicates that the boron atoms were successfully incorporated into the N,S and N,F co-doped carbons, as well as disturbing the stacking order of carbon layers.

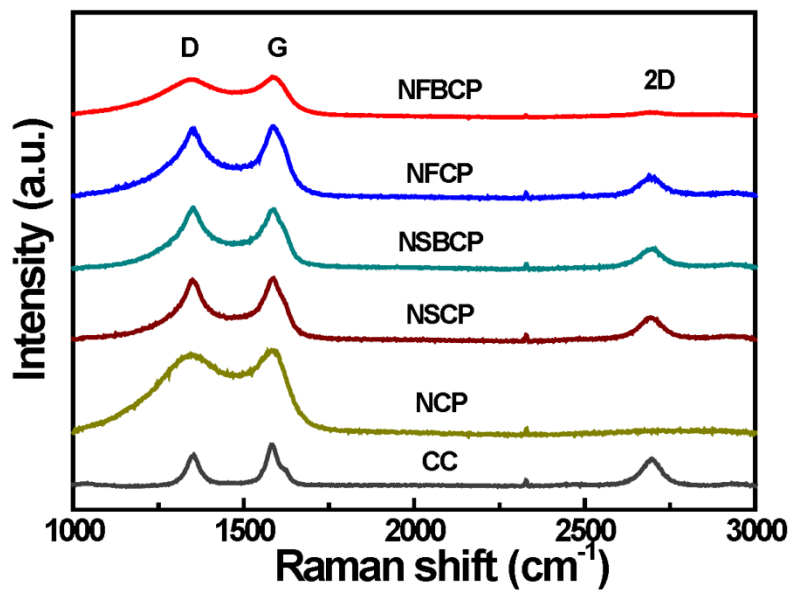


Figure 3.18. Raman spectra of multiple-heteroatom-doped carbons.

**Table 3.3.** Raman spectra data of multiple-heteroatom-doped carbons.

Sample	D peak ( $\text{cm}^{-1}$ )	G peak ( $\text{cm}^{-1}$ )	2D peak ( $\text{cm}^{-1}$ )	$I_D/I_G$	$I_{2D}/I_G$	$L_a$ (nm)
NFBCP	1350	1583	2690	0.945	0.113	20.3
NFCP	1348	1587	2692	0.961	0.282	20.0
NSBCP	1351	1587	2699	1.032	0.340	18.6
NSCP	1350	1587	2692	0.969	0.372	19.8
NCP	1346	1581	2699	0.952	0.044	20.2
CC	1353	1581	2698	0.742	0.645	25.9

To identify the composition of incorporated multiple heteroatoms into the carbon framework, XPS analysis was conducted, as shown in **Figure 3.19, 3.20, 3.21, 3.22, and 3.23**. All samples show three different deconvoluted peaks of the high-resolution N 1s at 398.5, 399.6, and 401.1 eV, corresponding to N-6 (pyridinic), N-5 (pyrrolic or pyridonic), and N-Q (quaternary), respectively [34]. N-6 and N-5 can improve the electrochemical performance by providing pseudocapacitance through faradic redox reactions. N-Q is located in the carbon matrix, bonding with three carbon atoms, which can effectively benefit the electron transfer and improve the conductivity. Interestingly, the peak intensity of N-Q in NFCP and NFBCP was higher than that of NSCP and NSBCP, which is advantageous for increasing the electrical conductivity of the electrode. According to the S 2p spectrum, the peaks at 164.3, 165.7, and 168.8 eV are attributed to S 2p<sub>3/2</sub>, S 2p<sub>1/2</sub>, and -SO<sub>n</sub>- bonds, respectively [82]. The high resolution of the F 1s spectrum shows very low intensity in the range 682–692 eV, corresponding to covalent C-F bonds [36]. The B 1s spectrum at 192.6 eV is attributed to B-O bonds [83]. As shown in **Table 3.4**, the amount of single-heteroatom dopant is 2.34 at.% of N for NCP. For dual-heteroatom-doped carbon, the N, S contents of NSCP are 1.32 and 0.82

at. %, and the N, F contents of NFPCP is 2.83 and 0.35 at. %. Even with relatively low amounts of S or F atoms in the carbon matrix, in situ multiple heteroatom doping can be easily tuned by controlling various diamine or dianhydride monomer compositions. Moreover, in triple-heteroatom-doped carbon obtained by introducing boric acid, the contents of N, S, and B in the NSBCP are 0.26, 1.42, and 0.68 at. %, respectively, and the contents of N, F, and B in the NFBCP are 4.0, 0.3, and 0.53 at. %. This result implies that additional boron atom doping from boric acid is successfully incorporated into the dual-heteroatom-doped carbons of NSCP and NFPCP.

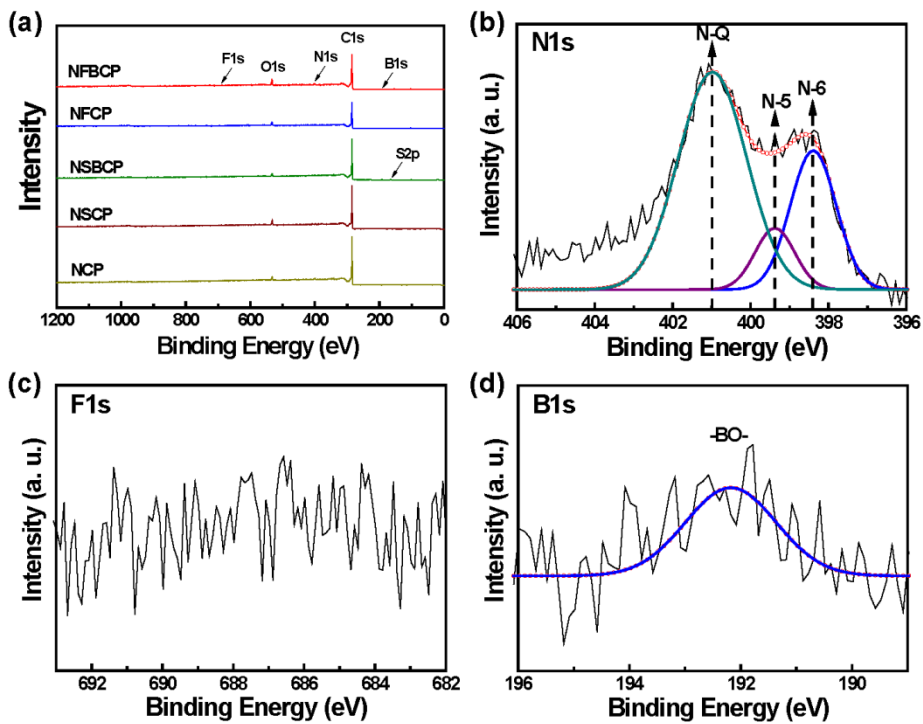


**Figure 3.19.** (a) The Low-resolution XPS spectra of multiple-heteroatom-doped carbons and high-resolution XPS spectra of (b) N 1s, (c) F 1s, (d) B 1s for NFBCP.

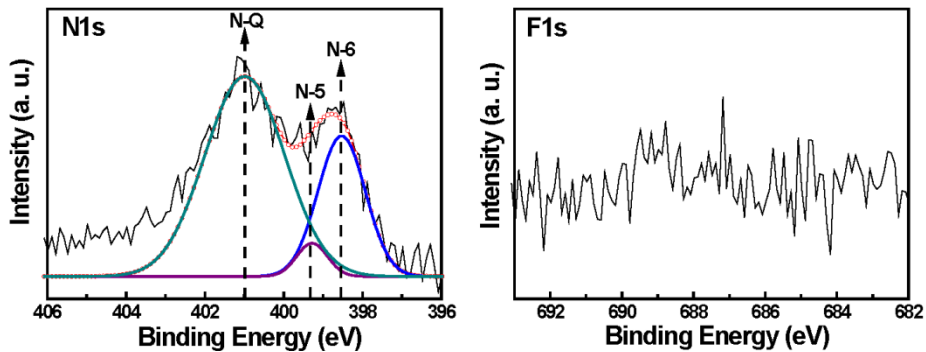


Figure 3.20. High-resolution XPS spectra of N 1s, and F 1s for NFCP.

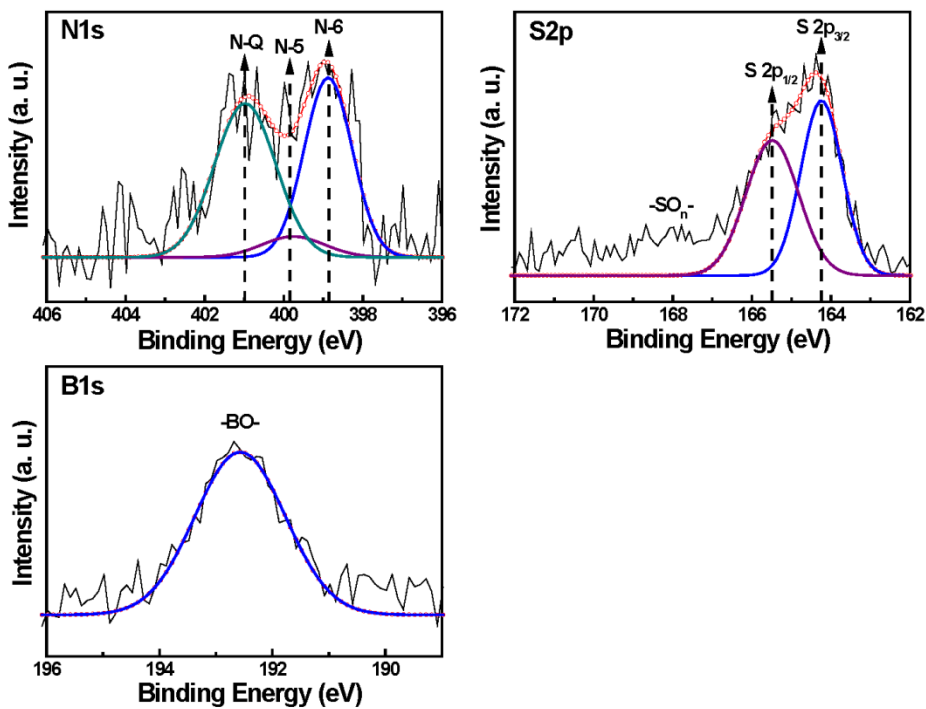
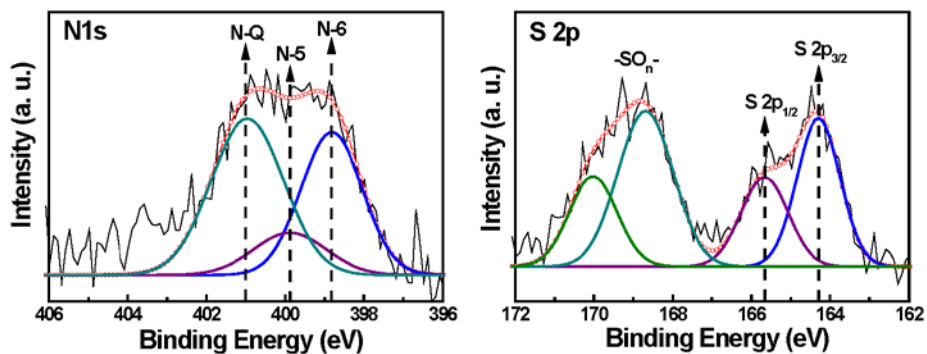
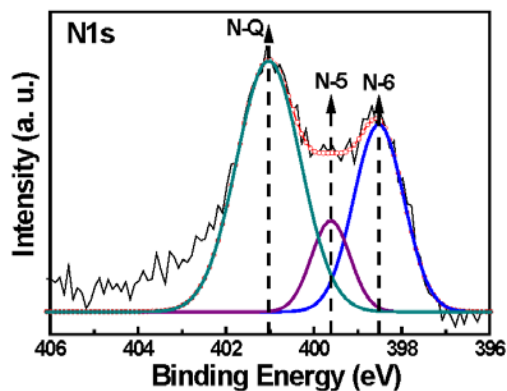


Figure 3.21. High-resolution XPS spectra of N 1s, S2p, and B1s for NSBCP.



**Figure 3.22.** High-resolution XPS spectra of N 1s, and S2p for NSCP.



**Figure 3.23.** High-resolution XPS spectra of N 1s for NCP.

**Table 3.4.** Heteroatom contents of multiple-heteroatom-doped carbons by XPS analysis

Sample	Atom %					
	C	O	N	F	S	B
NFBCP	88.67	6.50	4.00	0.30	-	0.53
NFCP	90.1	6.72	2.83	0.35	-	-
NSBCP	92.93	4.72	0.26	-	1.42	0.68
NSCP	91.51	6.34	1.32	-	0.82	-
NCP	93.18	4.48	2.34	-	-	-

**Figure 3.24** shows the comparative sheet resistance profiles of multiple-heteroatom-doped carbon electrodes using a four-point probe measurement method. The sheet resistance of carbon electrode with a single heteroatom species N decreased from  $0.813 \Omega \text{ sq}^{-1}$  for bare CC to  $0.58 \Omega \text{ sq}^{-1}$  for NCP. As the heteroatom number increased from single to double, the sheet resistances of N,S-co-doped carbon for NSCP and N,F-co-doped carbon for NFCP reached  $0.534$  and  $0.447 \Omega \text{ sq}^{-1}$ , respectively, which are lower than that of N-doped carbon for NCP. The intercalated S or F atoms in the carbon lattice improved the synergetic effects with N atoms, to which was attributed the enhanced energy density in the carbon. Moreover, the N-Q peak intensity of NFCP is higher than that of NSCP from the XPS analysis, which is favorable for enhancing the electrical conductivity. However, additional heteroatom boron doping into the dual-heteroatom-doped carbon increased the sheet resistance of the triple-heteroatom-doped carbon, to  $1.275 \Omega \text{ sq}^{-1}$  for NSBCP and  $0.783 \Omega \text{ sq}^{-1}$  for NFBCP, because low-level doped boron atoms in the carbon lattice are complexed with oxygen atoms, which act as electrochemical redox active sites [31].

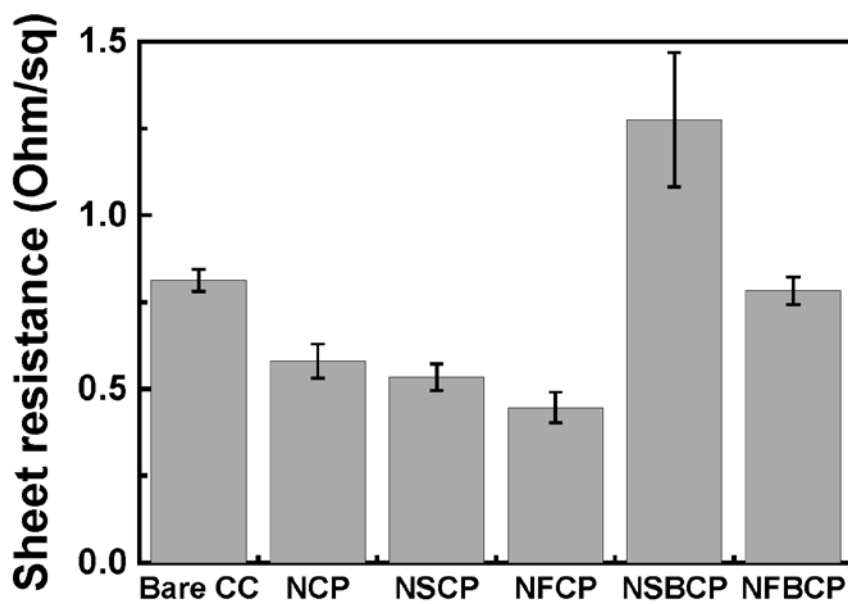


**Figure 3.24.** Sheet resistance measurement results of multiple-heteroatom-doped carbons.

The wettability of the carbon electrode was investigated by contact angle measurements to confirm the heteroatom doping effects, as shown in **Figure 3.25**. The contact angle of N-doped NCP decreased from  $129^\circ$  to  $55^\circ$ , compared to bare CC, due to the electronegativity of N atoms [16]. After additional fluorine doping into the N-doped carbon, the wettability of NFPCP was improved to a contact angle of  $42^\circ$ , which is an electronegativity enhancement effect due to the fluorine atoms [35]. However, the N,S-co-doped NSCP showed a contact angle of  $111^\circ$ , which is higher than that of NCP, owing to relatively lower N, S contents from XPS analysis because of their lower thermal stability at high temperature (**Figure 3.17**). The B-doped NSBCP with  $72^\circ$  and NFBCP with  $24^\circ$  exhibited higher wettability than those of NSCP and NFPCP, which is mainly due to oxygen complex formation with B atoms in the carbon lattice [31].

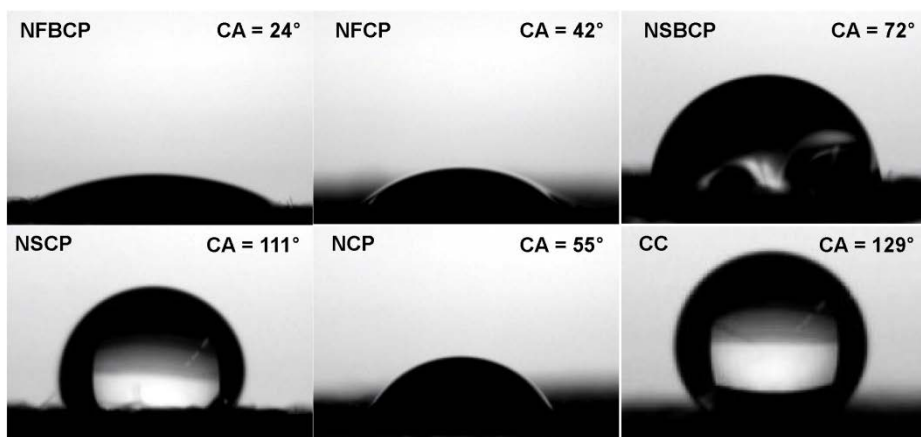


**Figure 3.25.** Contact angle measurement result of multiple-heteroatom-doped carbons.

### 3.2.2 Electrochemical activity measurements

The electrochemical performance of NCP, NSCP, NSBCP, NFCP, and NFBCP as a supercapacitor electrode material was examined by a typical three-electrode cell in 1 M H<sub>2</sub>SO<sub>4</sub> aqueous electrolyte, with Pt mesh and Ag/AgCl as the counter and reference electrodes, respectively. **Figure 3.26a** shows cyclic voltammetry (CV) curves at a scan rate of 10 mV s<sup>-1</sup> within a potential range of 0.0–1.0 V s<sup>-1</sup>. The CV curves exhibited quasi-rectangular shapes, including a pair of redox peaks at 0.3 and 0.5 V as well as hump peaks, which is the result of a combination of an electrical double layer capacitance behavior and faradic reactions, which are related to the surface functionalities from the doped heteroatoms [84, 85]. NFCP, NFBCP doped with N and F exhibited the highest CV curves compared with N- or N,S-doped carbons. NFBCP and NSBCP, which are additionally doped with boron, showed further increased electrochemical activity and pseudocapacitance contribution compared to that of NFCP and NSCP. Among these samples, the NFBCP doped with N,F,B-triple-heteroatom-doped carbon exhibited the best performance compared to that of NSBCP carbon. The relationships of specific capacitance with

the current density of NCP, NSCP, NSBCP, NFCP, and NFBCP are shown in **Figure 3.26b**. Through the current density increase from 1 A g<sup>-1</sup> to 20 A g<sup>-1</sup>, the specific capacitances of all samples decrease gradually. The specific capacitances of NCP, NSCP, and NFCP at 1 A g<sup>-1</sup> were 258.4, 246.5, and 311.5 F g<sup>-1</sup>, respectively. When the current density is increased to 20 A g<sup>-1</sup>, the specific capacitance of NCP, NSCP, and NFCP decrease to 205.6, 204, and 273.6 F g<sup>-1</sup>, respectively. The capacitance retentions are 79.6, 82.8, and 87.8%, respectively. This result implies that the effect of N,S or N,F co-doping is an enhancement in electron density of the carbon lattice with respect to that of N-doping, which contributes to an increase in the electrical conductivity. When boron atoms are doped into NSCP and NFCP, the specific capacitance value at 1 A g<sup>-1</sup> is increased to 281.6 and 350.3 F g<sup>-1</sup>, respectively. This specific capacitance value is higher than that of other multiple heteroatom doped carbon materials (**Table 3.5**) [26, 33, 35, 82, 84, 86-88]. However, the capacitance retentions of the NSCP and NFCP are decreased from 82.8 to 82.1% and from 87.8 to 83.2%, respectively. Because the doped boron atoms are combined with oxygen atoms on the carbon surface, the electrical conductivity of the electrode materials is reduced. This result coincides with the sheet resistance data in

**Figure 3.24.** The high specific capacitance of the NFBCP at high current density had several causes. First, the doped triple heteroatoms (N, F, and B) can induce pseudocapacitive behavior and improve the wettability between the electrolyte and electrodes. Second, the electrodes were fabricated without any binders or additives, resulting in large contact resistances and dead surface areas on the electrode materials. **Figure 3.26c** shows CV curves for NFBCP at different scan rates of 10–100 mV s<sup>-1</sup> in 1 M H<sub>2</sub>SO<sub>4</sub> aqueous electrolyte. The CV curves are slightly inclined with increasing current density, but retained quasi-rectangular shapes, indicating a high rate capability and good capacitive behavior. Galvanostatic charge–discharge measurements were performed to further investigate the electrochemical performance of NFBCP. The current density was increased from 1 A g<sup>-1</sup> to 20 A g<sup>-1</sup>, as shown in **Figure 3.26d**. The curves showed nearly symmetrical triangular shapes, indicating ideal capacitance behavior. To further study the electrochemical behavior, EIS measurements were conducted. **Figure 3.27a** shows a Nyquist plot of the NCP and NFBCP in 1 M H<sub>2</sub>SO<sub>4</sub> electrolyte with the frequency range from 0.01 Hz to 1 MHz. In the high-frequency region, the resistances consist of an equivalent series resistance (ESR) and charge transfer resistance (R<sub>ct</sub>). The ESR

represents the total resistance, which is composed of the ionic resistance of the electrolyte, the intrinsic resistance of the substrate, and the contact resistance at the interface between the active material and the current collector interface [39, 89]. The ESR value of NFBCP is 3.8  $\Omega$ , which is lower than that of NCP, at 4.3  $\Omega$ ; this could be attributed to the improvement in electrochemical activity due to the synergetic effects of multiple-heteroatom-doping. The semicircle in the high-frequency region ( $R_{ct}$ ) reflects the surface properties of the electrode and corresponds to the faradic reaction at the interface between the electrode and electrolyte [39, 89]. The diameter of the semicircle of NFBCP is relatively large compared to that of NCP, demonstrating a high charge transfer resistance attributed to the pseudocapacitive effects from N, F, and B doping. NFBCP shows a steeper slope than NCP to the real axis, because of more efficient diffusion of the electrolyte to the electrode surface, indicating a good rate capability. Thus, the capacitance retention of NFBCP at 20 A g<sup>-1</sup> is higher than that of NCP shown in **Figure 3.26b**. Long-term cycle stability is another requirement for essential supercapacitor applications. The cycle stability of NFBCP was tested at a scan rate of 10 A g<sup>-1</sup> in a three-electrode system, as shown in **Figure 3.27b**. After 10,000 cycles, 100%

of the initial capacitance was retained. This variation may be due to the effects from doped heteroatoms or *in situ* activation of the electrode to expose additional surface area. This result implies that NFBCP can be used an excellent electrode material for supercapacitor applications.

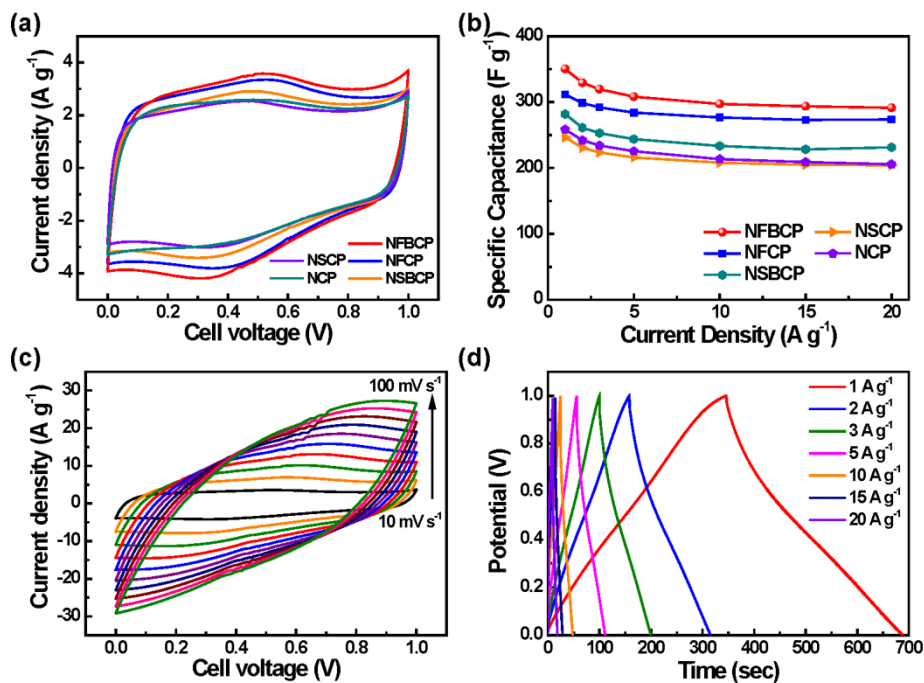


**Figure 3.26.** Electrochemical performances of multiple-heteroatom-doped carbons in a three-electrode system. (a) CV curves at scan rate of  $10 \text{ mV s}^{-1}$ . (b) Specific capacitance at different current densities from  $1 \text{ A g}^{-1}$  to  $20 \text{ A g}^{-1}$ . (c) CV curves of NFBCP at different scan rates from  $10 \text{ mV s}^{-1}$  to  $100 \text{ mV s}^{-1}$ . (d) GCD curves of NFBCP at different current densities from  $1 \text{ A g}^{-1}$  to  $20 \text{ A g}^{-1}$ .

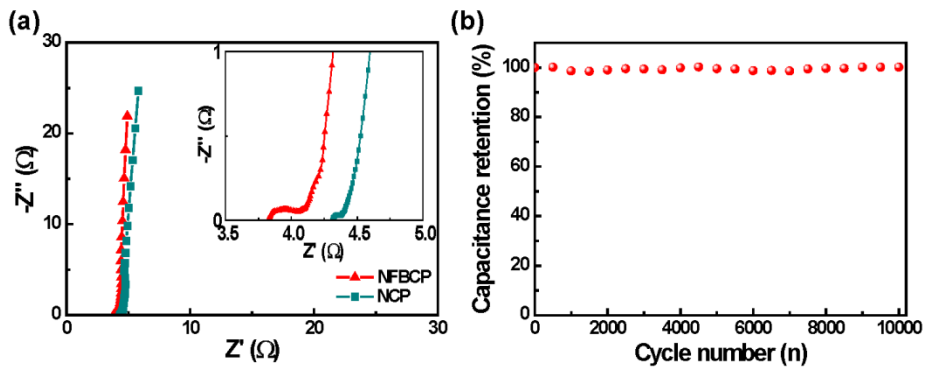


**Figure 3.27.** Electrochemical performances of multiple-heteroatom-doped carbons in a three-electrode system. (a) Comparison of Nyquist plots of NCP and NFBCP with frequencies from 0.01 Hz to 1 MHz. (b) Cycle stability test of NFBCP at current density of  $5 \text{ A g}^{-1}$ .

**Table 3.5.** Comparison of the multiple-heteroatom-doped carbon based materials in the three-electrode system.

Materials	Heteroatom contents (at.%)	Electrolyte	Specific capacitance ( $F g^{-1}$ )	ref
CM-NF	N 8.76 / F 3.4	1M $H_2SO_4$	270 at 0.2 $A g^{-1}$	26
NFMCNF	N 11.3 / F 10.9	1M $H_2SO_4$	252.6 at 0.5 $A g^{-1}$	33
FNC-4	F 17.5	1M TEA- $BF_4$	168 at 0.5 $A g^{-1}$	35
N,S-PCNs1-1	N 4.62 / S 2.56	6M KOH	285 at 1 $A g^{-1}$	82
HMC-800	N 4.38 / S 1.51	6M KOH	340 at 1.0 $A g^{-1}$	86
BN-GAs	N 3.0 / B 0.6	0.5M $Na_2SO_4$	239 at 1 $mV s^{-1}$	87
BN-HPC	N 12.1 / B 3.74	1M $H_2SO_4$	304 at 0.1 $A g^{-1}$	88
CC/C-MWCNT-PI-800	N 2.78	1M $H_2SO_4$	333.4 at 1 $A g^{-1}$	84
NFBCP	N 4.0 / F 0.3 / B 0.53	1M $H_2SO_4$	350.3 at 1 $A g^{-1}$	This work
NFCP	N 2.83 / F 0.35	1M $H_2SO_4$	311.5 at 1 $A g^{-1}$	This work
NSBCP	N 0.26 / S 1.42 B 0.68	1M $H_2SO_4$	281.6 at 1 $A g^{-1}$	This work
NSCP	N 1.32 / S 0.82	1M $H_2SO_4$	246.5 at 1 $A g^{-1}$	This work

To further the real-world application of NFBCP devices, flexible SSC devices were assembled. Two NFBCP electrodes were attached with a membrane as a separator and the PVA-H<sub>2</sub>SO<sub>4</sub> polymer gel electrolyte. **Figure 3.28a** shows CV curves of the device with scan rates increasing from 10 to 100 mV s<sup>-1</sup>. At low scan rates, the CV curves exhibited rectangular-like shapes. However, their shapes were inclined at high scan rates owing to the interfacial resistances that originated from the polymer gel electrolyte. The galvanostatic charge/discharge curves of the NFBCP supercapacitor device cell at different current densities from 0.01 to 0.2 A cm<sup>-3</sup> are shown in **Figure 3.28b**. Although the charge/discharge curves of the device exhibited a nearly linear triangular shape, shorter discharging time compared to than charging time is observed under different discharge current densities. Moreover, the *IR* drops of the GCD curves were observed and increased slightly with the current density. The maximum volumetric capacitance of the device is 4.45 F cm<sup>-3</sup> at a current density of 0.01 A cm<sup>-3</sup>, which was calculated from the GCD curve in **Figure 3.28c**. Moreover, the device retained 68% of its initial capacitance when the current density increased from 0.01 A cm<sup>-3</sup> to 0.2 A cm<sup>-3</sup>, demonstrating a moderate rate capability. To understand these results, EIS measurements of the

SSC device were conducted with the frequency range from 0.01 Hz to 1 MHz, as shown in **Figure 3.30**. The ESR value of the device in the high-frequency region was obtained as 3.5  $\Omega$ . However, the large semicircle diameter in the high-frequency region and highly inclined slope to the real axis indicate that the interfacial resistance between the electrode and polymer electrolyte increased owing to the SSC assembly. **Figure 3.28d** shows the long-term cycling performance of the SSC device at a scan rate of 0.05 A cm<sup>-3</sup>. After 10,000 cycles, 79 % of its initial capacitance was retained. However, increased variations were observed in the capacitance retention after the capacitance decreased. To investigate this large cycling variation, full cell device fabricated by non B-doped NFCP for a comparison was tested by cycling performances with same conditions at a scan rate of 0.05 A cm<sup>-3</sup>. As shown in **Figure 3.28d**, the cycling variation could not be observed in the NFCPs. It seems that B-doping is a major effects but it needs further studies to understand this phenomenon. For the practical applications in the field of flexible or wearable devices, the electrochemical stability test was performed under continuously changing conditions of mechanical deformation with flattening and folding in **Figure 3.29a**. The CV curves were measured at a scan rate of

50 mV s<sup>-1</sup> under changing conditions, and the device demonstrated excellent mechanical durability and electrochemical stability. Moreover, three SSC devices were assembled in series with 3V red LED to further investigate their practical applications, as shown in **Figure 3.29b**. The charged assembled cell powered a red light successfully. These results suggest the potential of such multiple-heteroatom-doped carbon-coated CC-based flexible SSCs for flexible and wearable electronics. The maximum volumetric energy density of 0.58 mWh cm<sup>-3</sup> at a current density of 0.01 mA cm<sup>-3</sup> and the maximum volumetric power density of 46 mW cm<sup>-3</sup> at a current density of 0.2 mA cm<sup>-3</sup> were achieved.

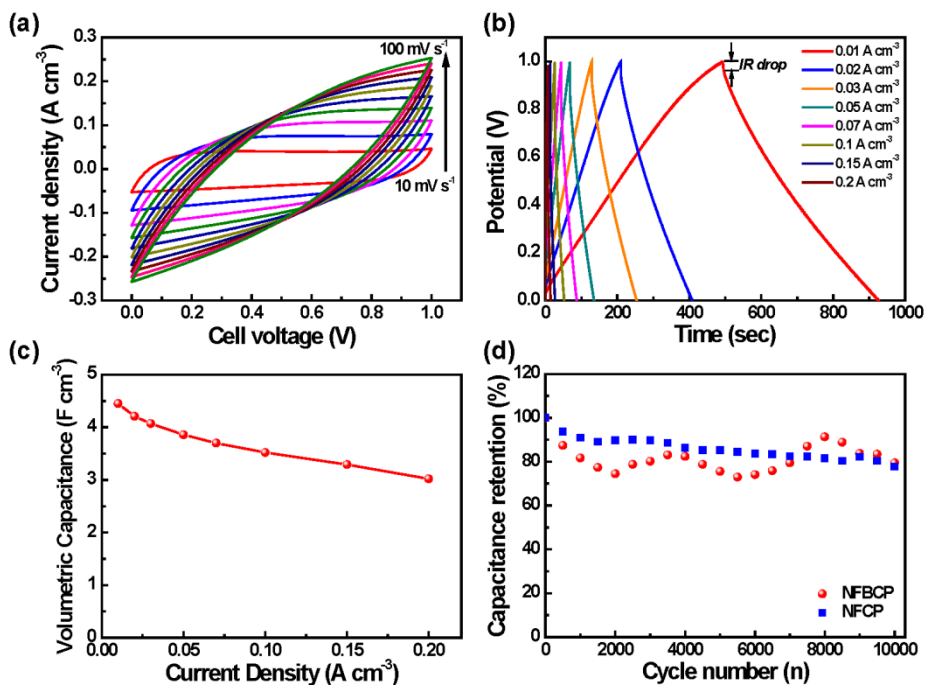


**Figure 3.28.** Electrochemical performances of the flexible all-solid-state supercapacitor device with NFBCP. (a) CV curves at scan rates from 10 to 100 mV s<sup>-1</sup>. (b) GCD curves at current density from 0.01 A cm<sup>-3</sup> to 0.2 A cm<sup>-3</sup>. (c) Volumetric capacitance at different current densities calculated from the GCD curves. (d) Long-term cycle stability test at current density of 0.05 A cm<sup>-3</sup>.

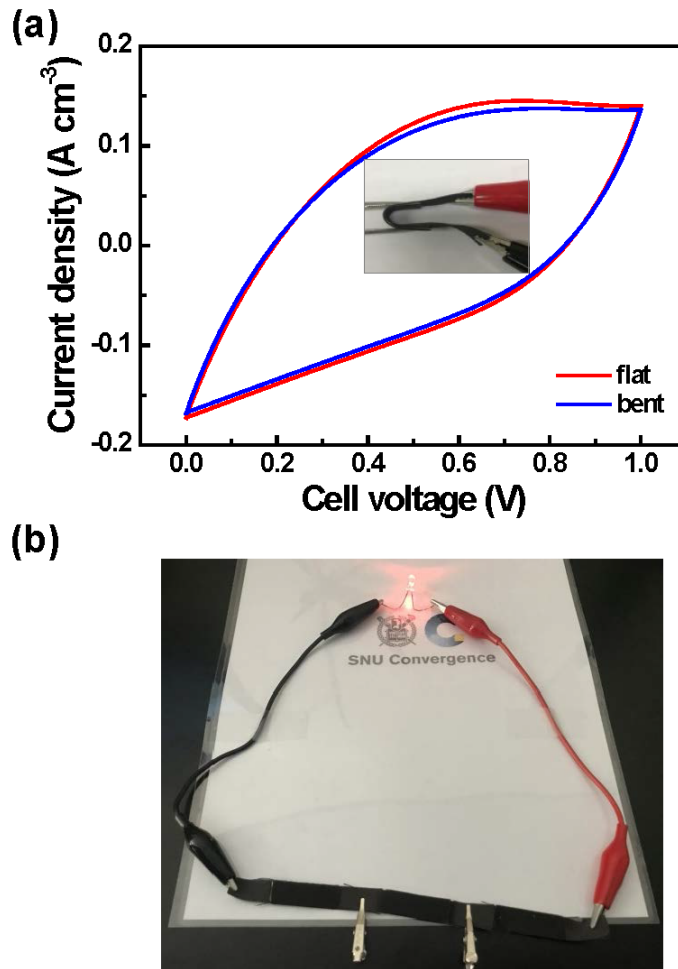


**Figure 3.29.** Electrochemical performances of the flexible all-solid-state supercapacitor device with NFBCP. (a) Flexibility test under bending and flattening at a scan rate of  $50 \text{ mV s}^{-1}$ . (b) Digital photo images of a LED lighted test with three devices connected in series.

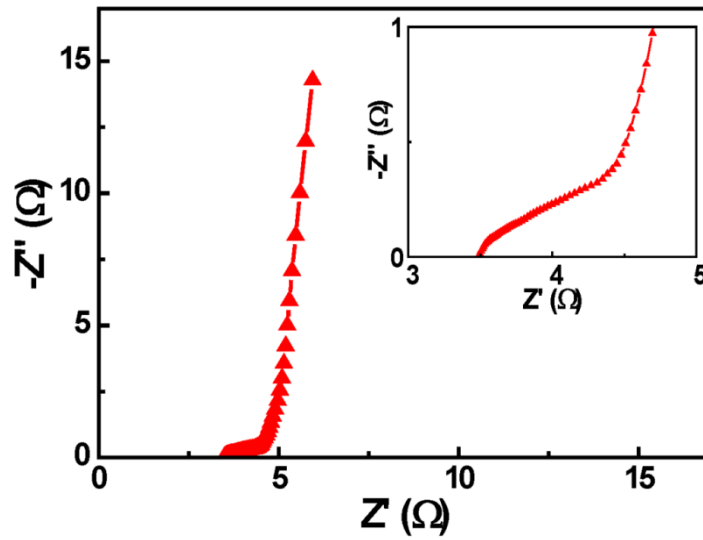


**Figure 3.30.** Nyquist plot of flexible all-solid-state NFBCP symmetric supercapacitor cell integrated with PVA-H<sub>2</sub>SO<sub>4</sub> polymer gel electrolyte.

### 3.3 Nitrogen- and boron-co-doped carbon derived from polyimide precursors

#### 3.3.1 Physical and chemical analysis

**Figure 3.31** shows a schematic illustration of the fabrication of N,B-co-doped carbon electrodes. Different contents of  $\text{NH}_3\text{BH}_3$  were mixed with PI precursors as a N-doping source. The introduced  $\text{NH}_3\text{BH}_3$  served as a co-doping source, as thermally decomposition released N and B atoms. Each mixed solution was dropped and coated onto a CC surface and then allowed to dry until the solvent evaporated. Finally, N, B-co-doped carbon-coated CC electrodes were obtained following a thermal process at 800 °C for 1 h. The resulting samples with 0, 3, 5, and 7 wt% of  $\text{NH}_3\text{BH}_3$ -loaded N,B-co-doped carbonized PI (NBCP) were denoted as NBCP-0, NBCP-3, NBCP-5, and NBCP-7, respectively. The morphologies of the as-prepared NBCP-coated CC electrodes were characterized by SEM (**Figure 3.32**). An NBCP layer with a thickness of  $\sim 1 \mu\text{m}$  was deposited over the CC surface without any deformations. This result indicates that the fabricated electrodes can be directly applied as binder-free type supercapacitor electrodes.

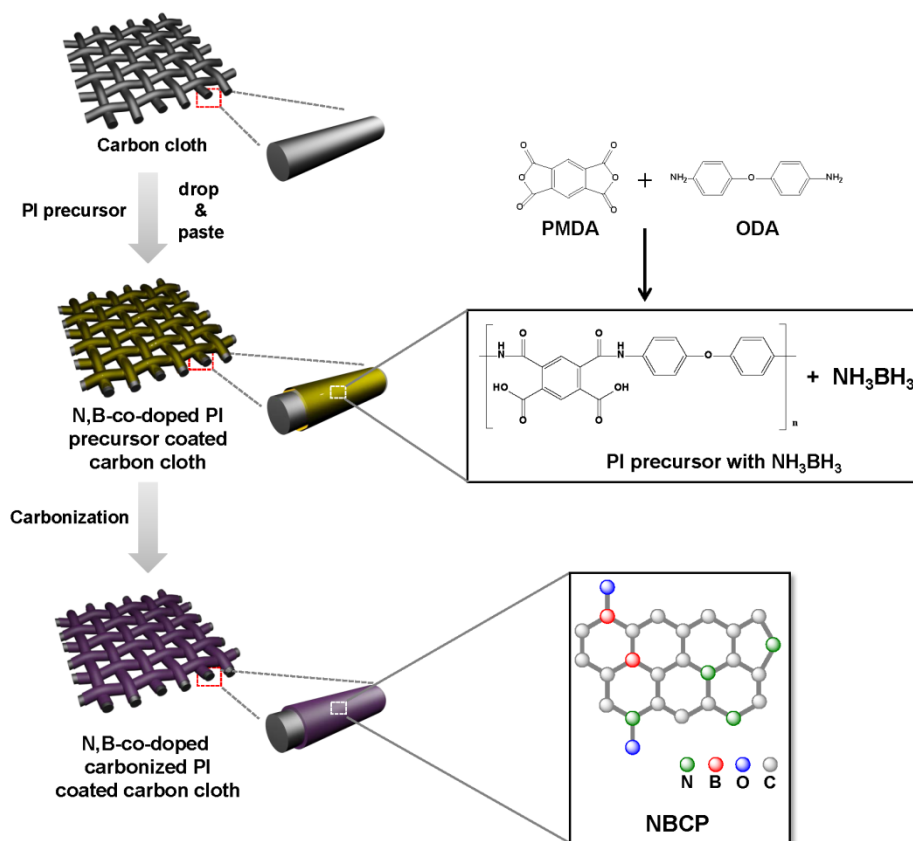


**Figure 3.31.** Schematic illustration of preparation of the nitrogen- and boron-co-doped carbon electrodes.

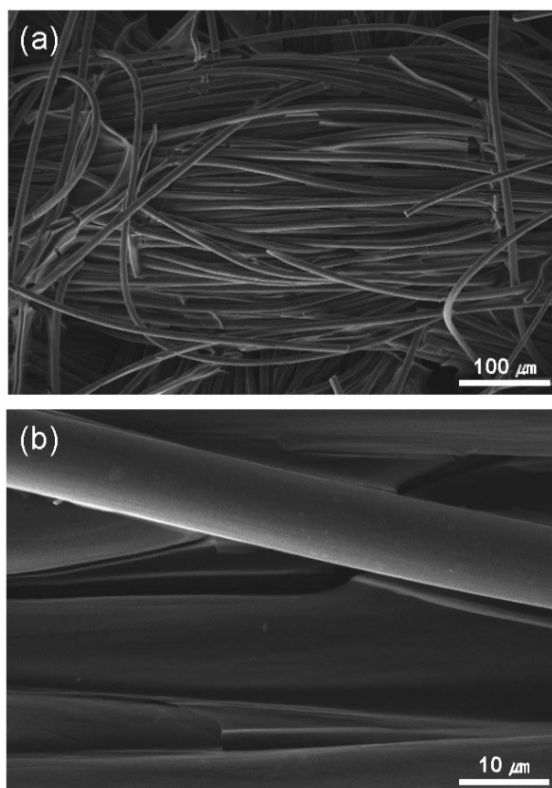


**Figure 3.32.** (a) Low- and (b) high-magnification SEM images of NBCP electrode.

The thermal stabilities of the NBCP samples were determined by TGA, as shown in **Figure 3.33**. As a reference sample, bare CC exhibited a very high thermal stability with 99% of its original weight maintained at 800 °C, indicating that CC is a suitable current collector for high-temperature processes. The TGA profiles of the NBCP samples exhibited two distinct phase-change regions. The first region at 100–300 °C corresponds to an imidization process and the second region at 500–700 °C corresponds to a carbonization process, indicating that the experimental temperature of 800 °C was sufficient to achieve carbonization [43]. The yield of NBCP-0 at 800 °C was 74.2%. Additionally, as the amount of  $\text{NH}_3\text{BH}_3$  increased from 3 to 7 wt%, the yield at 800 °C increased (76.7% for NBCP-3, 78.1% for NBCP-5, and 75.8% for NBCP-7). This result can be explained by an increasing amount of residual N and B after decomposition of  $\text{NH}_3\text{BH}_3$  at 800 °C.

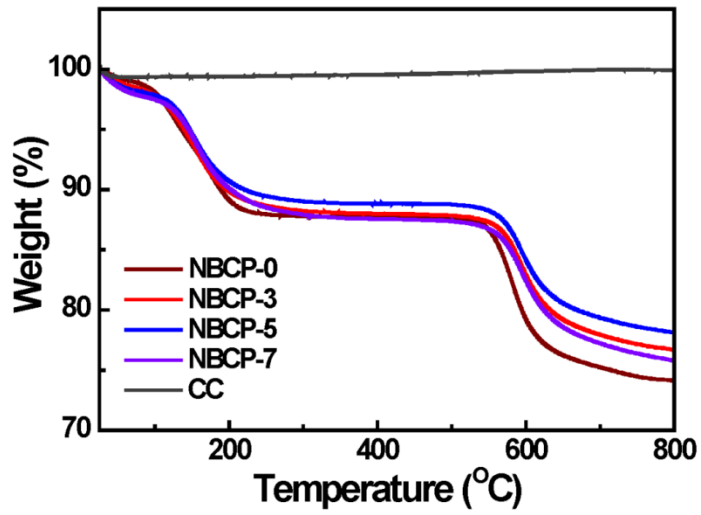


**Figure 3.33.** TGA analysis of CC and NBCPs.

The surface compositions of the NBCP samples were analyzed by XPS, as shown in Fig. 3. The chemical compositions of the NBCP samples are summarized in **Table 3.6**. As the amount of  $\text{NH}_3\text{BH}_3$  increased, the nitrogen and boron contents gradually increased from 3.92 to 4.93 at% and 0 to 1.31 at%, respectively. This finding indicates that the incorporation of  $\text{NH}_3\text{BH}_3$  is advantageous for simultaneous co-doping with N and B. **Figure 3.34a** shows that the NBCP samples are composed of C, N, O, and B. The C 1s spectrum of NBCP (**Figure 3.34b**) can be deconvoluted into peaks at 284.7 ( $\text{sp}^2$ ), 286.0 (C–N), 287.4 (C–O), 288.6 (C=O), 289.9 (O–C=O and O–C–B), and 291.2 eV ( $\pi$ – $\pi^*$ ). The N 1s spectrum of NBCP (**Figure 3.34c**) can be fitted with three peaks at 398.6, 399.6, and 400.9 eV, corresponding to N-6 (pyridinic), N-5 (pyrrolic or pyridonic), and N-Q (quaternary), respectively. The peaks in the B 1s spectrum of NBCP at 191.6 and 192.8 eV (**Figure 3.34d**) correspond to B–N and  $\text{B}_2\text{O}_3$  bonds, respectively [90, 91], indicating that both B and N atoms were incorporated during the carbonization process and that the incorporated B atoms were complexed with O atoms [31].

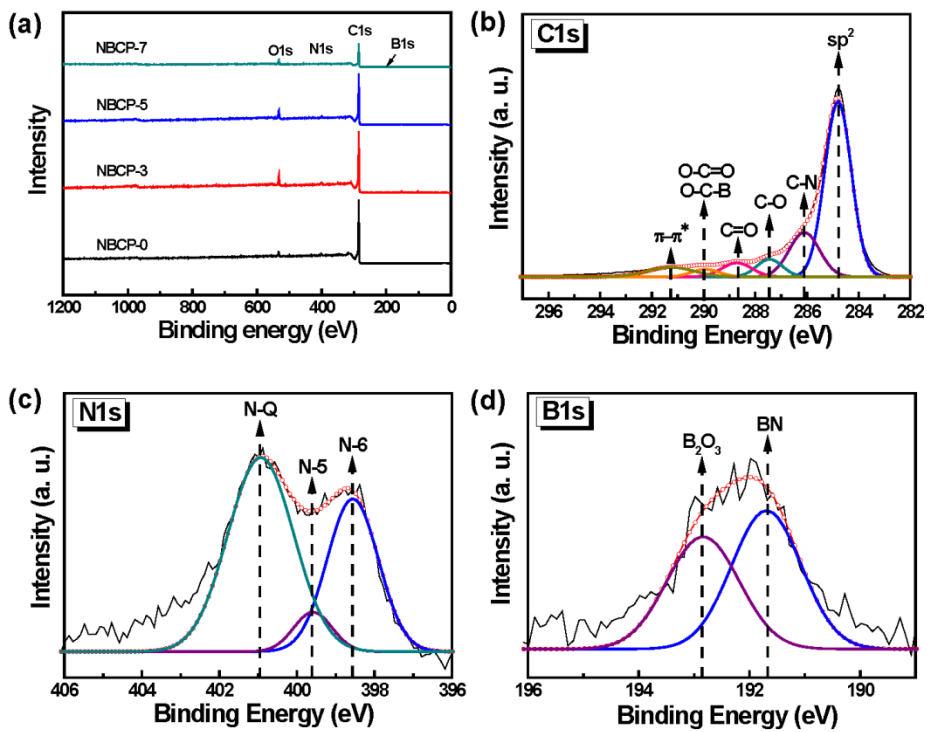


**Figure 3.34.** (a) Low-resolution XPS spectra of NBCPs and high-resolution (b) C 1s, (c) N 1s, and (d) B 1s XPS spectra.

**Table 3.6.** Elemental contents of NBCPs obtained by XPS analysis.

Sample	Atom %			
	C	O	N	B
NBCP-0	91.51	4.57	3.92	-
NBCP-3	87.19	7.64	4.58	0.59
NBCP-5	86.81	8.39	4.03	0.78
NBCP-7	84.12	9.64	4.93	1.31

Raman spectroscopy was conducted to investigate the introduction of N and B atoms into NBCP. The Raman spectra in **Figure 3.35a** exhibit three prominent broad peaks at  $\sim 1350$ ,  $\sim 1580$ , and  $\sim 2700$   $\text{cm}^{-1}$  corresponding to the D, G, and 2D peaks, respectively. The G peak corresponds to the  $E_{2g}$  mode of  $sp^2$  bonded carbon atoms in a graphitized structure, whereas the D peak usually indicates the presence of structural defects and disorder-induced phonon modes in a structure [78]. Further, the 2D peak represents the second order of the D peak [80, 81]. The  $I_D/I_G$  ratios of CC, NBCP-0, NBCP-3, NBCP-5, and NBCP-7 were 0.972, 0.977, 0.967, 1.005, and 0.984, respectively (**Figure 3.35b**). The  $I_D/I_G$  ratios are increased with slightly increasing N, B doping contents but it is not clear for indicating the boron doping in the carbon matrix. Therefore, to investigate boron doping, we calculated the  $I_{2D}/I_G$  ratios with increasing amounts of incorporated  $\text{NH}_3\text{BH}_3$  in the PI precursors (**Figure 3.35c**). The intensity of the 2D peak is dependent on doping owing to the influence of electron–electron interactions on the total scattering rate of photogenerated electrons (holes) [81, 92-94]. The  $I_{2D}/I_G$  ratios of CC, NBCP-0, NBCP-3, NBCP-5, and NBCP-7 were 0.625, 0.146, 0.093, 0.156 and 0.192, respectively. The  $I_{2D}/I_G$  ratio in NBCP-3 is the lowest value among the samples. This result suggests

that boron atoms were successfully incorporated into the carbon matrix of NBCP-3, which disturbed the stacking order of the carbon layers.

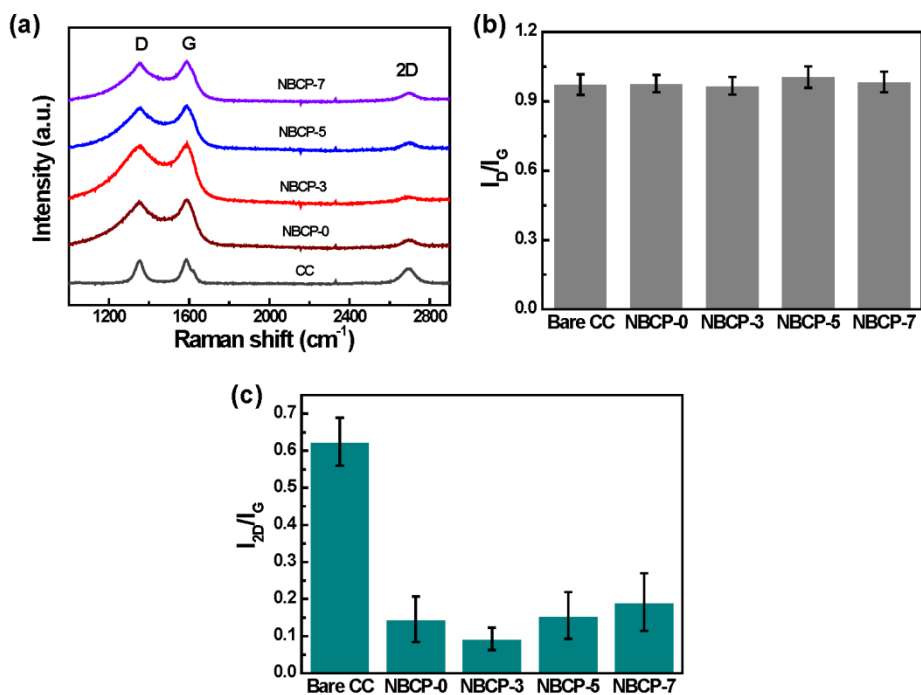


**Figure 3.35.** (a) Raman spectra of CC and NBCP samples. (b) Comparison of peak intensity ratios  $I_{2D}/I_G$  and  $I_D/I_G$  in the Raman spectra of NBCPs.

The sheet resistances of the NBCP samples were measured using a four-point probe method, as shown in **Figure 3.36**. As a reference, the sheet resistance of untreated bare CC was  $0.813 \Omega \text{ sq}^{-1}$ . The highest sheet resistance was exhibited by NBCP-3 ( $0.748 \Omega \text{ sq}^{-1}$ ) and the sheet resistance decreased with further increases in boron content to  $0.650 \Omega \text{ sq}^{-1}$  for NBCP-5 and  $0.602 \text{ Ohm sq}^{-1} \Omega$  NBCP-7. This result indicates that NBCP-3 had the highest amount of doped boron complexed with oxygen atoms, which increases the sheet resistance.

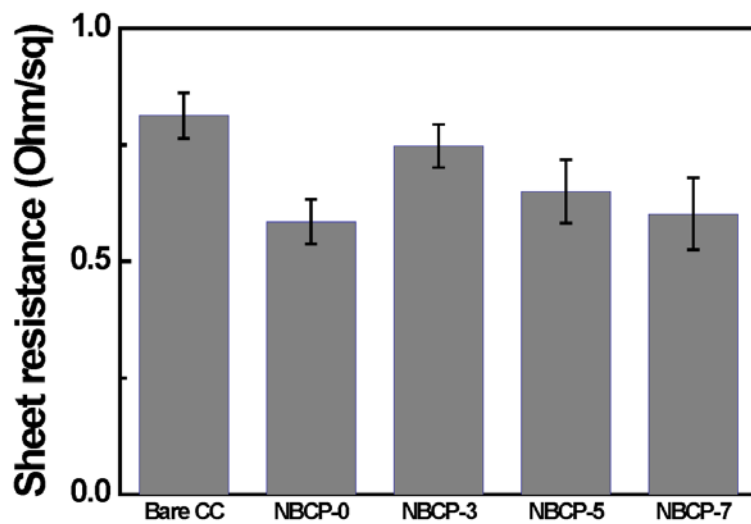


**Figure 3.36.** Sheet resistances of CC and NBCPs.

### 3.3.2 Electrochemical activity measurements

The N,B-co-doping effects in NBCP were confirmed by electrochemical measurements in a three-electrode cell with 1 M H<sub>2</sub>SO<sub>4</sub> as an aqueous electrolyte. **Figure 3.37a** shows the cyclic voltammetry (CV) curves of the NBCP samples at a scan rate of 10 mV s<sup>-1</sup> within the potential range of 0.0–1.0 V. The CV curve of NBCP-0 without boron doping exhibited a quasi-rectangular shape with a pair of redox peaks at ~0.4 V owing to the combination of electrical double layer capacitance behavior and faradic reactions. As the loading amount of NH<sub>3</sub>BH<sub>3</sub> increased, the pair of redox peaks shifted to 0.5 and 0.7 V, with the largest CV curve area observed for NBCP-3. The changes in the specific capacitances of the NBCP samples on increasing the current density from 1 to 20 A g<sup>-1</sup> are compared in **Figure 3.37b**. N, B-co-doped NBCP-3 shows the highest specific capacitance of 277.8 F g<sup>-1</sup> at a current density of 1 A g<sup>-1</sup>, whereas the specific capacitance of N-doped NBCP-0 is 245 F g<sup>-1</sup> at a current density of 1 A g<sup>-1</sup>, implying that co-doping may enhance the capacitance through synergetic effects. The specific capacitances of NBCP-5, and NBCP-7 C at 1 A g<sup>-1</sup> were 252.6, and 241.6 F g<sup>-1</sup>, respectively. At the highest current density of

20 A g<sup>-1</sup>, specific capacitances of 196.9 (80.4%), 237.3 (85.4%), 224.5 (88.9%), and 222.3 F g<sup>-1</sup> (92.0%) were retained for NBCP-0, NBCP-3, NBCP-5, and NBCP-7, respectively (**Figure 3.37c**). Interestingly, the capacitance retention gradually increased as the amount of NH<sub>3</sub>BH<sub>3</sub> loading increased. Though low-level B doping induced oxygen chemisorption on the carbon surface, which decreases the capacitance retention, increasing the N doping level may enhance the conductivity, causing a shift in the Fermi level toward the conduction band. **Figure 3.37d** shows the CV curves of NBCP-3 at various scan rates from 10 to 100 mV s<sup>-1</sup> in the potential window of 0.0–1.0 V. A pair of humps appeared in the CV curves at 0.4–0.5 V for all scan rates. This feature is characteristic of faradic redox reactions, which implies successful doping of N and B atoms into the carbon framework [95]. **Figure 3.38a** shows the galvanostatic charge–discharge (GCD) curves of NBCP-3 at various current densities from 1 to 20 A g<sup>-1</sup>. The curves have quasi-triangular shapes, even at relatively high current densities, indicating ideal capacitance behavior. EIS measurements were conducted to further study the electrochemical behavior of the NBCP samples. **Figure 3.38b** shows the Nyquist plots of NBCP-0 and NBCP-3 in 1 M H<sub>2</sub>SO<sub>4</sub> electrolyte within the frequency range of 0.01 Hz to 1 MHz. The

semicircle in the high-frequency region indicates the interfacial charge transfer resistance ( $R_{ct}$ ). The x-intercept in the high-frequency region indicates the internal resistance ( $R_s$ ), which is the total resistance corresponding to the contact resistance between the electrolyte and the electrode and the intrinsic resistance [39, 89]. A steeper slope to the real axis in the low-frequency region indicates efficient diffusion of the electrolyte to the electrode surface, suggesting good rate capability [33]. For NBCP-0 and NBCP-3, the  $R_s$  value and the slope to the real axis show similar behavior. However, the  $R_{ct}$  value for NBCP-3 is smaller than that for NBCP-0, which is attributed to the synergetic effects of dual heteroatom doping with N and B.

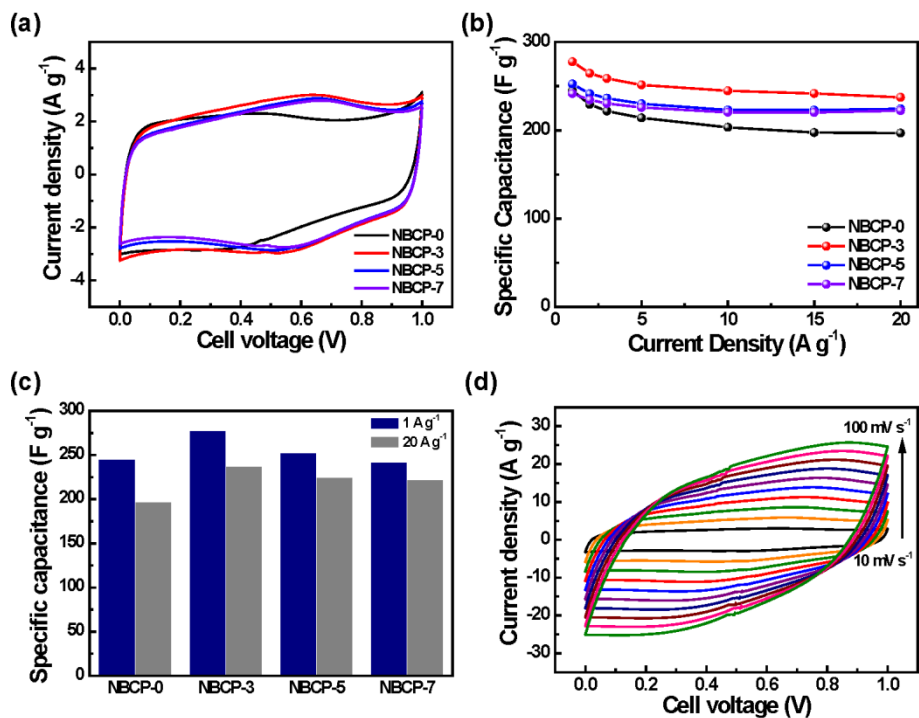


**Figure 3.37.** Electrochemical performance of NBCPs in a three-electrode system. (a) CV curves of NBCPs at a scan rate of  $10 \text{ mV s}^{-1}$ . (b) Specific capacitance of NBCPs at various current densities from 1 to  $20 \text{ A g}^{-1}$ . (c) Comparison of the specific capacitances of NBCPs at current densities of 1 and  $20 \text{ A g}^{-1}$ . (d) CV curves of NBCP-3 at various scan rates from 10 to  $100 \text{ mV s}^{-1}$ .

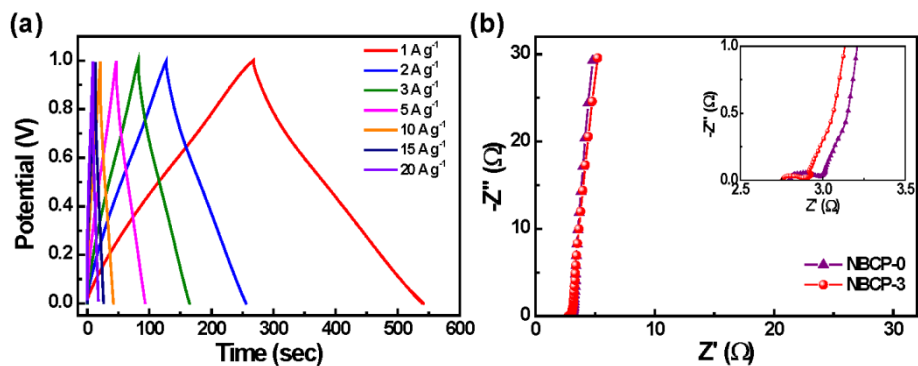


**Figure 3.38.** Electrochemical performance of NBCPs in a three-electrode system. (a) GCD curves of NBCP-3 at various current densities from 1 to 20  $\text{A g}^{-1}$ . (b) Nyquist plots of NBCP-0 and NBCP-3 in the frequency range of 0.01 Hz to 1 MHz.

To study the actual device performance of NBCP-3, flexible all-solid-state supercapacitor devices were fabricated. Two NBCP-3 electrodes were attached to a cellulose membrane as a separator with a PVA-H<sub>2</sub>SO<sub>4</sub> polymer gel electrolyte. **Figure 3.39a** shows the CV curves of the device at various scan rates from 10 to 100 mV s<sup>-1</sup>. The CV curves have similar rectangular-like shapes, indicating that the solid-state device exhibits ideal capacitive behavior. As shown in **Figure 3.39b**, the GCD curves of the NBCP-3 supercapacitor device at different current densities from 0.01 to 0.2 A cm<sup>-3</sup> exhibit nearly linear triangular shapes. However, the GCD curves also exhibit *IR* drops and discharge times that are shorter than the charge times. This behavior can be attributed to inefficient diffusion of ions owing to resistance between the electrode and the electrolyte in the solid-state supercapacitor cell. The Nyquist plot of the flexible all-solid-state NBCP device within the frequency range of 0.01 Hz to 1 MHz is shown in **Figure 3.41**. The R<sub>s</sub> value from the high-frequency region of the Nyquist plot is 3.28 Ω. The semicircle corresponding to R<sub>ct</sub> in the high-frequency region was larger than that observed for the three-electrode system, demonstrating incensement of the electrode–electrolyte interface in the solid-state supercapacitor device. The volumetric

capacitances of the device calculated from the GCD curves are shown in **Figure 3.39c**. The capacitance is  $2.97 \text{ F cm}^{-3}$  at a current density of  $0.01 \text{ A cm}^{-3}$  and 81% of the initial capacitance is retained at a current density of  $0.2 \text{ A cm}^{-3}$ , indicating a good rate capability. The long-term cycling performance of the device at a scan rate of  $0.05 \text{ A cm}^{-3}$ , as shown in **Figure 3.39d**, revealed that 92.4% of the initial capacitance was retained after 10000 cycles, with some increases in capacitance observed after the initial decrease. To test practical flexible and wearable applications, the electrochemical stability of the as-fabricated devices was examined by conducted CV at a scan rate of  $50 \text{ mV s}^{-1}$  under various mechanical deformation conditions, such as rolling and flattening, as shown in **Figure 3.40a**. The CV curves of the device reveal excellent mechanical durability and electrochemical stability under the deformation conditions. To further test practical applications, three device cells were connected in series. The potential window is extended from 1.0 V for a single device to 3.0 V for the series device. Upon charging to 3 V, a light-emitting diode (LED) was successfully switched on (**Figure 3.40b**). The power density and energy density are very important parameters that influence the practical applications of supercapacitor devices. The NBCP-3-based full cell device shows a

maximum energy density of  $0.38 \text{ mWh cm}^{-3}$  and a maximum power density of  $42 \text{ mWh cm}^{-3}$ .

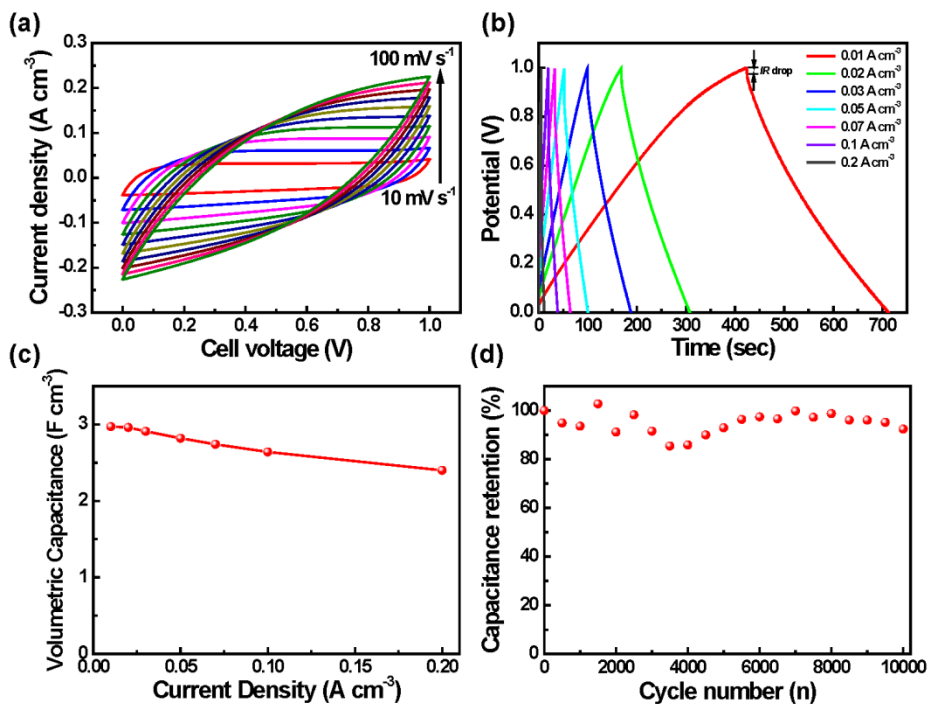


**Figure 3.39.** Electrochemical performance of the flexible all-solid-state supercapacitor device with NBCP-3. (a) CV curves at scan rates from 10 to  $100 \text{ mV s}^{-1}$ . (b) GCD curves at current densities from  $0.01$  to  $0.2 \text{ A cm}^{-2}$ . (c) Volumetric capacitances at various current densities calculated from the GCD curves. (d) Long-term cycle stability test at a current density of  $0.05 \text{ A cm}^{-2}$ .

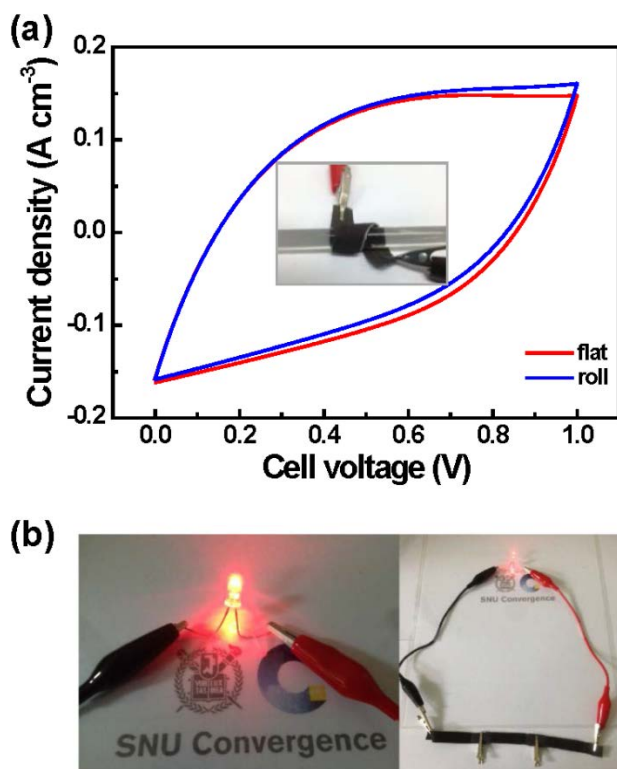


**Figure 3.40.** Electrochemical performance of the flexible all-solid-state supercapacitor device with NBCP-3. (a) Flexibility test under rolled and flattened conditions at a scan rate of  $50 \text{ mV s}^{-1}$ . (b) Digital photos of a LED test with three devices connected in series.

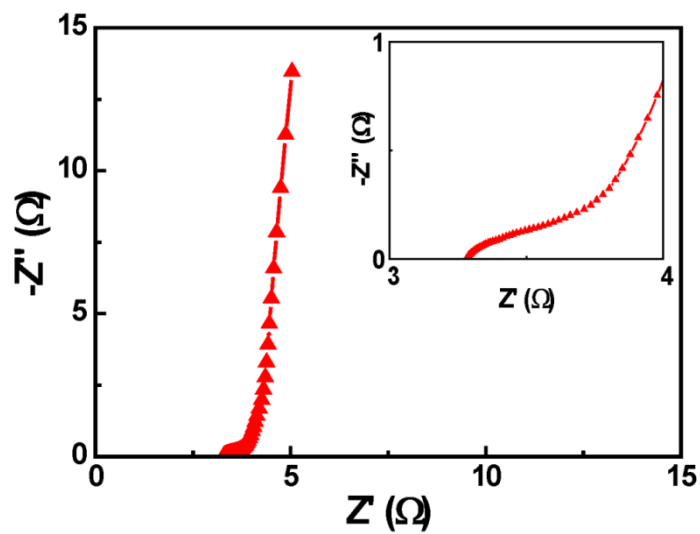


**Figure 3.41.** Nyquist plot of flexible all-solid-state NBCP-3 symmetric supercapacitor cell integrated with PVA-H<sub>2</sub>SO<sub>4</sub> polymer gel electrolyte.

## Chapter 4. Conclusions

In summary, this thesis is mainly focused on the synthesis of various types of heteroatom doped carbon materials derived from PI precursors by facile methods. Also, PI precursors were applied on flexible carbon textile substrates for the application of binder-free type all-solid-state flexible supercapacitor device.

First, N-doped carbon was prepared by amine functionalized MWCNT grafted polyimide precursor which was synthesized by *in situ* polymerization method following pyrolysis. The introduced amine-functionalized MWCNTs were improved electrochemical performances of carbonized PIs due to higher nitrogen contents and decreasing internal resistance in the carbon matrix.

Second, a novel and simple approach to the synthesis of multiple-heteroatom-doped carbon derived from polyimide precursors was prepared by an *in situ* method. The key point is that the monomer functional groups of polyimide precursors allow for easy doping with nitrogen, sulfur, and fluorine. Additional boron doping was obtained by homogeneous mixing with boric acid. Among these, N,F,B,-triple-doped carbon exhibits significantly enhanced electrochemical

performances. This result comes from the synergistic effects of several factors: (1) N,F co-doping enhanced the electrical conductivity; (2) boron doping improved the redox properties owing to the combination with oxygen atoms; (3) the increased wettability is due to the electronegativity of nitrogen and fluorine as well as boron complexed with oxygen.

Third, N,B-co-doped carbon using PI precursors was synthesized by adding the amount of  $\text{NH}_3\text{BH}_3$ . As a co-doping source,  $\text{NH}_3\text{BH}_3$  decomposed and released boron atoms as well as nitrogen atoms during the carbonization process. Owing to N,B-co-doping effects, N,B-co-doped carbon exhibited the improved electrochemical performances rather than that of N-doped carbon.

Fourth, binder-free type all-solid-state flexible supercapacitor device fabricated using carbon cloth for flexible current collector. This fabrication process presents significant advantages to control over the mass loading of active material on the CC surface and available large scale production of electrode. The fabricated devices demonstrated excellent mechanical durability and electrochemical stability.

Finally, although electrochemical performances of NFBCP, CC/C-MWNCT-PI-800, and NBCP were highly improved by the heteroatom

doping strategy into carbon matrix, the volumetric energy densities of devices are in the range of 0.38~0.58 mWh cm<sup>-3</sup>, which has not improved drastically (**Figure 4.1**). The main reason is due to the volumetric energy density has an inverse relationship with total volume of device. Therefore, while maintaining their mechanical durability and flexibility, reducing thickness of current collectors or fabricating thin current collectors by heteroatom doped carbon itself will be good suggestions.

These works not only provide a simple preparation route for heteroatom doped carbon materials for high-performance supercapacitor electrodes, but also reveal the potential of these materials for applications in carbon-textile-based flexible supercapacitor devices.

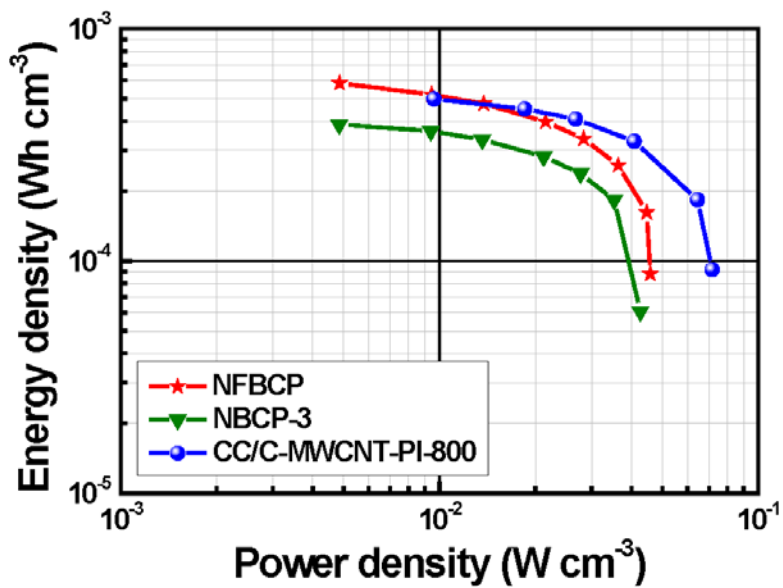


**Figure 4.1.** Ragone plots of the flexible all-solid-state supercapacitor devices of NFBCP, NBCP-3, and CC/C-MWCNT-PI-800.

## References

- [1] Jost, K.; Dion, G.; Gogotsi, Y., *J. Mater. Chem. A*, **2014**, 2, 10776-10787.
- [2] Simon, P.; Gogotsi, Y., *Nat. Mater.*, **2008**, 7, 845-854.
- [3] Frackowiak, E., *Phys. Chem. Chem. Phys.*, **2007**, 9, 1774-85.
- [4] Rolison, D. R.; Long, J. W.; Lytle, J. C.; Fischer, A. E.; Rhodes, C. P.; McEvoy, T. M.; Bourg, M. E.; Lubers, A. M., *Chem. Soc. Rev.*, **2009**, 38, 226-252.
- [5] Beguin, F.; Presser, V.; Balducci, A.; Frackowiak, E., *Adv. Mater.*, **2014**, 26, 2219-2251.
- [6] Wang, G.; Zhang, L.; Zhang, J., *Chem Soc Rev*, **2012**, 41, 797-828.
- [7] Zhang, L. L.; Zhao, X. S., *Chem. Soc. Rev.*, **2009**, 38, 2520-31.
- [8] Zhu, Y.; Murali, S.; Stoller, M. D.; Ganesh, K. J.; Cai, W.; Ferreira, P. J.; Pirkle, A.; Wallace, R. M.; Cychosz, K. A.; Thommes, M.; Su, D.; Stach, E. A.; Ruoff, R. S., *Science*, **2011**, 332, 1537-1541.
- [9] Hao, L.; Li, X.; Zhi, L., *Adv. Mater.*, **2013**, 25, 3899-3904.
- [10] Paraknowitsch, J. P.; Thomas, A., *Energy Environ. Sci.*, **2013**, 6,

2839-2855.

- [11] Han, L.-N.; Wei, X.; Zhu, Q.-C.; Xu, S.-M.; Wang, K.-X.; Chen, J.-S., *J. Mater. Chem. A*, **2016**, 4, 16698-16705.
- [12] Mendes, T. C.; Xiao, C.; Zhou, F.; Li, H.; Knowles, G. P.; Hilder, M.; Somers, A.; Howlett, P. C.; MacFarlane, D. R., *ACS Appl. Mater. Interfaces*, **2016**, 8, 35243-35252.
- [13] Jurewicz, K.; Babel, K.; Żiółkowski, A.; Wachowska, H., *Electrochim. Acta*, **2003**, 48, 1491-1498.
- [14] Lai, L.; Potts, J. R.; Zhan, D.; Wang, L.; Poh, C. K.; Tang, C.; Gong, H.; Shen, Z.; Lin, J.; Ruoff, R. S., *Energy Environ. Sci.*, **2012**, 5, 7936-7942.
- [15] Hulicova-Jurcakova, D.; Seredych, M.; Lu, G. Q.; Bandosz, T. J., *Adv. Funct. Mater.*, **2009**, 19, 438-447.
- [16] Hulicova-Jurcakova, D.; Kodama, M.; Shiraishi, S.; Hatori, H.; Zhu, Z. H.; Lu, G. Q., *Adv. Funct. Mater.*, **2009**, 19, 1800-1809.
- [17] Jeong, H. M.; Lee, J. W.; Shin, W. H.; Choi, Y. J.; Shin, H. J.; Kang, J. K.; Choi, J. W., *Nano Lett.*, **2011**, 11, 2472-7.
- [18] Wei, L.; Sevilla, M.; Fuertes, A. B.; Mokaya, R.; Yushin, G., *Adv. Funct. Mater.*, **2012**, 22, 827-834.
- [19] Su, F.; Poh, C. K.; Chen, J. S.; Xu, G.; Wang, D.; Li, Q.; Lin, J.;

- Lou, X. W., *Energy Environ. Sci.*, **2011**, 4, 717-724.
- [20] Li, L.; Liu, E.; Li, J.; Yang, Y.; Shen, H.; Huang, Z.; Xiang, X.; Li, W., *J. Power Sources*, **2010**, 195, 1516-1521.
- [21] Zhu, T.; Zhou, J.; Li, Z.; Li, S.; Si, W.; Zhuo, S., *J. Mater. Chem. A*, **2014**, 2, 12545-12551.
- [22] Zhou, J.; Zhu, T.; Xing, W.; Li, Z.; Shen, H.; Zhuo, S., *Electrochim. Acta*, **2015**, 160, 152-159.
- [23] Hulicova, D.; Kodama, M.; Hatori, H., *Chem. Mater.*, **2006**, 18, 2318-2326.
- [24] Ra, E. J.; Raymundo-Piñero, E.; Lee, Y. H.; Béguin, F., *Carbon*, **2009**, 47, 2984-2992.
- [25] Guo, D.-C.; Mi, J.; Hao, G.-P.; Dong, W.; Xiong, G.; Li, W.-C.; Lu, A.-H., *Energy Environ. Sci.*, **2013**, 6, 652-659.
- [26] Zhou, J.; Lian, J.; Hou, L.; Zhang, J.; Gou, H.; Xia, M.; Zhao, Y.; Strobel, T. A.; Tao, L.; Gao, F., *Nat. Commun.*, **2015**, 6, 8503.
- [27] Huang, S.; Li, Y.; Feng, Y.; An, H.; Long, P.; Qin, C.; Feng, W., *J. Mater. Chem. A*, **2015**, 3, 23095-23105.
- [28] Kiciński, W.; Szala, M.; Bystrzejewski, M., *Carbon*, **2014**, 68, 1-32.
- [29] Zhao, X.; Zhang, Q.; Chen, C.-M.; Zhang, B.; Reiche, S.; Wang,

- A.; Zhang, T.; Schlögl, R.; Sheng Su, D., *Nano Energy*, **2012**, 1, 624-630.
- [30] Zhou, Y.; Candelaria, S. L.; Liu, Q.; Huang, Y.; Uchaker, E.; CaO, G., *J. Mater. Chem. A*, **2014**, 2, 8472-8482.
- [31] Wang, D. W.; Li, F.; Chen, Z. G.; Lu, G. Q.; Cheng, H. M., *Chem. Mater.*, **2008**, 20, 7195-7200.
- [32] Agnoli, S.; Favaro, M., *J. Mater. Chem. A*, **2016**, 4, 5002-5025.
- [33] Na, W.; Jun, J.; Park, J. W.; Lee, G.; Jang, J., *J. Mater. Chem. A*, **2017**, 5, 17379-17387.
- [34] Wei, D.; Liu, Y.; Wang, Y.; Zhang, H.; Huang, L.; Yu, G., *Nano Lett.*, **2009**, 9, 1752-1758.
- [35] Zhou, H.; Peng, Y.; Wu, H. B.; Sun, F.; Yu, H.; Liu, F.; Xu, Q.; Lu, Y., *Nano Energy*, **2016**, 21, 80-89.
- [36] Poh, H. L.; Simek, P.; Sofer, Z.; Pumera, M., *ACS Nano*, **2013**, 7, 5262-5272.
- [37] Yu, X.; Park, H. S., *Carbon*, **2014**, 77, 59-65.
- [38] Chen, L. F.; Zhang, X. D.; Liang, H. W.; Kong, M.; Guan, Q. F.; Chen, P.; Wu, Z. Y.; Yu, S. H., *ACS Nano*, **2012**, 6, 7092-102.
- [39] Miao, F.; Shao, C.; Li, X.; Wang, K.; Liu, Y., *J. Mater. Chem. A*, **2016**, 4, 4180-4187.

- [40] Liaw, D.-J.; Wang, K.-L.; Huang, Y.-C.; Lee, K.-R.; Lai, J.-Y.; Ha, C.-S., *Prog. Polym. Sci.*, **2012**, 37, 907-974.
- [41] Inagaki, M.; Ohta, N.; Hishiyama, Y., *Carbon*, **2013**, 61, 1-21.
- [42] Sroog, C. E., *J. Polym. Sci., Part D*, **1976**, 11, 161-208.
- [43] Inagaki, M.; Harada, S.; Sato, T.; Nakajima, T.; Horino, Y.; Morita, K., *Carbon*, **1989**, 27, 253-257.
- [44] Le, T.; Yang, Y.; Huang, Z.; Kang, F., *J. Power Sources*, **2015**, 278, 683-692.
- [45] Kim, C.; Choi, Y.-O.; Lee, W.-J.; Yang, K.-S., *Electrochim. Acta.*, **2004**, 50, 883-887.
- [46] Li, Y.; Dong, J.; Zhang, J.; Zhao, X.; Yu, P.; Jin, L.; Zhang, Q., *Small*, **2015**, 11, 3476-84.
- [47] Jung, K.-H.; Ferraris, J. P., *Carbon*, **2012**, 50, 5309-5315.
- [48] Peng, Z.; Ye, R.; Mann, J. A.; Zakhidov, D.; Li, Y.; Smalley, P. R.; Lin, J.; Tour, J. M., *ACS Nano*, **2015**, 9, 5868-75.
- [49] Cai, J.; Lv, C.; Watanabe, A., *Nano Energy*, **2016**, 30, 790-800.
- [50] Xu, Z.; Zhuang, X.; Yang, C.; Cao, J.; Yao, Z.; Tang, Y.; Jiang, J.; Wu, D.; Feng, X., *Adv. Mater.*, **2016**, 28, 1981-7.
- [51] Chen, Y.; Gao, Z.; Zhang, B.; Zhao, S.; Qin, Y., *J. Power Sources*, **2016**, 315, 254-260.

- [52] Kaempgen, M.; Chan, C. K.; Ma, J.; Cui, Y.; Gruner, G., *Nano Lett.*, **2009**, 9, 1872-6.
- [53] Zheng, G.; Hu, L.; Wu, H.; Xie, X.; Cui, Y., *Energ. Environ. Sci.*, **2011**, 4, 3368-3373.
- [54] Chen, L.-F.; Huang, Z.-H.; Liang, H.-W.; Yao, W.-T.; Yu, Z.-Y.; Yu, S.-H., *Energ. Environ. Sci.*, **2013**, 6, 3331-3338.
- [55] El-Kady, M. F.; Strong, V.; Dubin, S.; Kaner, R. B., *Science*, **2012**, 335, 1326-30.
- [56] Xu, P.; Gu, T.; Cao, Z.; Wei, B.; Yu, J.; Li, F.; Byun, J.-H.; Lu, W.; Li, Q.; Chou, T.-W., *Adv. Energy Mater.*, **2014**, 4, 1300759.
- [57] Meng, Y.; Zhao, Y.; Hu, C.; Cheng, H.; Hu, Y.; Zhang, Z.; Shi, G.; Qu, L., *Adv. Mater.*, **2013**, 25, 2326-31.
- [58] Wang, G.; Wang, H.; Lu, X.; Ling, Y.; Yu, M.; Zhai, T.; Tong, Y.; Li, Y., *Adv. Mater.*, **2014**, 26, 2676-2682.
- [59] Yang, M.; Cheng, B.; Song, H.; Chen, X., *Electrochim. Acta*, **2010**, 55, 7021-7027.
- [60] Horng, Y.-Y.; Lu, Y.-C.; Hsu, Y.-K.; Chen, C.-C.; Chen, L.-C.; Chen, K.-H., *J. Power Sources*, **2010**, 195, 4418-4422.
- [61] Chen, Y.-C.; Hsu, Y.-K.; Lin, Y.-G.; Lin, Y.-K.; Horng, Y.-Y.; Chen, L.-C.; Chen, K.-H., *Electrochim. Acta*, **2011**, 56, 7124-

7130.

- [62] Qian, Y.; Liu, R.; Wang, Q.; Xu, J.; Chen, D.; Shen, G., *J. Mater. Chem. A*, **2014**, 2, 10917-10922.
- [63] Yu, Z.-Y.; Chen, L.-F.; Yu, S.-H., *J. Mater. Chem. A*, **2014**, 2, 10889-10894.
- [64] Xia, C.; Chen, W.; Wang, X.; Hedhili, M. N.; Wei, N.; Alshareef, H. N., *Adv. Energy Mater.*, **2015**, 5, 1401805.
- [65] Lam, D. V.; Jo, K.; Kim, C. H.; Kim, J. H.; Lee, H. J.; Lee, S. M., *ACS Nano*, **2016**, 10, 11351-11359.
- [66] Lim, J.; Shin, D. G.; Yeo, H.; Goh, M.; Ku, B.-C.; Yang, C.-M.; Lee, D. S.; Hwang, J.-Y.; Park, B.; You, N.-H., *J. Polym. Sci. Pol. Phys.*, **2014**, 52, 960-966.
- [67] Xiong, G.; Meng, C.; Reifengerger, R. G.; Irazoqui, P. P.; Fisher, T. S., *Adv. Energy Mater.*, **2014**, 4, 1300515.
- [68] Zhao, Y.; Liu, M.; Deng, X.; Miao, L.; Tripathi, P. K.; Ma, X.; Zhu, D.; Xu, Z.; Hao, Z.; Gan, L., *Electrochim. Acta*, **2015**, 153, 448-455.
- [69] Wan, L.; Wang, J.; Xie, L.; Sun, Y.; Li, K., *ACS. Appl. Mater. Interfaces*, **2014**, 6, 15583-96.
- [70] Yuan, W.; Che, J.; Chan-Park, M. B., *Chem. Mater.*, **2011**, 23,

4149-4157.

- [71] Hulicova-Jurcakova, D.; Kodama, M.; Shiraishi, S.; Hatori, H.; Zhu, Z. H.; Lu, G. Q., *Adv. Funct. Mater.*, **2009**, 19, 1800-1809.
- [72] Candelaria, S. L.; Garcia, B. B.; Liu, D.; Cao, G., *J. Mater. Chem.*, **2012**, 22, 9884-9889.
- [73] Stoller, M. D.; Park, S.; Zhu, Y.; An, J.; Ruoff, R. S., *Nano Lett.*, **2008**, 8, 3498-3502.
- [74] Li, L.; Zhong, Q.; Kim, N. D.; Ruan, G.; Yang, Y.; Gao, C.; Fei, H.; Li, Y.; Ji, Y.; Tour, J. M., *Carbon*, **2016**, 105, 260-267.
- [75] Shi, K.; Ren, M.; Zhitomirsky, I., *ACS Sustain. Chem. Eng.*, **2014**, 2, 1289-1298.
- [76] Sevilla, M.; Yu, L.; Zhao, L.; Ania, C. O.; Titiricic, M.-M., *ACS Sustain. Chem. Eng.*, **2014**, 2, 1049-1055.
- [77] Chen, W.; Chen, W.; Zhang, B.; Yang, S.; Liu, C.-Y., *Polymer*, **2017**, 109, 205-215.
- [78] Ferrari, A. C.; Basko, D. M., *Nat. Nanotechnol.*, **2013**, 8, 235-246.
- [79] Cançado, L. G.; Takai, K.; Enoki, T.; Endo, M.; Kim, Y. A.; Mizusaki, H.; Jorio, A.; Coelho, L. N.; Magalhães-Paniago, R.; Pimenta, M. A., *Appl. Phys. Lett.*, **2006**, 88, 163106.

- [80] Ferrari, A. C., *Solid State Commun.*, **2007**, 143, 47-57.
- [81] Hyun, K.; Saito, N., *Sci. Rep.*, **2017**, 7, 3825.
- [82] Li, Y.; Wang, G.; Wei, T.; Fan, Z.; Yan, P., *Nano Energy*, **2016**, 19, 165-175.
- [83] Chang, Y.; Yuan, C.; Liu, C.; Mao, J.; Li, Y.; Wu, H.; Wu, Y.; Xu, Y.; Zeng, B.; Dai, L., *J. Power Sources*, **2017**, 365, 354-361.
- [84] Qian, W.; Sun, F.; Xu, Y.; Qiu, L.; Liu, C.; Wang, S.; Yan, F., *Energy Environ. Sci.*, **2014**, 7, 379-386.
- [85] Yun, Y. S.; Cho, S. Y.; Shim, J.; Kim, B. H.; Chang, S. J.; Baek, S. J.; Huh, Y. S.; Tak, Y.; Park, Y. W.; Park, S.; Jin, H. J., *Adv. Mater.*, **2013**, 25, 1993-1998.
- [86] Kim, D. K.; Kim, N. D.; Park, S.-K.; Seong, K.-d.; Hwang, M.; You, N.-H.; Piao, Y., *J. Power Sources*, **2018**, 380, 55-63.
- [87] Wu, Z. S.; Winter, A.; Chen, L.; Sun, Y.; Turchanin, A.; Feng, X.; Mullen, K., *Adv. Mater.*, **2012**, 24, 5130-5135.
- [88] Chen, H.; Xiong, Y.; Yu, T.; Zhu, P.; Yan, X.; Wang, Z.; Guan, S., *Carbon*, **2017**, 113, 266-273.
- [89] Stoller, M. D.; Park, S.; Zhu, Y.; An, J.; Ruoff, R. S., *Nano Lett.*, **2008**, 8, 3498-3502.
- [90] Guo, H.; Gao, Q., *J. Power Sources*, **2009**, 186, 551-556.

- [91] Zhang, J.; Nie, N.; Liu, Y.; Wang, J.; Yu, F.; Gu, J.; Li, W., *ACS Appl. Mater. Interfaces*, **2015**, 7, 20134-20143.
- [92] Lin, Y.; Zhu, Y.; Zhang, B.; Kim, Y. A.; Endo, M.; Su, D. S., *J. Mater. Chem. A*, **2015**, 3, 21805-21814.
- [93] Basko, D. M.; Piskanec, S.; Ferrari, A. C., *Phys. Rev. B*, **2009**, 80.
- [94] Casiraghi, C., *Phys. Rev. B*, **2009**, 80.
- [95] Han, J.; Zhang, L. L.; Lee, S.; Oh, J.; Lee, K. S.; Potts, J. R.; Ji, J. Y.; Zhao, X.; Ruoff, R. S.; Park, S., *Acs Nano*, **2013**, 7, 19-26.

## 국 문 초 록

화석 연료의 한계와 기후 변화 등의 문제점 등으로 인하여 전 세계적으로 신재생 에너지 생산 및 고성능 에너지 저장 장치에 대한 관심이 높아지고 있다. 슈퍼커패시터는 전기화학 방식을 이용한 에너지 저장 장치 중 하나로 고출력 특성과 반영구적인 수명등의 장점을 갖고 있다. 슈퍼커패시터 중 하나인 전기이중층커패시터는 이온과 활물질의 물리적 흡탈착 방식으로 에너지를 저장하고 있으며 주로 탄소 재료를 전극 물질로 사용하고 있다. 높은 출력 특성, 전기 전도성, 수명 안정성 등의 장점을 갖고 있으나 특히 낮은 에너지 밀도가 한계로 지적 받고 있으며 이를 해결하기 위하여 많은 연구들이 진행 되고 있다. 본 연구에서는 폴리이미드를 탄소 전구체로 사용하였으며 여기에 다양한 종류의 이중원소 도핑을 통한 방법으로 에너지 밀도를 높이하고자 하였다.

첫째, 탄소나노튜브 폴리이미드 복합 전구체를 이용하여 질소 도핑 된 탄소 전극 재료를 합성하였다. 본 연구에서 사용된 표면 화학 개질된 탄소나노튜브는 아민을 갖고 있어 질소 함량을 증가 시킬 수 있으며 탄소나노튜브의

전기전도성은 전극에서의 저항 감소를 통하여 전기화학 특성을 향상 시킬 수 있다. 또한 탄소나노튜브 폴리이미드 전구체를 일정량 유연성을 갖는 탄소천 위에 바른 후 열처리 공정을 진행하였다. 그 결과 열처리 후 폴리이미드 전구체는 탄소천 위에 고르게 탄화되어 분포 되어있음을 보였고 부가적인 첨가제 없이 전극이 제작 가능함을 보였으며 탄소천은 유연성을 유지 하였다. 삼전극에서의 전기화학 특성 평가 결과  $1 \text{ A g}^{-1}$ 에서  $333.4 \text{ F g}^{-1}$ 의 용량을 보였으며 일만 회의 수명 평가에서도 초기 대비 103%의 용량을 유지함을 보였다. 유연 소자 제작 결과  $0.02 \text{ mA cm}^{-3}$ 에서  $3.88 \text{ F cm}^{-3}$ 의 용량을 나타내었고  $0.50 \text{ mWh cm}^{-3}$ 의 에너지 밀도값을 보였다. 또한 여러 형태의 물리적 변형에서도 안정적인 전기화학 특성을 보였다.

둘째, 질소 단일 원소 이외의 두가지 또는 세가지 이중원소의 조합을 통한 도핑을 시도 하였다. 폴리이미드 전구체는 다양한 단량체의 조합을 통하여 원하는 작용기를 부여 할 수 있으며 간단히 외부에서 이중 도핑 원소 재료를 첨가 할 수 있는 장점이 있다. 질소 단일 원소 이외에 질소와 황, 질소와 불소 등의 이중원소 된 탄소 재료를 합성하였고 또한 질소, 황, 붕산 그리고 질소, 불소, 붕산 등 삼중 원소가

도핑 된 탄소 재료를 합성하였다. 그 결과 단일 혹은 이중 원소 도핑 보다는 삼중 원소 도핑이 전기 화학 특성을 향상 시킴을 확인 할 수 있었다. 이 중에서 질소, 불소, 붕산의 삼중 원소 조합을 가질때 삼전극 환경에서 가장 높은 전기화학 특성을 나타내었으며  $1 \text{ A g}^{-1}$  에서  $350.3 \text{ F g}^{-1}$ 의 용량값을 보였다. 이를 유연 소자로 제작하였을 경우  $0.01 \text{ mA cm}^{-3}$ 에서  $4.45 \text{ F cm}^{-3}$  의 용량값을 나타내었으며  $0.58 \text{ mWh cm}^{-3}$ 의 에너지 밀도 값을 보였다.

마지막으로, 질소와 붕소가 동시에 도핑 된 폴리이미드 전구체 기반 탄소 재료를 합성하였다. 사용된 붕소 도핑 재료로  $\text{NH}_3\text{BH}_3$ 를 사용하였는데 열처리 과정 중 붕소 원소뿐만 아니라 동시에 질소 원소를 방출하여 두 가지 원소가 동시에 도핑 되는 효과를 얻을 수 있는 장점이 있다. 폴리이미드 전구체에 첨가 된  $\text{NH}_3\text{BH}_3$  함량에 따른 탄소 재료의 물질 특성 및 전기 화학 성능 평가를 진행 하였다. 그 결과 삼전극 환경에서  $1 \text{ A g}^{-1}$  에서  $350.3 \text{ F g}^{-1}$ 의 용량값을 보였다. 또한 유연 소자로 제작하여  $0.01 \text{ mA cm}^{-3}$ 에서  $2.97 \text{ F cm}^{-3}$  의 용량값을 나타내었으며  $0.38 \text{ mWh cm}^{-3}$ 의 에너지 밀도 값을 보였다.

결과적으로 본 연구에서는 슈퍼커패시터 탄소 전극 재료로

폴리이미드 전구체를 사용하였으며 간단한 방법으로 다양한 이종 원소의 도핑을 유도 할 수 있었다. 또한 첨가제 없이 열처리 공정만으로 탄소천 기반의 유연 전극 소자 제작이 가능함을 보였다. 이와 같이 다양한 방법으로 합성된 탄소 재료의 전기화학적 특성평가를 통해 슈퍼커패시터 전극 재료로서의 가능성을 보여주었으며, 또한 높은 유연성 및 전기화학 안정성을 갖고 있어서 다양한 응용분야에 적용될 수 있다는 것을 보여주었다.

주요어: 슈퍼커패시터, 탄소 재료, 폴리이미드, 이종원소 도핑, 유연 전극

학 번: 2012-30692